DVCS at HERMES: The Recoil Detector & Transverse Target Spin Asymmetries

Morgan J. Murray

A Thesis presented for the degree of
Doctor of Philosophy

Nuclear Physics Experimental Research Group
Department of Physics and Astronomy
University of Glasgow
Scotland
July 2007

DVCS at HERMES: The Recoil Detector and Transverse Target Spin Asymmetries

Morgan J. Murray

Submitted for the degree of Doctor of Philosophy
July 2007

Abstract

The HERMES experiment is a large forward angle spectrometer located at the HERA accelerator ring at DESY, Hamburg. One of the most exciting topics studied at HERMES is Deeply Virtual Compton Scattering (DVCS) which is the simplest interaction that provides a gateway for access to Generalised Parton Distributions (GPDs). GPDs are a theoretical framework which can be used to calculate the total angular momentum of the quarks in the nucleon. As such, they provide one piece of the puzzle of nucleonic spin structure.

In 2005, HERMES was upgraded in the target region with a Recoil Detector that allows it to make truly exclusive measurements of the DVCS interaction for the first time. The design and construction of the Recoil Detector is discussed herein, in addition to a complete analysis of the Transverse Target Spin Asymmetry (TTSA) in DVCS. Experimental facilities that enable measurement of this asymmetry are rare. The importance of the information on the TTSA from HERMES is made yet greater as the transversely polarised target that allows the asymmetry to be measured has been replaced by an unpolarised target. This was to allow the Recoil Detector to be installed. The final stage of this thesis shows a model-dependent method for constraining the angular momentum of the quarks in the nucleon and speculates as to the other pieces of the spin puzzle.

Declaration

The work in this thesis is based on research carried out at the Nuclear Physics Experimental Research group, Department of Physics and Astronomy, University of Glasgow, Scotland. No part of this thesis has been submitted elsewhere for any other degree or qualification and it is all my own work unless referenced to the contrary in the text.

Acknowledgements

Whilst the thesis declaration states that the following is all my own work, it would not exist if I didn't have help from various people over the last four years. I want to thank Profs. G. Rosner and R. Kaiser for giving me the chance to learn by accepting me into Glasgow University's nuclear physics group. They gave me the opportunity to travel to DESY and experience another culture which is something that I specifically sought for my studies.

The people I worked with in DESY also deserve my thanks. J. Stewart, V. Prahl and I. Gregor all provided valuable advice and saved me from getting lost in my work on the recoil project. I. Hristova did a lot of work with me at the T22 facility in DESY, and provided me with a first introduction to programming, for which I am very grateful. W. D. Nowak provided very useful guidance at stages during my analysis work and I am grateful for his helping me to refine the interpretations presented here. Several of my other collaborators, too numerous to mention here, helped at various stages and for that I thank them.

Z. Ye was the first person to tackle the analysis issues presented in this thesis, and he was in constant e-mail contact throughout the work presented here. I thank him for the help he gave to me. Matthias Hoek and Björn Seitz arrived in Glagsow part-way through my PhD and provided support in numerous ways, from proof-reading my thesis to merely being available for five minutes to talk something through. I am very grateful for that.

Whilst in Glasgow, the people I saw every day from Rooms 407 and 410 helped to make life a little more bearable. Evie Downie, Eilidh McNicholl, Gordon Hill, Scott Lumsden and Tony Clarkson all contributed to lifting my spirits when times were hard. Gordon provided a valuable sounding board and I can only hope that he enjoys writing his thesis as much as I have enjoyed writing mine. I worked for some considerable time with Scott and I don't doubt that without him I would have spent more time miserable and confused. Tony also deserves my thanks for his

contributions towards figure 6.5 at the end of this thesis.

Markus Ehrenfried, Nils Pickert and Christian Vogel all provided me with priceless help throughout my work. Whenever I had some complicated problem they invariably helped find a simple solution. I hope that someday I can return all the favours that they have done me.

Finally, I'd like to thank my family, especially my father Anthony. Without the support of my parents I would never have been in a position to start my PhD, let alone complete my thesis. I am truly grateful for the opportunities that they have afforded me.

Contents

Abstract ii

Declaration iii

Acknowledgements iv

1 Introduction 1

2 GPDs and DVCS 3

2.1 Generalised Parton Distributions 4

2.1.1 Common Variables of Generalised Parton Distributions 5

2.1.2 GPDs and Currently Known Distributions 7

2.1.3 GPDs and the Spin Structure of the Nucleon 8

2.2 Accessing GPDs via DVCS at HERMES 9

2.3 Observable Asymmetries from DVCS at HERMES 12

2.3.1 Beam-Dependent Observables 12

2.3.2 Target Spin-Dependent Asymmetries 13

3 The HERMES Experiment 19

3.1 The HERA Storage Ring 19

3.1.1 The Polarised Lepton Beam 20

3.2 The Polarised Target 24

3.3 The HERMES Spectrometer 31

3.4 PID at HERMES 32
3.5 Tracking at HERMES 35
3.5.1 HERMES Reconstruction Code 36

4 The Recoil Detector 38
4.1 The Components of the Detector 38
4.2 The Storage Cell 42
4.3 The Silicon Detector 45
4.3.1 The Silicon Sensors 45
4.3.2 The Readout Electronics 46
4.4 Calibration and Testing of the Recoil Detector 48
4.4.1 The GSI Tests 49
4.4.2 The Cosmics Test 56
4.5 Integration with the HERMES Spectrometer 57

5 Transverse Target Spin Asymmetries in DVCS 59
5.1 Extraction of the Event Sample 59
5.1.1 Kinematic Definitions 61
5.1.2 Data Quality Cuts 65
5.1.3 Geometrical Cuts 67
5.2 Extraction of the TTSA Amplitude 69
5.2.1 Least Squares Fitting 69
5.2.2 The Maximum Likelihood Fitting Technique 71
5.3 TTSA Amplitudes 74
5.4 Systematic Errors 74
5.4.1 Total Systematic Errors 84

6 Interpretation 89

6.1 A Parameterisation of the Generalised Parton Distribution H 89
6.2 A Parametrisation of the GPD E 91
6.3 Calculating Observables in DVCS 93
6.3.1 Comparison with Data 93
6.3.2 The Constraint Result 96
6.4 Comparison with JLab Data 97
6.5 Total Angular Momentum Constraint 97
6.5.1 Interpretation of the Spin Equation 99
6.5.2 Simple Physical Interpretation 101
6.6 Future Work 102

7 Conclusions and Outlook **104**

A Inputs to the VGG Code **106**

B Quotations **108**

List of Figures

1.1 The spin puzzle relating to quarks in the nucleon 2

2.1 The u and d quark distributions in impact parameter space 4

2.2 The standard DIS graph 5

2.3 Illustration of DVCS and Beth-Heitler 10

2.4 BSA results from HERMES 14

2.5 BCA results from HERMES 15

2.6 LTSA results at HERMES 16

2.7 TTSA results at HERMES 18

3.1 The HERA Ring 20

3.2 HERA polarisation over selected months 25

3.3 Target System Schematic 26

3.4 Transverse Target Magnet 28

3.5 Breit-Rabi Polarimeter Schematic 29

3.6 Target Gas Analyser Schematic 30

3.7 HERMES Spectrometer Schematic 32

3.8 PID with H2 33

3.9 Pre-Shower and Calorimeter 34

3.10 Hermes Reconstruction Code schematic 36

4.1 HERMES + Recoil Schematic 39

4.2 3D CAD Representation of the Recoil Detector 40
4.3 Silicon Detector Photographs 41
4.4 Scintillating Fibre Detector Photographs 42
4.5 The energy deposition in the silicon and scintillating fibre detectors. . 43
4.6 Photon Detector and Magnet Photographs 44
4.7 Target Cell Photograph 44
4.8 Microscope picture of the silicon detectors onboard electronics 46
4.9 Silicon Detector process schematic 47
4.10 Schematic of the electronics on an HADC 48
4.11 Plots of the GSI data for the silicon detector 49
4.12 Plots of the GSI data from the SFT 50
4.13 Schematic of the DESY II Facility 51
4.14 Schematic of the silicon setup at T22 52
4.15 Alignment information from T22 54
4.16 Pedestal correction plots from T22 54
4.17 1 MIP response of the silicon detector 55
4.18 Sensor wide response of the silicon detector to 1 MIP signal 55
4.19 Efficiencies of a typical silicon module 56
4.20 Example track from the cosmics test of the recoil detector 57
4.21 Typical track through the recoil from production data 58

5.1 Schematic of the HERMES data structure 60
5.2 Angle Definitions for TTSA Calculation 61
5.3 Missing Mass Distribution at HERMES Kinematics 65
5.4 Probability functions from ML fit in Parameter Space 75
5.5 TTSA amplitudes from 2002-04 data set 76
5.6 TTSA amplitudes from 2005 data set 77

5.7 Difference between 02-04 and 05 data sets 78

6.1 Fit accuracy to data at various values of J_u. 94

6.2 χ^2-surface of "VGG model"/data comparison 95

6.3 Constraint for impact parameters (1,9) 96

6.4 Constraint Summary on J_u/J_d 98

6.5 Physical Interpretation of thesis conclusions 101

6.6 Projected DVCS errors with the Recoil Detector 103

7.1 DVCS Coverage over the next 15 years 105

List of Tables

2.1 Different GPDs at leading twist. 7

5.1 Spectrometer and Beam misalignment slopes and offsets 80

5.2 Systematic errors in A_{sc} for 2005 data. 85

5.3 Systematic errors in A_{cs}. 86

5.4 Table of Final Results for 2005 data. 87

Chapter 1

Introduction

It has long been known that hadrons can be thought of as being constituted from two or more quarks [Bjo69], [Fey89], [GM64], [Zwe94], with gluons binding the quarks into the hadronic state. However, this simplistic view of hadrons is of no use when we try to look deeper inside the particle, and attempt to acquire information about how the properties of the hadron are conveyed from those of its constituents.

The constituent spin contributions to the proton spin can be written [Ji97b]

$$\begin{aligned} \frac{1}{2} &= J_Q + J_G \\ &= \frac{1}{2}\Delta\Sigma + L_Q + \Delta G + L_G \end{aligned}$$

where $J_{Q,G}$ are the total angular momenta of quarks, gluons in the proton. $\Delta\Sigma$ represents the fraction of the spin carried by the constituent quarks, ΔG is the fraction of the spin carried by the gluons and L_Q and L_G are the orbital angular momenta of the quarks and gluons inside the hadron (see figure 1.1).

In 1988, the European Muon Collaboration at CERN [A$^+$88], [A$^+$89] published a result that showed that the contribution of the quark spin towards the total spin of the nucleon is so small as to be potentially consistent with zero — a result known as the "spin crisis" [LA88] due to its potentially devastating ramifications for QCD. Although later publications showed that the actual contribution is likely to be $\approx 30\%$ [Ter94], [A$^+$00b], [Ade98], [A$^+$07b], this still leaves a significant question to be answered: how is the rest of the spin of the nucleon composed? The principal scientific purpose of the HERMES experiment is to answer that question and in the last decade the HERMES collaboration has been at the forefront of many contributions to the field, in addition to producing other notable physics results.

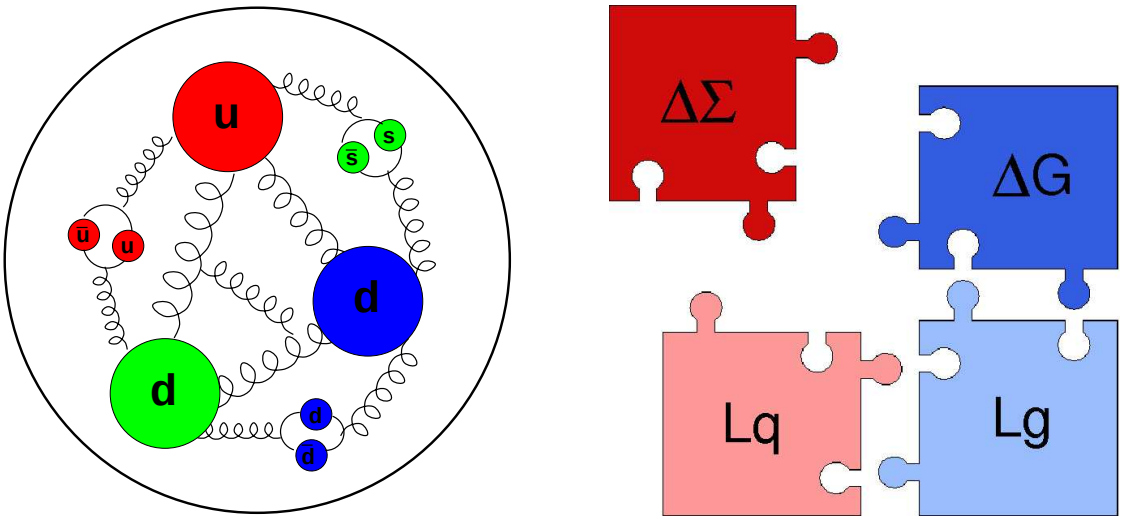

Figure 1.1: It has long been known that nucleons (left) are made of quarks and gluons but it has proven difficult to access information about how the characteristics of these partons contribute to the characterstics of the nucleon as a whole. Generalised Parton Distributions provide a framework to describe each parton's contribution to the nucleon's behaviour, symbolised by the spin puzzle (right) which shows the leading order contributions towards the overall nucleon spin.

References [A$^+$05a], [A$^+$05b], [A$^+$04], [A$^+$03], [A$^+$01b], [A$^+$00a] are just some of the papers published by HERMES on a wide variety of topics. Recently HERMES was upgraded in the target region with a recoil detector [ea97]. This detector was planned in order to allow exclusive measurements of Deeply Virtual Compton Scattering (DVCS)—a process described by $eP \rightarrow e'P'\gamma$ where e (e') and P (P') are initial (final) leptons and protons respectively and γ is a produced real photon.

The subject of DVCS has recently become of great interest in the spin physics community, as it is the simplest interaction which can be used to access information on Generalised Parton Distributions (GPDs) [DMR$^+$88], [MRG$^+$94], [Ji97b], [Ji97a], [Rad97]. These distributions can be used to entirely describe the total angular momentum of the quarks in the nucleon [Ji97b] and could provide information on the spatial distribution of quarks within the nucleon. As such they represent the possible completion of the spin puzzle and better knowledge of GPDs could present the possibility to fully understand the structure of the nucleon.

This thesis details work done on the recoil detector and presents an analysis of data from 2002-2005 from the HERMES experiment on the Transverse Target Spin Asymmetry in DVCS. This analysis includes detail on the systematic errors of the measurement, and how the asymmetry amplitude can be used to constrain the total angular momentum of the up and down quarks in the proton.

Chapter 2

Generalised Parton Distributions and Deeply Virtual Compton Scattering

Since the introduction of the "spin crisis" in the late 1980s [A+88], [A+89], [LA88], the size of contributions from elements within the nucleon to its overall spin has been an unsolved puzzle of hadronic physics. More recently research into the spin structure of the nucleon has been set against the wider background of research into Generalised Parton Distributions (GPDs) [MRG+94]. GPDs incorporate regular parton distribution functions and form factors into a framework for a phenomenological description of the nucleon and provide the possibility to interpret observables from medium-energy experiments in a physically intuitive way, describing the transverse distributions of quarks in the nucleon for example (see figure 2.1).

Research into GPDs originally evolved from two separate approaches aimed at contextualising ordinary well-known and experimentally verified Parton Distribution Functions (PDFs). These mathematical descriptions are valid only in the forward limit and investigations by Ji [Ji97b], [Ji97a] and Radyushkin [Rad97] led respectively to Off-Forward Parton Distributions (OFPDs) and Non-Forward Parton Distributions (NFPDs). Both similar ideas, the former described the longitudinal momentum fraction of the quark in the nucleon in terms of $x + \xi$ and $x - \xi$ where ξ is referred to as the "skewedness" of the interaction. NFPDs chose to write the momentum fraction of the quark in the nucleon as X and describe the it as having lost momentum fraction ζ. Since the Trento convention of 2002 [BDDM04], HERMES has chosen to work with the OFPD description [Ell04] and it is the OFPD notation

that has survived as that of Generalised Parton Distributions.

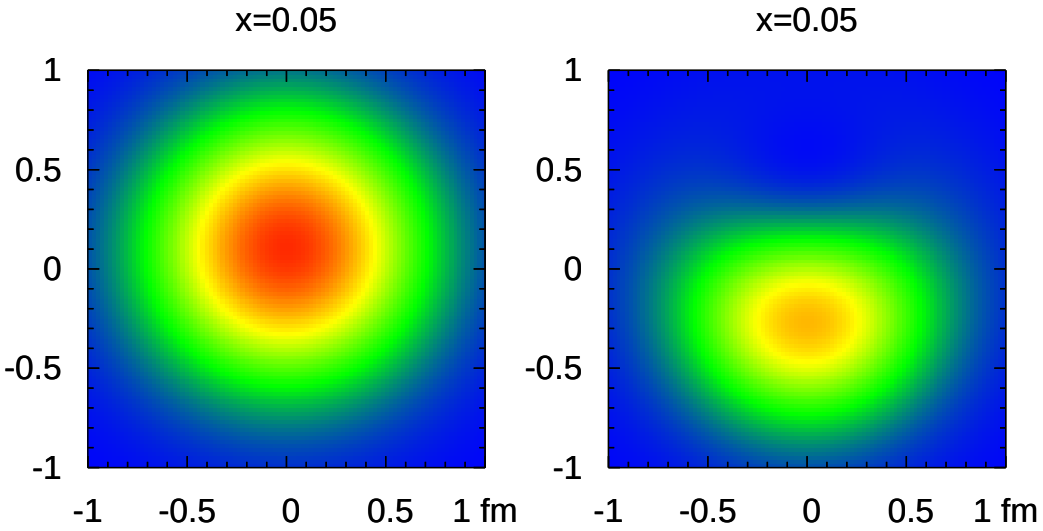

Figure 2.1: The u (left) and d (right) quark densities in the impact parameter plane at x = 0.05 for a transversely polarised proton. The warmer colours show increasing probability. These figures are taken from [Kro06].

This chapter shows GPDs in a physics context, with particular attention paid towards GPDs and the Deeply Virtual Compton Scattering (DVCS) process at HERMES. Section 2.1 explains the links between GPDs and well-known functions, such as form factors and parton distribution functions. This section also notes the relationship between GPDs and the spin structure of the nucleon. Section 2.2 explains the difficulty in accessing GPDs at HERMES, showing that, in order to access the GPD framework, it is necessary to consider convolutions of GPDs with had scattering kernels. Section 2.3 then shows the different observables available to analysers at the HERMES experiment, showing some of the links between observables and GPDs.

2.1 Generalised Parton Distributions

This section describes some of the nomenclature used in discussions about GPDs and shows their relation to well-known quantities such as form factors. Generalised Parton Distributions are complicated quantities and not all are directly accessible through measurements made at HERMES. Table 2.1.1 shows the four GPDs that are accessible at leading-order by measurements made at HERMES. It further describes the relation known as "Ji's sum rule" and explains its significance in understanding the spin structure of the nucleon.

2.1.1 Common Variables of Generalised Parton Distributions

When describing GPDs, it is common to refer to them as having dependence upon three variables: x_B, ξ and t. (Whilst there is an additional dependence on the measurement scale μ^2 this is rarely stated implicitly and will from here be taken as implied.) Before defining these three variables, some basic kinematic definitions are required.

The regular DIS graph can be seen in figure 2.2. It shows an incoming lepton (an electron/positron in the case of HERMES) with four momentum **k** scattering off a proton with four momentum **P**. The lepton leaves with four momentum **k'** and the proton leaves in an undefined final state. In the case of elastic scattering (as in the rest of this thesis), the proton remains intact.

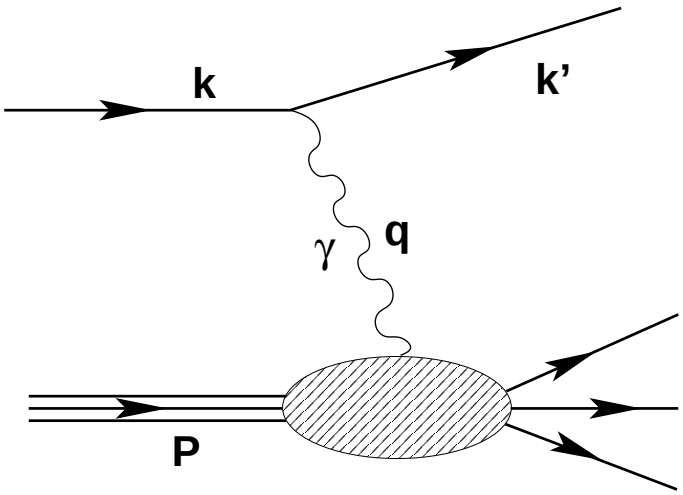

Figure 2.2: The standard graph representing Deep Inelastic Scattering. An initial lepton with four momentum **k** scatters from proton **P** and leaves with a changed four momentum **k'**. The four momentum of the virtual photon is written as **q**. The final state of the proton is undefined in regular DIS, but in the elastic case examined in this thesis, the proton remains intact.

The quantities used regularly to describe the process are

$$s \equiv (\mathbf{k}+\mathbf{P})^2 \tag{2.1}$$

$$q^2 \equiv -Q^2 = (\mathbf{k}-\mathbf{k'})^2 < 0 \tag{2.2}$$

$$W^2 \equiv (\mathbf{P}+\mathbf{q})^2 \tag{2.3}$$

$$\nu \equiv \frac{\mathbf{P}\cdot\mathbf{q}}{M} \tag{2.4}$$

where s denotes the total available centre of mass energy squared, q^2 denotes the four momentum transfer of the virtual photon involved in the process, W^2 is the square of the invariant mass of the final hadronic state(s). These three quantities are Lorentz-invariant, however there is no such interpretation of ν. Transferring these quantities into the proton rest frame for a fixed-target experiment experiment like HERMES, the following are obtained, where $\cong$ is used as shorthand for "in the lab frame":

$$\begin{aligned} s &\cong 2ME + M^2 && (2.5)\\ Q^2 &\cong 4EE' \sin^2 \frac{\theta}{2} && (2.6)\\ W^2 &\cong M^2 + 2M\nu - Q^2 && (2.7)\\ \nu &\cong E - E', && (2.8) \end{aligned}$$

where E (E') is the initial (final) energy of the scattered lepton, θ is the scattering angle of the lepton with respect to the direction of the initial lepton and M is the rest mass of the proton. In this case ν is simply the energy loss of the scattered lepton. In addition, there are two more variables defined

$$\begin{aligned} x_B &= \frac{Q^2}{2\mathbf{P}\cdot\mathbf{q}} && (2.9)\\ y &= \frac{\mathbf{P}\cdot\mathbf{q}}{\mathbf{P}\cdot\mathbf{k}}. && (2.10) \end{aligned}$$

which, in the proton rest frame become

$$\begin{aligned} x_B &\cong \frac{Q^2}{M\nu} && (2.11)\\ y &\cong \frac{\nu}{E} && (2.12) \end{aligned}$$

In regular DIS x_B is the fraction of longitudinal momentum of the nucleon carried by the quark struck in the process. It is the same x_B which is mentioned above as a variable used to describe GPDs. y can be interpreted as the fraction of the beam energy carried by the virtual photon in the proton's rest frame. Having defined these variables, they will be used throughout this chapter. A further discussion of the important variables for a practical DVCS analysis can be found in chapter 5.

Having now defined x_B, the other two variables that are important for GPDs are:

1. ξ — the "skewedness" parameter, related in the HERMES kinematic region to the well-known x-Bjorken x_B as $\xi \approx \frac{x_B}{2-x_B}$. It is this variable that describes the "off-forwardness" of the process, its deviation from regular PDFs.

2. t — a Mandlestam variable, the transverse momentum transfer during the interaction. Given by $t = (\mathbf{P} - \mathbf{P'})^2$ where P and P' are the four-momenta of the initial– and final–state protons respectively.

Another common quantity referred to during discussions of GPDs is that of *twist*, a quantum number derived from operator product expansions that arise whilst manipulating the hadronic tensor. Further definitions of this quantity can be found e.g. in [Jaf96] and [Car99]. It is sufficient for this discussion, however, merely to note that the twist of a term refers usually to its suppression of $\mathcal{O}(\frac{1}{Q})$ and that the smallest possible twist number is two—that is that an object described as twist-2 has no suppression by $(\frac{1}{Q})$ whereas a twist-3 object has suppression by $(\frac{1}{Q})$ and a twist-4 object is suppressed by $(\frac{1}{Q^2})$ etc. Unless otherwise stated, everything in this thesis is taken at leading twist, i.e. twist-2.

In the HERMES measurement range, and for the details discussed in this work, there are four twist-2 GPDs, described in table 2.1.1.

	Nucleon Helicity Conserving	Nucleon Helicity Flipping
Unpolarised GPDs	H	E
Polarised GPDs	$\tilde{H}$	$\tilde{E}$

Table 2.1: Different GPDs at leading twist.

Each of the GPDs described in table 2.1.1 exists for each quark flavour q and there exists an implied equivalent for gluons. Gluon GPDs are not the subject of this work and will no longer be mentioned here.

2.1.2 GPDs and Currently Known Distributions

Parton Distribution Functions

At the forward limit where $t \to 0$ and $\xi \to 0$, GPDs reduce to regular PDFs. Specifically,

$$H^q(x,0,0) = q(x) \quad \text{and} \quad \tilde{H}^q(x,0,0) = \Delta q \tag{2.13}$$

where $q(x)$ is the longitudinal distribution of quarks of flavour q in the nucleon and Δq is the helicity distribution inside the nucleon. It was from the measurements of $\Delta\Sigma = \sum_q \Delta q + \Delta\,\bar{q}$ that the "spin crisis" or puzzle originated, as initial measurements found that it could be consistent with zero and later measurements showed that it could not account for the total spin of the nucleon.

Form Factors

The first x-moment of the GPDs in table 2.1.1 reduce to form factors as [Ji97b]:

$$\begin{aligned} \int_{-1}^{1} dx H^q(x,\xi,t) &= F_1^q(t) \quad \int_{-1}^{1} dx \tilde{H}(x,\xi,t) = G_A^q(t) \\ \int_{-1}^{1} dx E^q(x,\xi,t) &= F_2^q(t) \quad \int_{-1}^{1} dx \tilde{E}(x,\xi,t) = G_P^q(t) \end{aligned} \tag{2.14}$$

where F_1^q,F_2^q are the elastic Dirac and Pauli form factors, and G_A^q,G_P^q are the axial and pseudo-scalar form factors for each quark flavour q. This description of GPDs is useful not only as an indicator of GPDs in the context of more widely-known objects, but also serves as a useful anchor to the discussion of a parameterisation of GPDs laid out in chapter 6. This is because it allows the GPD to be written in a factorised form [GPV01] e.g.

$$H^q(x,\xi,t) = H^q(x,\xi) \cdot F_1^q(t) \tag{2.15}$$

$$F_q(\alpha,\beta,t) = F_q(\alpha,\beta)\,\frac{1}{|\beta|^{\alpha' t}} \tag{2.16}$$

2.1.3 GPDs and the Spin Structure of the Nucleon

The goal of the HERMES experiment, as stated in chapter 1, is the investigation of the spin structure of the nucleon. It is to this end that HERMES studies DVCS, and the motivation for this was originally shown in [Ji97b] from the relationship:

$$J^q\left(\mu^2\right) = \frac{1}{2}\lim_{t\to 0}\int_{-1}^{1} dx\; x\left[H^q(x,\xi,t,\mu^2) + E^q\left(x,\xi,t,\mu^2\right)\right] \tag{2.17}$$

which relates the sum of the second moments of GPDs H and E to the total angular momentum of the quarks in the nucleon J_q at the limit $t \to 0$. It should be noted that if it were possible to obtain values for H and E and thus calculate the total angular momentum of the quarks in the nucleon, it would represent a significant step forward in the understanding of the spin structure of the nucleon, by means of equation 1.1.

2.2 Accessing GPDs via DVCS at HERMES

Deeply Virtual Compton Scattering (DVCS) is the process by which the incoming lepton in DIS scatters from a quark in the nucleon, which is for interpretive purposes removed from the nucleon with momentum fraction $x+\xi$ and replaced with momentum fraction $x-\xi$ so that the entire momentum transfer from the during the process is 2ξ. The struck quark emits a real photon before being re-absorbed into the nucleon.

Mentioned briefly at the beginning of this chapter, DVCS is not the only process in the HERMES measurement range that satisfies the requirement $eP \to e'\gamma P'$. The most significant background process is known as Bethe-Heitler (BH) scattering [KN02], a Deeply-Inelastic Scattering (DIS) process that interferes with the DVCS interaction on the amplitude level, so that the obtained cross section amplitude σ is proportional to the total scattering amplitude $|\tau|^2$, written as:

$$\sigma \sim |\tau|^2 = |\tau^2_{\mathrm{BH}}| + |\tau^2_{\mathrm{DVCS}}| + |\tau_{\mathrm{int}}| \tag{2.18}$$

where τ_{BH} and τ_{DVCS} refer to the pure BH and DVCS amplitudes respectively and $\tau_{\mathrm{int}} = \tau_{BH}\tau^*_{DVCS} + \tau_{DVCS}\tau^*_{BH}$ is the interference term. Studies have shown that, at HERMES energies, the BH term is massively dominating and whilst BH is calculable in QED and could be subtracted from the cross section, the errors introduced would render the DVCS term of the cross section useless. It is thus beneficial at HERMES only to study the interference term. A mathematical description of this interference term shows that [BMK02]

$$\tau_{\mathrm{int}} = \frac{\pm e^6}{x_B y^3 p_1(\phi) p_2(\phi) t} \times \left\{ c_o^{\mathrm{int}} + \sum_{n=1}^{3} [c_n^{\mathrm{int}} \cos(n\phi) + s_n^{\mathrm{int}} \sin(n\phi)] \right\} \tag{2.19}$$

where $y = \frac{\nu}{E_{\mathrm{beam}}}$ is the fraction of the beam energy carried by the virtual photon, the $\pm$ relates to the beam charge and $p_{1,2}(\phi)$ are the lepton propagators. The Fourier

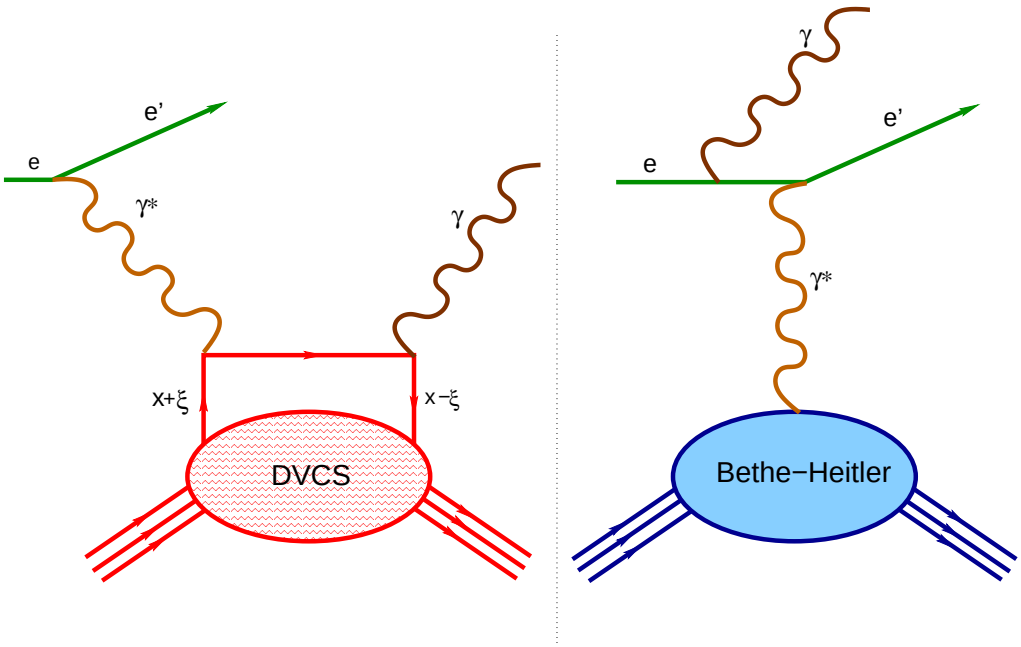

Figure 2.3: Left — the DVCS process. In this process, the incoming lepton (e) scatters by means of a virtual photon (γ^*) from a quark with longitudinal momentum fraction $x + \xi$ which is taken outside the nucleon blob. The quark then emits a real photon (γ) and returns to the nucleon with longitudinal momentum fraction $x - \xi$. Right — the competing Bethe-Heitler process. In this process (which has identical initial and final states to DVCS) the lepton radiates a real photon either before (shown) or after (not shown) scattering from the nucleon as a whole by means of a virtual photon. Only DVCS permits the extraction of information of GPDs.

coefficients from this equation show a linear dependence on Compton Form Factors (CFFs), which are convolutions of GPDs with "hard-scattering kernels", $C^{\pm}$ such that

$$\begin{pmatrix} \mathcal{H} \\ \mathcal{E} \end{pmatrix}(\xi,t) = \int_{-1}^{1} C^{-}(x,\xi)\,dx \begin{pmatrix} H \\ E \end{pmatrix}(x,\xi,t) \tag{2.20}$$

$$\begin{pmatrix} \tilde{\mathcal{H}} \\ \tilde{\mathcal{E}} \end{pmatrix}(\xi,t) = \int_{-1}^{1} C^{+}(x,\xi)\,dx \begin{pmatrix} \tilde{H} \\ \tilde{E} \end{pmatrix}(x,\xi,t) \tag{2.21}$$

where the RHS of each equation above expands to

$$C^{\pm}F = \sum_{q=u,d,s} C^{\pm} e_q^2 F^q \tag{2.22}$$

for each GPD F and quark flavour q and where $C^{\pm}$ expands to:

$$C^{\pm} = \frac{1}{x-\xi-i\epsilon} \pm \frac{1}{x+\xi-i\epsilon} + \mathcal{O}(\alpha) \tag{2.23}$$

in which ϵ is a standard mathematical non-zero term allowing $C^{\pm}$ to exist even when $x = \xi = 0$. This allows the split of the CFFs into real and imaginary parts, thus:

$$\Re(\mathcal{F}) = \mathcal{P}\int_{-1}^{1} dx \left(\frac{F}{x-\xi} \pm \frac{F}{x+\xi}\right) \tag{2.24}$$

$$\Im(\mathcal{F}) = F(x,\xi) \pm F(x,-\xi) \tag{2.25}$$

where $\mathcal{P}$ denotes Cauchy's principle value and terms of $\mathcal{O}(\alpha)$ are ignored.

It is then these real and imaginary parts of CFFs which can be written in terms of observables at HERMES, and which allow HERMES to access GPDs. Note that in section 2.3 any observable that relates to the real part of a CFF can access only an integral value of the GPDs at a given ξ, whereas an observable that contains an imaginary part of the CFF allows access to the GPD along the line $x = \pm\xi$.

2.3 Observable Asymmetries from DVCS at HERMES

When "observable asymmetries at HERMES" are discussed, the asymmetries are those in the photon production of the reaction, measured in the azimuthal angle around the direction of the virtual photon in the DVCS interaction. A more detailed discussion of the DVCS angles and directions can be seen in chapter 5, and figure 5.2 in particular describes exactly the angles ϕ and ϕ_s. Here is presented a brief overview of the four observables measured at HERMES, with their dependence on GPDs included for completeness. The Transverse Target Spin Asymmetry 2.3.2 is discussed in more detail in chapters 5 and 6.

2.3.1 Beam-Dependent Observables

The beam-dependent asymmetries from the DVCS interaction are the most well understood quantities and the Beam Spin Asymmetry has been measured by more than one experiment [Ste01]. They involve predominately the CFF (GPD) $\mathcal{H}$ (H) and both use an unpolarised target.

Beam Spin Asymmetry

The Beam Spin Asymmetry (BSA), where there is an azimuthal asymmetry that has a dependence upon a positive/negative beam helicity $\overrightarrow{e}$ / $\overleftarrow{e}$ is defined as:

$$A_{BSA}(\phi) = \frac{d\sigma\left(\overrightarrow{e},\phi\right) - d\sigma\left(\overleftarrow{e},\phi\right)}{d\sigma\left(\overrightarrow{e},\phi\right) + d\sigma\left(\overleftarrow{e},\phi\right)} \tag{2.26}$$

and is measured using a longitudinally-polarised lepton beam and, usually, an unpolarised Hydrogen target. This observable has also been measured at HERMES on heavier nuclear targets such as Nitrogen, Krypton and Xenon. It can be related to GPDs as:

$$A_{BSA} \approx \ Im\left[F_1\mathcal{H} + \frac{x_B}{2-x_B}(F_1(t)+F_2(t))\tilde{\mathcal{H}} - \frac{t}{4M^2}F_2(t)\mathcal{E}\right] \tag{2.27}$$

where the terms relating to $\tilde{\mathcal{H}}$ and $\mathcal{E}$ are suppressed at the low x_B and t values found

at HERMES allowing a simpler relationship to be written:

$$A_{BSA}(\phi) \approx A_{BSA}^{\sin(\phi)} \cdot \sin(\phi) \propto F_1 \cdot \Im\mathcal{H} \cdot \sin(\phi). \tag{2.28}$$

Often the quantity A_{BSA} is referred to as A_{LU}.

The Beam Spin Asymmetry has been measured by HERMES [A$^+$01a] (see figure 2.4), in addition to being measured at CLAS at Jefferson Lab in the USA [Ste01]. It is the most-known of the DVCS asymmetries.

Beam Charge Asymmetry

The Beam Charge Asymmetry (BCA) in DVCS, an azimuthal asymmetry in the production of the real photon from the process that depends upon the lepton beam charge $e^{\pm}$, is defined as:

$$A_{BCA}(\phi) = \frac{d\sigma\left(e^+,\phi\right) - d\sigma\left(e^-,\phi\right)}{d\sigma\left(e^+,\phi\right) + d\sigma\left(e^-,\phi\right)}. \tag{2.29}$$

BCA is measured by scattering a charged lepton beam off an unpolarised Hydrogen target. HERMES has been the only experiment to publish [A$^+$07a] a BCA result at the time of writing — see figure 2.5. This is due to the unique setup of the HERA accelerator which can be filled with both electrons and positrons. While there are indications that other facilities may be able to reproduce such a result in the future, none are available at present. The BCA result is important because the azimuthal distribution of photons relating to it can be approximated by a cosine dependence. The amplitude of this dependence is related to the real part of the CFF $\mathcal{H}$ convoluted with the Pauli Form Factor F_1 in a similar fashion the relationship between the BSA amplitude and the imaginary part of $\mathcal{H}$ (see eqn. 2.27):

$$A_{BCA}(\phi) \approx A_{BCA} \cdot \cos\phi \propto F_1 \cdot \Re\mathcal{H} \cdot \cos\phi. \tag{2.30}$$

Often, the quantity A_{BCA} is referred to as A_C.

2.3.2 Target Spin-Dependent Asymmetries

The target spin-dependent asymmetries in DVCS are considerably more complicated than those arising from the beam conditions. They relate to CFFs and thus GPDs

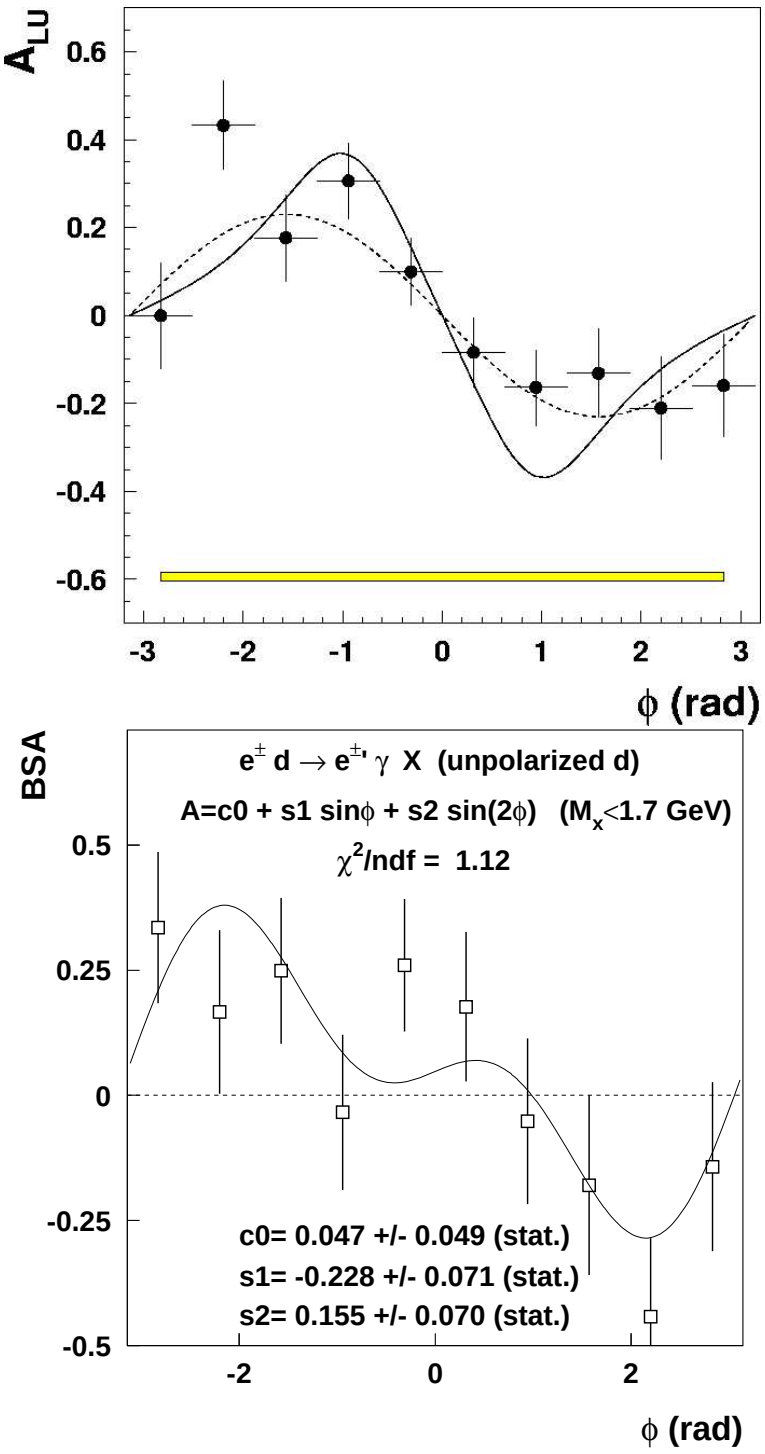

Figure 2.4: Two BSA results arising from measurements at HERMES. The upper plot shows the azimuthal dependence for the BSA of the DVCS interaction on unpolarised Hydrogen. This plot shows two lines. The dashed line represents a $\sin\phi$ dependence with an amplitude of 0.23 whilst the solid line is the result of a model calculation from Ref. [GPV01]. This figure is taken from [A^+01a]. The lower plot is a preliminary result showing the azimuthal dependence for the BSA of the DVCS interaction on unpolarised Deuterium. The fitting function in this case is more complicated to take into account the more complicated structure of Deuterium. This figure is taken from [Kra05].

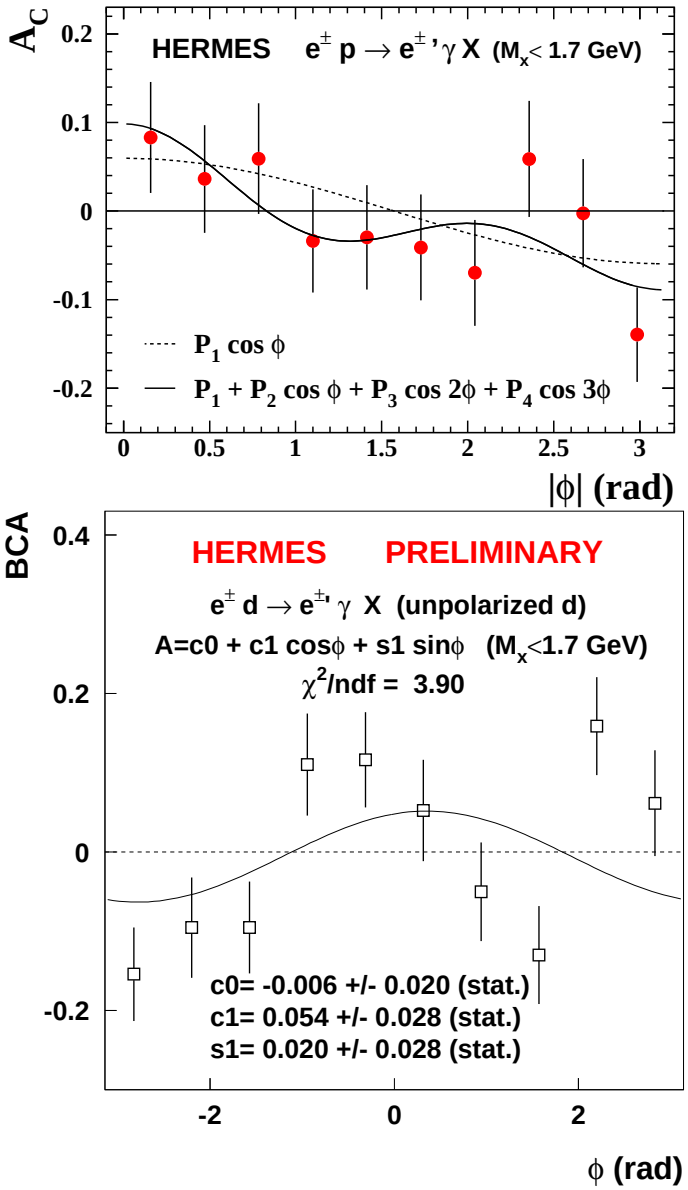

Figure 2.5: BCA results from investigations at HERMES. The upper plot shows the dependence of the BCA from Hydrogen on azimuthal angle ϕ. The solid curve shows the result of a four parameter fit while the dashed line shows the pure $\cos\phi$ dependence. The plot is taken from ref. [A$^+$07a]. The lower plot show the same observable for the interaction involving Deuterium data. The line shows the fit with the parameters marked on the plot. It is taken from ref. [Kra05]. The upper plot has undergone symmetrisation about $\phi = 0$ so as to remove any odd terms from the data and decrease the statistical error.

not only through the Pauli Form Factor F_1 but also the Dirac Form Factor F_2 and can be used to access not only the unpolarised CFF (GPD) $\mathcal{H}(H)$ but also $\mathcal{E}(E)$ and their polarised equivalents $\tilde{\mathcal{H}}$ and $\tilde{\mathcal{E}}$ ($\tilde{H}$ and $\tilde{E}$).

Longitudinal Target Spin Asymmetry

The Longitudinal Target Spin Asymmetry (LTSA) in DVCS is the asymmetry in the azimuthal distribution of the produced photon arising from the interaction of a lepton beam with a longitudinally polarised Hydrogen or Deuterium target:

$$A_{LTSA} = \frac{d\sigma\left(\vec{T},\phi\right) - d\sigma\left(\overleftarrow{T},\phi\right)}{d\sigma\left(\vec{T},\phi\right) + d\sigma\left(\overleftarrow{T},\phi\right)} \tag{2.31}$$

where the left (right) arrow relates to a target that is positively (negatively) polarised in the direction of the virtual photon involved in the interaction. The LTSA has an approximate sinusoidal dependence and its relationship to CFFs, and thus GPDs. The LTSA has a very complicated dependence on CFFs and GPDs, a dependence too complicated to reproduce here given that LTSA measurements are not the main work of this thesis. Instead, more details about LTSA measurements at HERMES can be found in reference [Kop06]. The quantity A_{LTSA} is often referred to as A_{UL}.

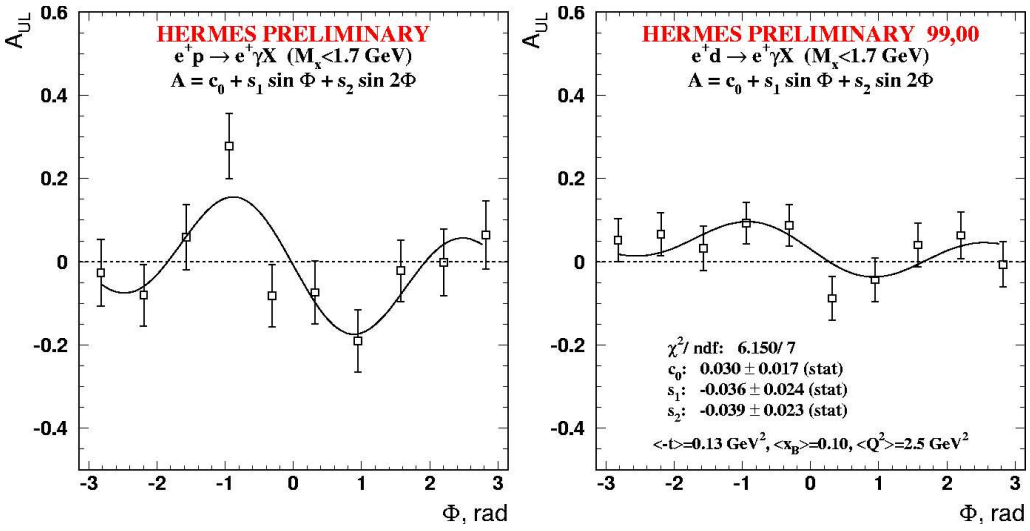

Figure 2.6: LTSA results released at HERMES. The left plots shows the dependence on ϕ of the LTSA on Hydrogen, the right plot shows the same information but for Deuterium. Both figures are taken from ref. [Kop06]. Both asymmetries are related to GPDs in a complicated manner, with both the first and second sin moments yielding information about CFFs.

Transverse Target Spin Asymmetry

The Transverse Target Spin Asymmetry (TTSA) in which the asymmetry results from the interaction of a single-charge lepton beam with a target which is polarised

in a direction transverse to the incoming beam, approximated as the direction of the virtual photon [DS05]. It is defined as:

$$A_{TTSA} = \frac{d\sigma\left(\phi, \phi_s\right) - d\sigma\left(\phi, \phi_s + \pi\right)}{d\sigma\left(\phi, \phi_s\right) + d\sigma\left(\phi, \phi_s + \pi\right)} \tag{2.32}$$

where ϕ is the azimuthal angle, defined above as the angle between the produced photon and the virtual photon and ϕ_s is the angle between the lepton plane and the produced photon. For a more detailed explanation of these angles, see chapter 5.

The TTSA is different to the other observables described above as it involves not only of two asymmetry amplitudes, but two angles, with a more complicated approximation necessary in order to relate the measured asymmetry to any theoretical quantity. In eqns. 2.34 and 2.35, M_N refers to the mass of the nucleon.

$$A_{TTSA} \approx A_1 \sin(\phi - \phi_s)\cos(\phi) + A_2 \cos(\phi - \phi_s)\sin(\phi) \tag{2.33}$$

where

$$A_1 \propto -\frac{t}{4m_N^2} \cdot \left(F_2 \cdot \Im\mathcal{H} - F_1 \cdot \Im\mathcal{E}\right) \tag{2.34}$$

$$A_2 \propto -\frac{t}{4m_N^2} \cdot \left(F_2 \cdot \Im\tilde{\mathcal{H}} - F_1 \cdot \Im\tilde{\mathcal{E}}\right) \tag{2.35}$$

Equations (2.33), (2.34) and (2.35) show the dependence of the TTSA on CFFs. These are approximations, but as with beam spin- and charge-dependent asymmetries, these dependences are quite complicated and the above equations do not show any dependences that are kinematically or otherwise suppressed.

Later in this thesis (Chapter 5) there an analysis is presented of the possibilities the TTSA presents with regards to an extraction of a constraint on the total angular momentum of the up and down quarks in the nucleon. Previous results for 2002-04 data from the HERMES experiment can be seen in figure 2.7 taken from ref. [YMMN06]. The quantities $A_{1,2,TTSA}$ is often referred to as A_{UT}, with the trigonometric dependence specified in order to differentiate between the two amplitudes $A_{1,2}$ of most interest.

This chapter has shown the importance of GPDs to physical quantities, and described how they can be accessed at HERMES through the consideration of the DVCS process. There has been a brief description of the observables measured at HERMES that arise from the DVCS process. The next chapter describes the HERMES experimental setup. More details on DVCS can be found in chapter 5 which

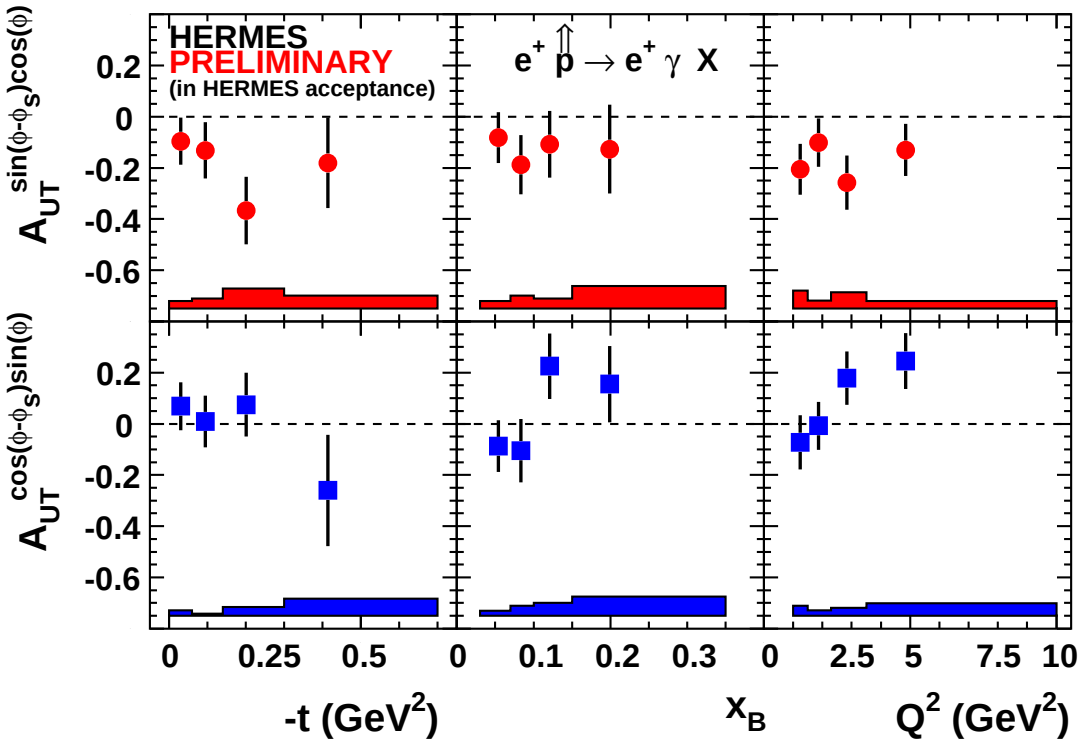

Figure 2.7: TTSA as a function of the HERMES kinematic range. Picture is taken from reference [Ye06]. The theory curves on the plot relate to theoretical predictions for various values of J_u with J_d set to 0. These predictions and their implications are discussed further in chapter 6.

describes in detail an analysis carried out on the TTSA observable, and more details on GPDs and their links to physical quantities can be found in chapter 6.

Chapter 3

The HERMES Experiment

During the construction phase of HERA, a new experiment was proposed, a fixed-target experiment that would investigate the spin crisis arising from the measurements made at CERN's European Muon Collider experiment. In 1993, HERMES (HERa MEasurement of Spin) started to undergo construction and began taking data in 1995 [Due95]. Over the next fifteen years, the HERMES physics scope would be expanded to include the investigation of further hadronic information. HERMES has several novel aspects to it that allow it to claim its position at the forefront of spin physics and hadron physics in its kinematic range—foremost amongst these are the nature of its beam and its unique target. Over its lifetime the HERMES experiment has been upgraded from its original design, with the most recent and final upgrade taking place in the HERA shutdown of 2005 when a recoil detector was installed in the target region. This was done in order to allow HERMES to detect the recoil proton involved in DVCS and so make an exclusive measurement of the interaction [ea97]. This detector is detailed in chapter 4. This chapter details the experimental setup of the spectrometer in the period 2002-2005. This is the time period over which the data analysed in chapter 5 was taken.

3.1 The HERA Storage Ring

The HERA storage ring in Hamburg, Germany is a part of the DESY (Deutsches Elektronen SYnchrotron) institute. It has a circumference of 6.3 km and features four experimental halls that allow access to the ring itself, which is buried under the west of Hamburg at depths of up to 30 m. Originally there were four experiments on the ring, ZEUS, HERMES, HERA-B and H1, but HERA-B was decommissioned

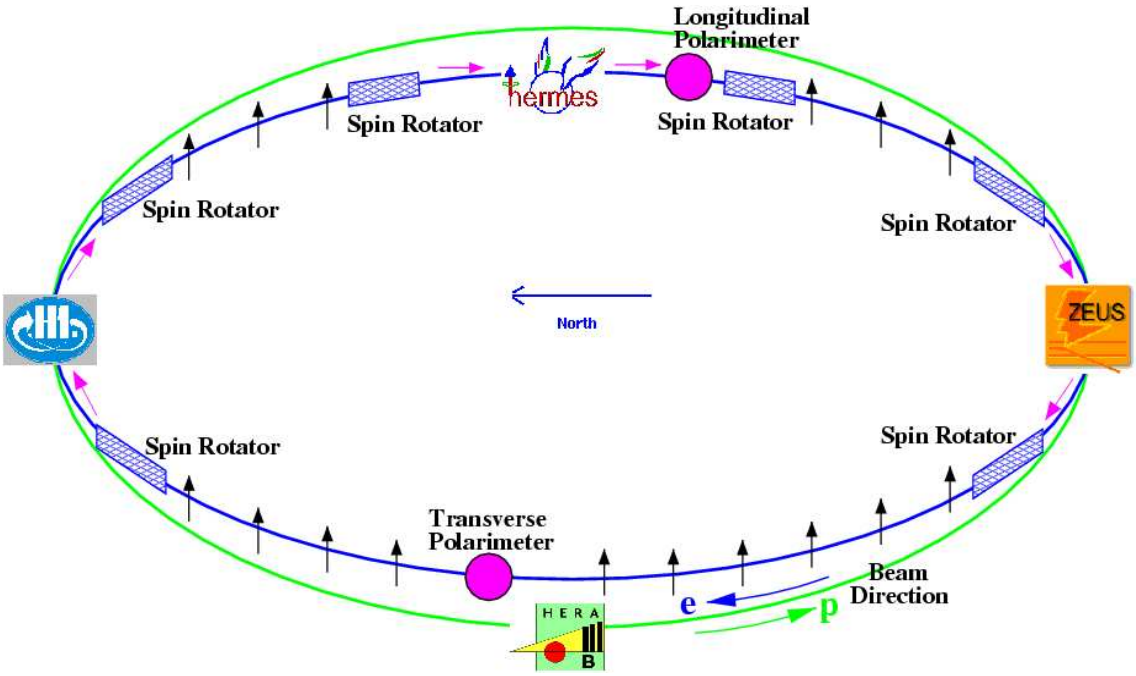

Figure 3.1: The HERA ring, showing the positions of the experiments, the spin-rotators and the polarimeters. HERA-B is no longer operational. HERMES is located in the Eastern experimental hall, under Hamburg's Volkspark.

in 2003. With HERMES based in the eastern experimental hall of the ring, this leaves two other experiments — ZEUS and H1. Both of these are very different in nature to HERMES, being collider experiments that utilise a 920 GeV proton beam in the storage ring which collide with the 27.56 GeV lepton beam to produce reaction products, in comparison to the HERMES gaseous target which sits in the lepton beam. See figure 3.1.

3.1.1 The Polarised Lepton Beam

The HERA lepton beam is operated at a momentum of 27.56 GeV and can be operated as either a positron or electron beam. In the period 1995-2000 the beam was made up of positrons with the exception of a short period during 1998 when electrons were used. The brevity of this period was caused by the fact that negatively charged electrons attracted positively charged dust on its path around the ring, which had a severe negative influence on the lifetime of the beam. The HERA accelerator was upgraded during 2001 and in the run period 2002-2005, positrons were used in 2002-04, with electrons filled into the ring in 2005, changed back to positrons in the winter shutdown of 2006. Positrons remained in HERA until the end of data taking in June 2007, when HERA was shut down.

Production of the Beam

The positron/electron beam is accelerated through DESY's LinAc II linear accelerator to 450 MeV. At this energy they are injected into the DESY-II storage ring where they undergo further acceleration to 7.5 GeV. They are then transferred to the final pre-acceleration stage in the PETRA storage ring where they are accelerated to 12 GeV before being injected into HERA where they undergo a final acceleration to the operating energy of 27.56 GeV.

Characteristics of the Beam - Lifetime

While the storage ring is capable of storing the particles within it for a long time, there are several contributions which cause a deterioration in the lifetime of the beam. Whilst the HERMES target is gaseous and therefore does not stop the beam in the way that a traditional liquid or solid target would, it does significantly contribute to the deterioration of the lepton beam. If the lifetime of the beam is τ then it is governed by two contributions:

$$\frac{1}{\tau} = \frac{1}{\tau_{HERMES}} + \frac{1}{\tau_{HERA}} \tag{3.1}$$

The lifetime of the beam follows an exponential decay during which the contribution from the HERMES target must not be more than 45 hours [Col07]. This corresponds to a target density of 0.162×10^{15} nucleons/cm^2. Once the current of the beam drops below 14 mA, the target density is increased to 0.313×10^{16} nucleons/cm^2 which corresponds with a beam lifetime contribution $\tau_{HERMES} = 2$ hours. Other factors that deplete the beam from the rest of the HERA system include the interaction of the beams in the collision points at ZEUS and H1 and, in the electron beam case, arcing voltages from the high-frequency pumps used in the accelerator system. For further discussion of the beam, the z-direction is taken as the direction of the beam momentum, the y- and x-directions are taken as the transverse directions, the y-direction being vertical.

Characteristics of the Beam — Spin

Since the beampath is necessarily curved, the Sokolov-Ternov (S-T) effect [ST64] causes an initially unpolarised beam to become polarised. The S-T effect is the eventuality of a small asymmetry in the probability of lepton spin-flipping during the emission of synchrotron radiation caused by the traversal of the arcs of the

ring. The vector of polarisation rotates to become parallel(↑)/anti-parallel (↓)to the direction of the magnetic fields emitted by the HERA bending magnets depending upon whether the beam is positively/negatively charged. The polarisation is defined as

$$P = \frac{N^{\uparrow} - N^{\downarrow}}{N^{\uparrow} + N^{\downarrow}} \tag{3.2}$$

where $N^{\uparrow,\downarrow}$ are the numbers of e.g. positrons with polarisation $(\uparrow, \downarrow)$ and this polarisation increases exponentially with time (t) with the dependence:

$$P = P_{ST} \cdot \left(1 - \exp\left\{ - \frac{t}{\tau_{ST}} \right\}\right) \tag{3.3}$$

where P_{ST} is the theoretically maximum polarisation possible polarisation and τ_{ST}, the characteristic rise time, which has dependencies on the bending radius, the energy of the beam and a further dependence on P_{ST} . In the case of the HERA storage ring, this works out to be ∼40 minutes.

These are not the only effects which govern the polarisation in the HERA ring. There are many small effects which conspire to reduce the level of polarisation in the ring including, but not limited to, non-perfect alignment of the magnetic fields which govern the bending of the beam around the arcs of the beampath, proton-lepton interactions at the collision points used by ZEUS and H1 and energy loss from leptons due to the emission of synchrotron radiation as the beam path curves which gives rise to non-aligned magnetic fields in the beam itself. All this means that the maximum achievable polarisation in the storage ring is significantly lower than the theoretical maximum ($\approx 90\%$) and, although values of ∼70% have been achieved in previous running conditions, since the 2001 upgrade polarisation levels have changed considerably. Average values for the positron data are ∼35%, dropping to ∼25% for the electron beam used in 2005. In later years, 2006 and 2007, the polarisation increased once more to around $\approx 40\%$.

Whilst the natural transverse polarisation of the beam can be desirable, the cross section for transverse-spin lepton beams is highly suppressed compared to the the longitudinal cross-section so a longitudinally polarised beam is more useful. In order to achieve this, the experiments on the ring have assemblages of magnets, called spin rotators [BS86], installed either side of each experiment, which gradually change the spin of the beam from the transverse direction to the longitudinal direction. After exiting each experiment, the beam spin is returned to the transverse direction, as this is the natural direction for the beam spin to occur as the particles travel around

the ring, see figure 3.1. A lot of the measurements taken at HERA require the beam to be polarised, or require the polarisation of the beam to be balanced so that the net beam polarisation is 0%. In order to be able to use the polarised beam, or compensate for the polarisation, accurate measurements of the polarisation are required and these are provided by two polarimeters at HERA: the transverse polarimeter and the longitudinal polarimeter.

The Polarimeters

There are two polarimeters on the HERA storage ring - one which is positioned next to the HERA-west control room and measures the transverse polarisation and one which is positioned next to the HERMES experiment and measures the longitudinal polarisation. See fig 3.1. The effect of the spin rotators on the HERA ring is merely to move the direction of the polarisation from the transverse to the longitudinal direction. Since the magnitude of the polarisations should otherwise be the same, the longitudinal and transverse polarimeters should measure the same absolute polarisation and this means that a cross check between the two values is possible.See figure 3.2. Both of these polarimeters exploit the fact that the cross section of Compton scattering of circularly polarised photons off polarised leptons is spin-dependent, but in different ways.

The Transverse Polarimeter

The Transverse Polarimeter (TPol) [B$^+$94] uses a laser source for photons which pass through a Pockels cell to produce circularly polarised photons. The photons are then incident on the y-polarised lepton beam and the backscattered photons are detected in a calorimeter. During a measurement, the polarisation of the photons is flipped at $\sim 83Hz$ which creates an asymmetry in the y-distribution of the photons in the calorimeter. This asymmetrical distribution

$$\Delta y(E_\gamma) = \frac{1}{2}(\langle y(E_\gamma)\rangle^+) = \Delta S_3 \cdot P_y \cdot \Pi_y(E_y) \tag{3.4}$$

which is dependent upon the energy of the photons E_γ, the polarisation of the lepton beam in the y-direction and the mean magnitude of the circular light polarisation. The relationship to E_γ on the right hand side of equation 3.4 is subsumed in a second function Π_y, known as the analysing power of the polarimeter.

The Longitudinal Polarimeter

In a similar manner to the TPol, the Longitudinal Polarimeter (LPol) [B$^+$02b] uses circularly-polarised photons, but rather than a spatial asymmetry, the LPol measures an energy asymmetry. Using a laser to produce photons and inducing circular polarisation in a fashion similar to that used in the TPol, the LPol detects around 1000 backscattered photons per laser pulse. It measures an asymmetry

$$A(\Delta S_3, P_z) = \Delta S_3 \cdot P_z \cdot \Pi \tag{3.5}$$

where the analysing power Π is a function which relates the longitudinal polarisation P_z to the polar scattering angle of the photon detected in the calorimeter and ΔS_3 is again the mean magnitude of the circular polarisation of the incident photon.

3.2 The Polarised Target

One of the pieces of apparatus that helps to make HERMES unique is the polarised target. The target setup can be filled with Hydrogen, which can be polarised or unpolarised, depending upon physics needs, or filled with unpolarised heavier gases like Nitrogen or Xenon. The subject of the physics analysis of this thesis, however, is an observable extracted only for a transversely polarised Hydrogen target, and consequentally the rest of this description will focus on the target used for that purpose.

One of the main considerations that had to be taken into account in the planning of the HERMES experiment is that, unlike some other experiments that measure similar physical quantities such as COMPASS, HERMES is placed on a storage ring and must take the needs of the other users into account. For this reason, a solid or liquid target cannot be used, since such a target stops the beam, negating the storage ring and rendering the other experiments on the ring inoperable. A solid or liquid target would also necessarily introduce impurities into the target material, making analysis more difficult — such an effect has been observed in other experiments. This leaves a gaseous target as the type of choice for the experiment, meaning that the density of the target and hence the reaction rate for the experiment is not as high as it would otherwise be. This choice of target is serendipitous however, as the gaseous nature of the target does allow the target material and density to be changed without access to the experimental setup, even during running. In addition to filling the storage cell with Krypton or Nitrogen gas, the pump system used in

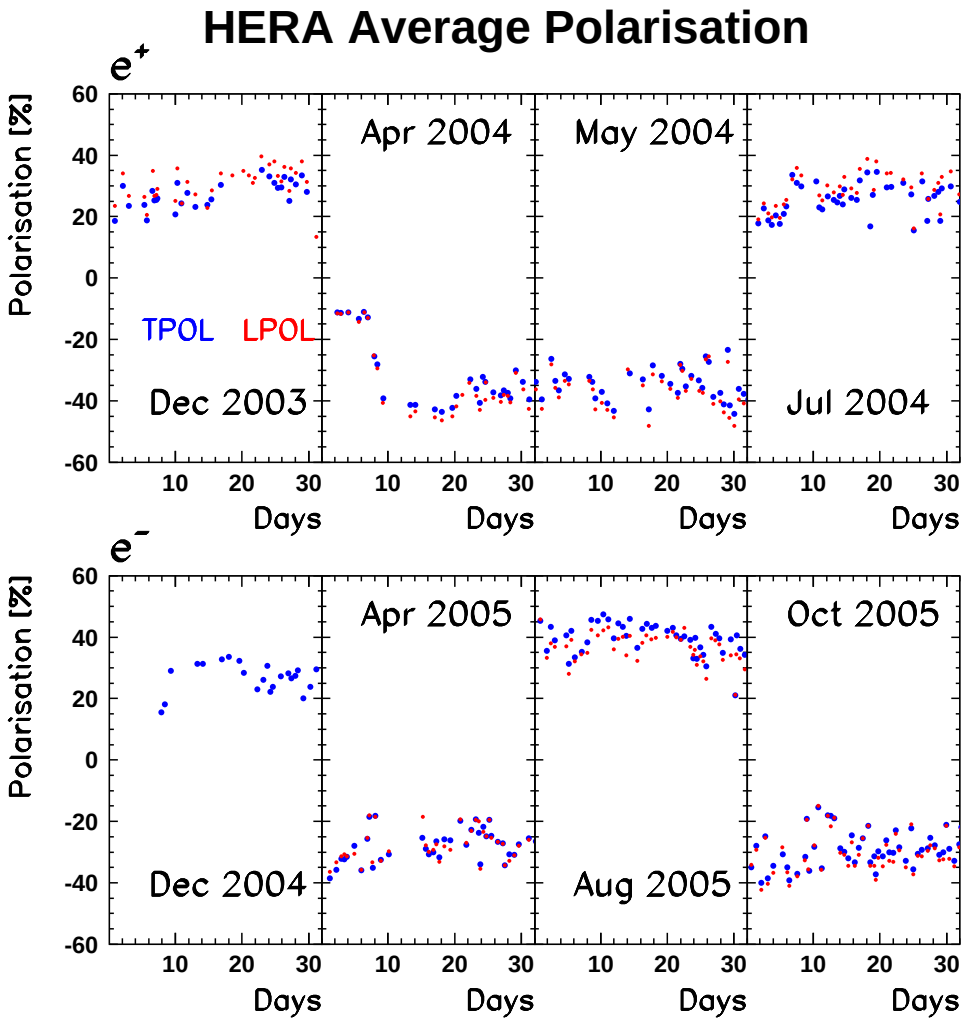

Figure 3.2: The polarisation of HERA over selected months showing both positron and electron data as seen by both polarimeters. Both polarimeters show good agreement, save for Dec. 2004, when the LPol was non-functional.

the target can be used to fill the target to greater densities as the beam current decreases, increasing the reaction rate substantially. Standard operating procedure is to increase the target density when the HERA beam current reaches 14 μA [Col07], leaving HERMES as the primary beam user for the rest of the fill period.

The Atomic Beam Source

The atomic beam source, or ABS, (fig. 3.3) is the piece of apparatus [ea03] that is used to fill the HERMES storage cell with disassociated, polarised Hydrogen atoms. It consists of 5 distinct parts that are capable of supplying the target with

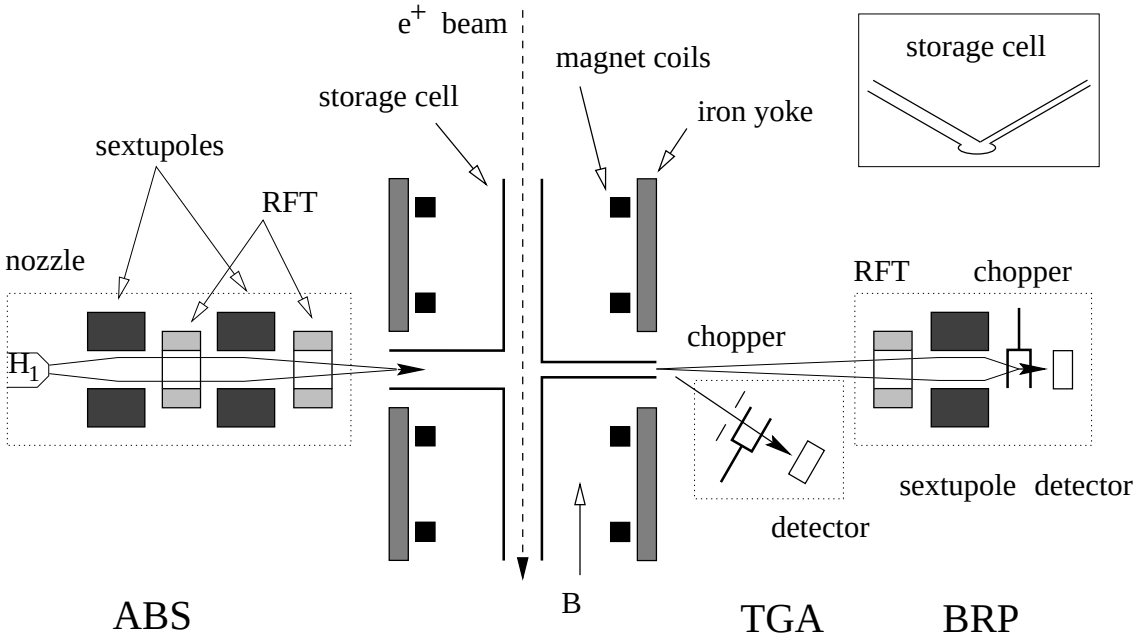

Figure 3.3: A schematic diagram of the target system, showing the various parts of the HERMES polarised target. The ABS feeds polarised Hydrogen atoms into the storage cell, which is subject to the magnetic field from the target magnet. The TGA and BRP monitor the levels of polarisation by extracting some gas from the storage cell and measuring how polarised it is.

spin polarised protons by making use of the hyperfine splitting levels in Hydrogen. Pure H_2 gas is first passed through a disassociator which renders the gas into its monatomic state with an 80% success rate. This monatomic gas is then passed through a skimmer-collimator that causes the monatomic Hydrogen to be formed into a vapour jet. This is all done at a temperature of 100K, and a thin layer of frozen water on the nozzle of the jet helps to prevent the monatomic Hydrogen from recombining. In this state, and in the absence of an external magnetic field, the Hydrogen is split into 4 states. This arises from the spins of the proton and electron, with the four states corresponding to the four combinations of (P_p,P_e)=($\pm\frac{1}{2}, \pm\frac{1}{2}$). Upon exiting the jet-forming system, the hydrogen passes into a sextupole magnetic system which draws Hydrogen with electron spin $+\frac{1}{2}$ onto the magnetic axis. Following this separation of Hydrogen atoms into 2 groups with a distinct electron polarisation, but a theoretical proton polarisation P_p=0, high frequency transition units are used to invert the polarisations of the atoms with $(P_p, P_e) = (\pm\frac{1}{2}, +\frac{1}{2})$ and $(P_p, P_e) = (\pm\frac{1}{2}, -\frac{1}{2})$, leaving two distinct groupings of gas with (P_p,P_e)=($+\frac{1}{2}, \pm\frac{1}{2}$) or ($P_p$,$P_e$)=($-\frac{1}{2}, \pm\frac{1}{2}$). These groups of gas are then injected into the target, providing a polarised target gas for data taking.

The Storage Cell

As the HERMES storage cell [B$^+$03a] is positioned as a part of the HERA storage ring, a lot of effort has gone into the design and implementation of the storage cell in order to provide the maximum possible data taking opportunity to HERMES whilst minimising any adverse influence on other experiments on the ring. The storage cell itself consists of a smooth aluminium tube with 75 μm-thick walls and an elliptical cross section with a major axis of 21 mm and a minor axis of 8.9 mm. In an effort to preserve the monatomic nature of the injected gas and prevent depolarisation, the tube is cooled to 100K using cooling rails and coated internally to minimise surface effects. The temperature is measured by four resistors which are monitored continually by a part of the HERMES data acquisition environment. The storage cell is 400 mm long and is connected to the beampipe by wake-field suppressors which act to minimise destabilising radio frequency effects which would otherwise arise from the discontinuities. These wakes would otherwise heat the storage cell, possibly melting the cell walls, and destroy the beam orbit, ruining the fill and possibly causing damage to the experimental apparatus. There exist various apertures onto the storage cell, one of which is used to fill the cell with unpolarised Hydrogen when necessary, and others used to monitor the target gas. These monitoring apertures are offset from the input apertures by 120^o in order to allow the target gas to attain thermal equilibrium with the storage cell.

The Transverse Target Magnet

The transverse target magnet (figure 3.4) surrounds the storage cell and provides a uniform, vertical 297mT magnetic field across the dimensions of the storage cell [Tai06] in order to maintain the polarisation of the target. It is of conventional design, with one pole above and one pole below the storage cell and a surrounding yoke. It operates under a supplied current of 545 A. The magnetic field fluctuates in the x-direction by 0.60 mT, the y-direction by 0.15 mT and the z-direction by 0.05 mT. It displays time-dependent behaviour due to heating effects, which cause the magnetic field to drop by up to 0.4 mT over a period of several hours. In order to correct for this, there is a correction coil—the so-called "Yoke-Coil"—which has a maximum field effect of 0.7 mT applied across the transverse target magnet. The current to this yoke coil is controlled through feedback from a hall probe located inside the bore of the transverse target magnet. The y-direction of the transverse magnetic field causes the lepton beam to be bent in the x-direction through the Lorentz force, in a similar fashion to the other magnets on the HERA ring. To

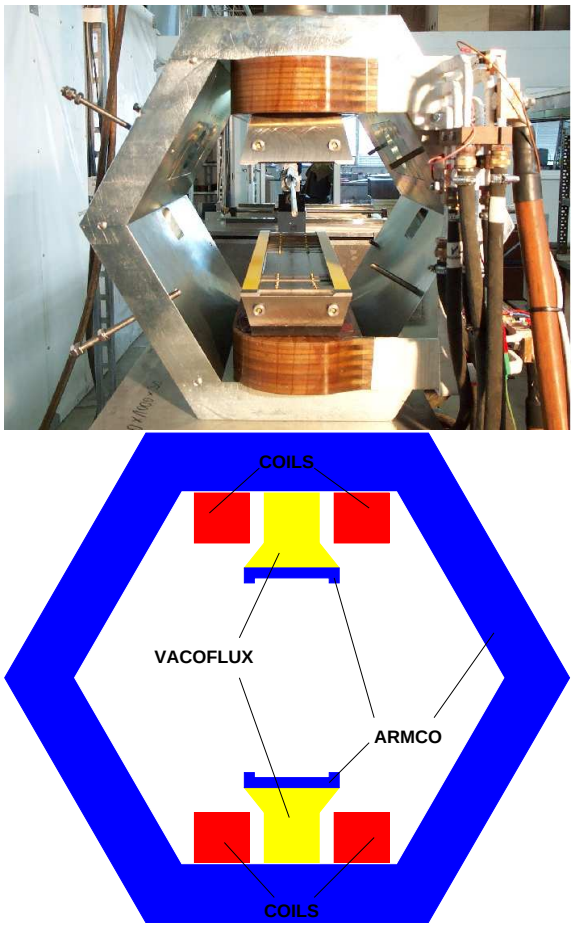

Figure 3.4: The transverse target magnet provides a uniform 297 mT dipolar field across the storage cell. The field is directed along the y-axis which causes the lepton beam to be bent in the x-axis direction by the Lorentz force. The yoke is made of ARMCO magnetic iron and the poles are made of VACOFLUX which is a trademark of the Vacuumschmelze Gmbh. Picture is taken from reference [Tai06].

counteract this influence on the beam, there are two small, compensatory dipole magnets placed before and after the storage cell which negate the deflection of the beam. The transverse magnetic field also causes the tracks caused by interactions in the storage cell to be deflected slightly. In order to correct for this unwanted effect, there are two techniques that can be applied, one which is based upon calculations made of known tracks during the data taking period, the other is applied from calculations based upon an accurate field map of the bore of the transverse magnet. This is discussed further in chapter 5.

The Breit-Rabi Polarimeter

The target gas at HERMES is closely monitored [B$^+$02a] since any target-spin-dependent asymmetry requires a measure of the polarisation of the target gas. There

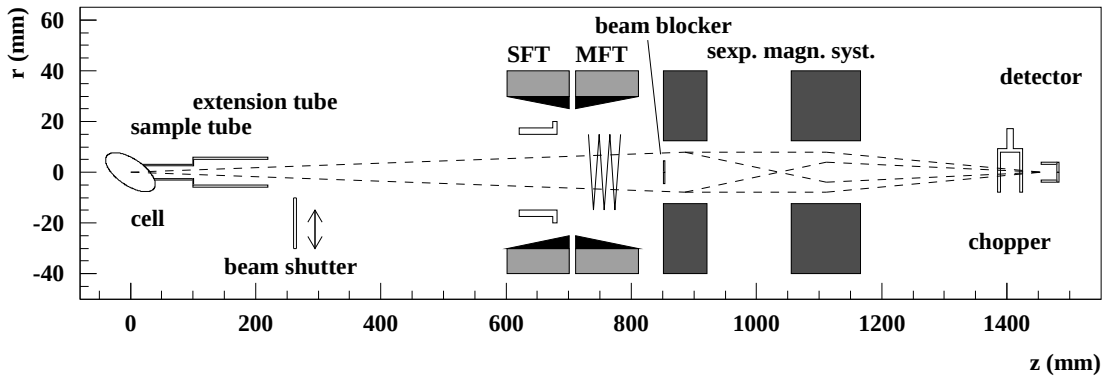

Figure 3.5: Schematic view of the Breit-Rabi Polarimeter with Strong Field Transition (SFT) and Medium Field Transition (MFT) units. The beam blocker at the magnetic field axis ensures 100% rejection of atoms with $P_e = +\frac{1}{2}$ from the measurement apparatus.

are two pieces of apparatus used to monitor the gas and the Breit Rabi Polarimeter (BRP) is one of them (fig. 3.5). Consisting of a set of transition chambers similar to those used in the ABS in order to select between hyperfine states in the Hydrogen gas, a sextupole magnet system that draws gas with $P_e = +\frac{1}{2}$ toward the detection system and a quadrupole mass spectrometer, the BRP is capable of sampling the atomic polarisation in the centre of the cell. In order to achieve a value for the average atomic polarisation, the value measured by the BRP P_α must be multiplied by correction factors c_P that are determined by Monte Carlo simulations of the flow of the gas along the cell tube.

$$P_{BRP} = c_P \cdot P_\alpha \tag{3.6}$$

The Target Gas Analyser

The second piece of apparatus [B$^+$03b] used to monitor the polarisation of the target gas is the Target Gas Analyser (see fig. 3.6). The input aperture of the Target Gas Analyser (TGA) is offset by 7^o to that of the BRP in order to avoid interference with the gas flow into that apparatus. It consists of a quadrupole mass spectrometer similar to that used in the BRP and is used to measure the flow of gas in the storage cell. The degree of disassociation of the target gas sample α_{TGA} is given by the flow of atoms ϕ_a normalised by the overall flow of atoms and molecules $\phi_a + \phi_m$:

$$\alpha_{TGA} = \frac{\phi_a}{\phi_a + \phi_m} \tag{3.7}$$

In addition to special calibration data taken by the spectrometer between fills of the

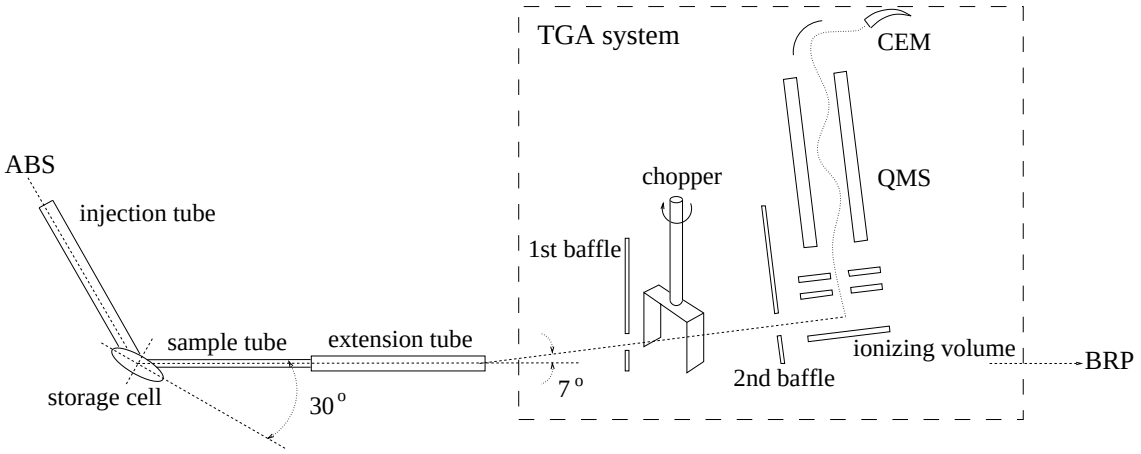

Figure 3.6: Schematic view of the Target Gas Analyser, with Quadrupole Mass Spectrometer (QMS) and Channel Electron Multiplier (CEM) which is used to allow single ion detection.

HERA ring this quantity can be used to calculate two further quantities, the degree of disassociation in absence of recombination of the gas arising from interaction with the cell walls, α_0, and the fraction of atoms which survive nuclear recombination within the cell, α_r.

Target Polarisation

Through consideration of the measurements of the BRP P_{BRP} and the TGA α_{TGA}, a value for the polarisation of the target gas P_T can be deduced:

$$P_T = \alpha_0[\alpha_r + (1 - \alpha_r)\beta]P_{BRP}. \tag{3.8}$$

In Eqn. 3.8, β refers to the ratio of nuclear polarisation produced by recombination of atomic Hydrogen into molecular Hydrogen to the contribution of polarisation from atoms that survive in the cell without recombination in the cell. This quantity cannot be measured directly at HERMES by the BRP which is only capable of measuring the polarisation of a monatomic sample. It is possible to understand something of this quantity however, by making the reasonable assumption that, at the densities found inside the HERMES storage cell, the chances of recombination in the gas volume is negligible, and the over-riding contribution to molecular recombination arises from surface effects. The quantity has been studied at higher temperatures than are experienced during normal running conditions, and the conclusion that $\beta\epsilon[0.45, 0.83]$ was reached [Kol98].

The upper limit is arrived at from measurements made at 260 K in 1997 and follows

the logic that, at this higher temperature the possibility of recombination is higher due to the increased kinetic energy of the atoms, so $\beta \leq 0.83$ which was the value at 260 K.

The lower limit is reached by the further supposition that the nuclear spin is not affected by the recombination process and that the nuclear polarisation of a molecule P_m can be reached as being the average of the nuclear polarisation of an atom on the surface of the cell P_s and the nuclear polarisation of an atom in the gas body P_a. Since an atom on the cell wall has undergone some depolarisation by its collision with the wall, apply the equation

$$\beta_{low}^{100K} = \frac{P_m^{100k,low}}{P_a^{100K}} = \frac{P_a^{100K} + P_s^{100K,low}}{2} \times \frac{1}{P_m^{100k}} \tag{3.9}$$

and apply a correction factor of 0.9 to account for the depolarisation of a molecule which comes into contact with the walls of the cell, giving the lower limit of $\beta = 0.45$. So this gives a final value of β as merely being the mean value of the two limits, with the range expressed as an uncertainty, i.e. $\beta = 0.63 \pm 0.19$.

The uncertainty in the value of β is a major contributor to the uncertainty of the overall target polarisation.

3.3 The HERMES Spectrometer

The HERMES spectrometer (fig. 3.7) is split into two halves (top and bottom) above and below the beam line. It consists of Drift Chambers (DVCs, FCs and BCs in figure 3.7), Proportional Chambers, Multi Wire Proportional Chambers (MCs in figure 3.7), a Ring Imaging Cerenkov (RICH) detector (not used for the work in this thesis), a Transition Radiation Detector (TRD), several Hodoscopes and a lead glass calorimeter. There is also a set of silicon detectors in the front region called the Lambda Wheels (LW) which were not used in the work presented in this thesis. A more thorough description of the apparatus can be found in [A+98].

The purpose of each detector that was used in the work in this thesis is explained in the rest of this chapter. Descriptions of the Ring Imaging Cerenkov detector and the Lambda Wheel detectors are not included, as they were not used in the analysis of data in chapter 5.

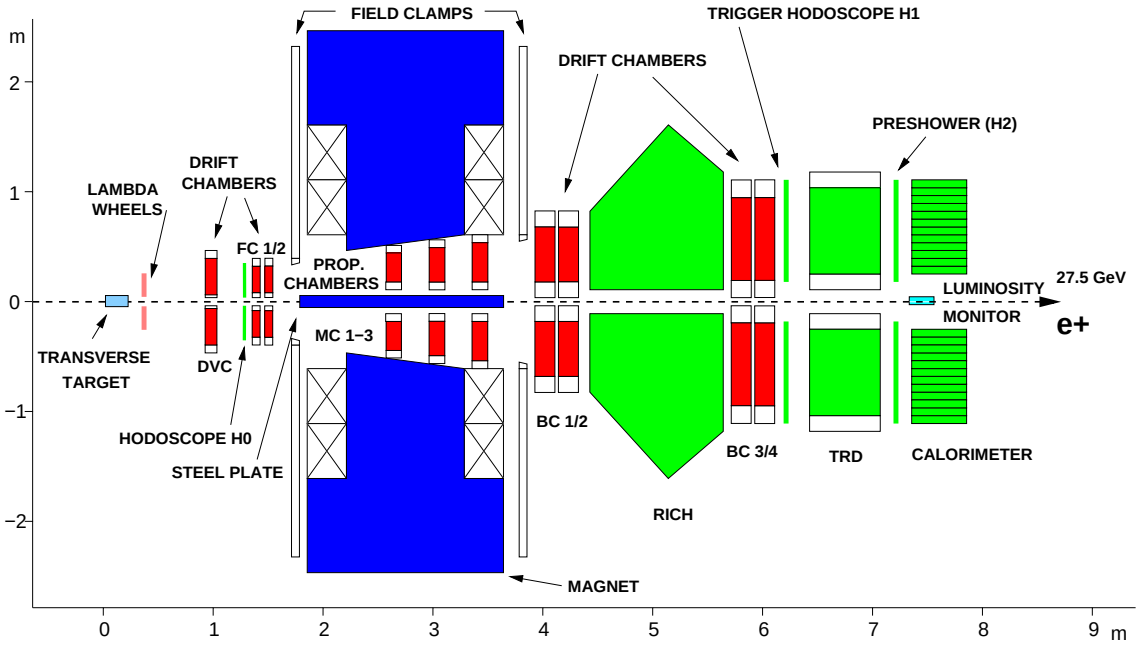

Figure 3.7: Diagram of the HERMES spectrometer showing all major detector components. The PID detector systems are shown in green, whereas the tracking detectors are shown in red. The large blue section is the main spectrometer magnet, used to bend charged tracks through the spectrometer to aid in PID and momentum reconstruction.

3.4 PID at HERMES

PID at HERMES is performed using a likelihood technique [Kai97] that discriminates between leptons and hadrons with hadron contamination of the lepton sample in the order of 1%. The method is founded upon empirical knowledge of the Transition Radiation Detector (TRD), a pre-shower hodoscope (H2) that sits in front of the calorimeter and the calorimeter itself. In other analyses, the RICH detector plays an essential role in hadron-lepton separation, however information from this detector is not used in this analysis.

The Pre-Shower Detector

The pre-shower detector [A$^+$98] consists of two parts, two radiation lengths of lead that convert incident leptons into electromagnetic showers and an array of 84 scintillator bars that sit 42 above and 42 below the beam line. The scintillator bar array is sometimes referred to as the H2 hodoscope.

The pre-shower detector is an important device for differentiating between leptons and hadrons – hadrons do not produce an electromagnetic shower when passing through the original layer of lead, and so do not usually produce an amount of light

in the hodoscope similar to that of leptons. There is a part of the light production distribution that overlaps, but in this area other techniques can be used to differentiate between the two particle types. The calorimeter also offers lepton/hadron separation (figure 3.8) based upon a similar concept, but with better resolution in the overlap area that proves difficult for the pre-shower detector.

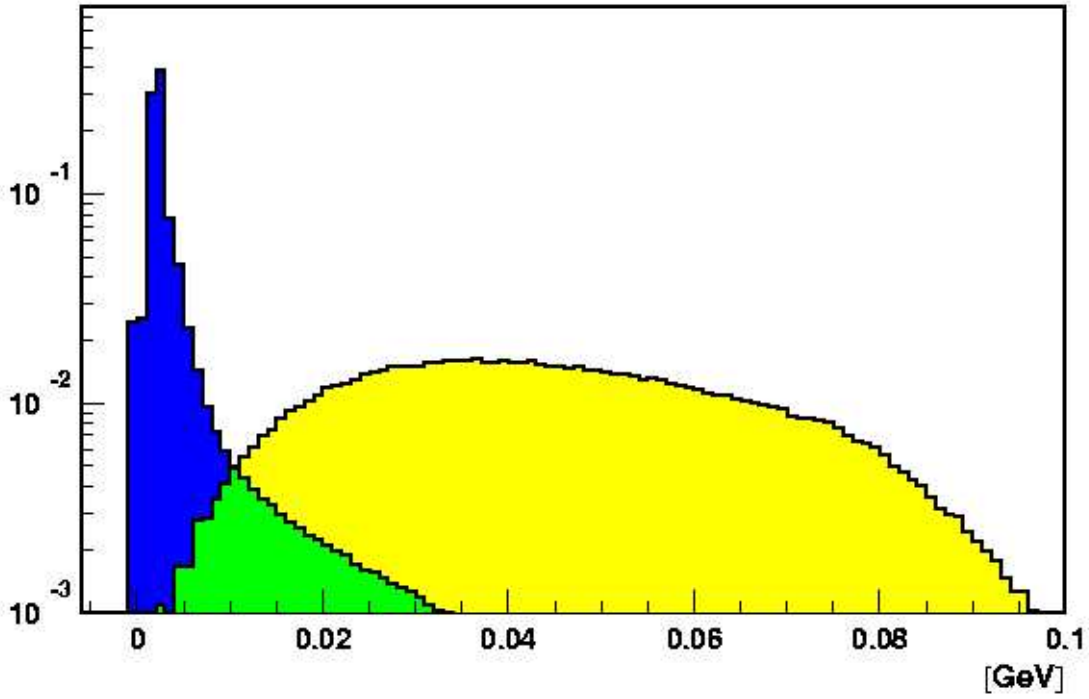

Figure 3.8: The distribution of energy deposited in the preshower detector. The yellow region is leptonic energy deposition, the blue shows hadronic energy deposition. Leptonic/hadronic separations in the overlap area can be determined by other means at HERMES. Picture is taken from [Kai97].

The Transition Radiation Detector

The Transition Radiation Detector [A+98] consists of six modules, each consisting of a radiator with plastic fibres, each of ≈ 20 μm and a gas filled (X_3/CH_4 in a ratio of 90/10) proportional chamber with vertical wires with a separation of 1.27 cm. Both electrons and hadrons deposit energy in the TRD, but since only electrons produce transition radiation in the HERMES energy regime the responses of all six modules can be combined and, using a probability-based analysis, a pion rejection factor better than 1400 for a lepton efficiency of about 90% can be obtained.

The Electro-Magnetic Calorimeter

The EM calorimeter [Ava98] is a very versatile piece of equipment that is used not only in PID and as part of the main DIS trigger at HERMES, but can also be used to measure the energy of photons for DVCS analyses, as well as for π^0 and η decays and other radiative processes. The poor energy resolution of the calorimeter, however, generally means that steps are taken not to rely upon this measurement in the analysis of DVCS events (see chapter 5 for more information). The calorimeter also provides a coarse position measurement for photons which would otherwise be untracked in their flight through the spectrometer.

It consists of 840 radiation-hard lead-glass blocks in which electromagnetic showers produce Ĉerenkov light, which in turn is detected by PMTs which view the glass blocks from downstream. Each block has an area of $\approx 9 \times 9$ cm^2, and is of length consistent with ≈18 radiation lengths. The blocks are arranged in two 42×10 arrays, one above and one below the beam line. See fig. 3.9.

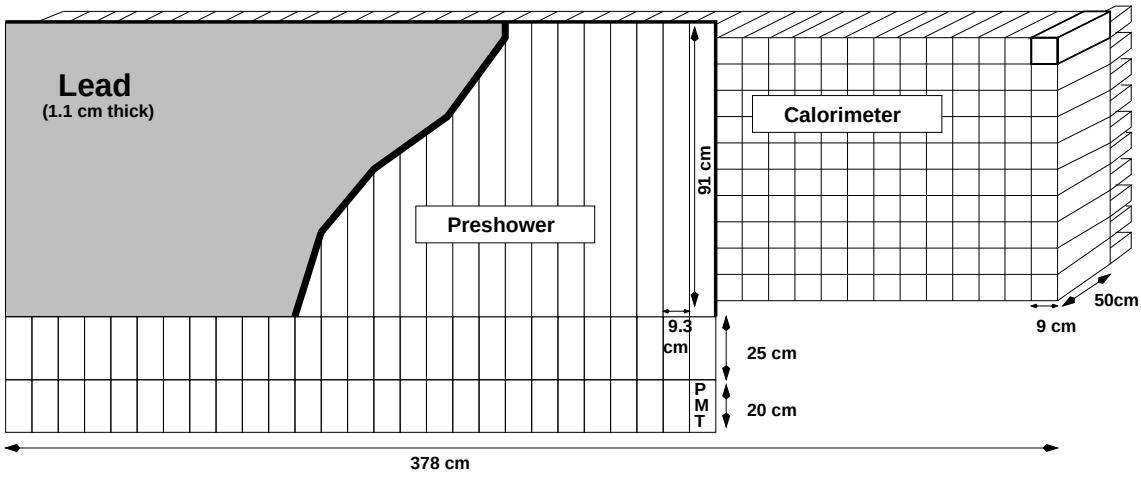

Figure 3.9: The pre-shower and calorimeter parts of the HERMES spectrometer. The pre-shower is preceded by two radiation lengths of lead to aid in shower production. The EM calorimeter is used as part of the trigger system, and is also used for PID and as the main source of information for uncharged particles such as photons.

The response of the calorimeter has been studied extensively [Ava98]. It has been shown to be able to resolve impact position to within 1 cm and is not susceptible to radiation damage.

3.5 Tracking at HERMES

In addition to being separated into two halves (top and bottom) around the beam line, the HERMES detector can be considered to be in three sections along the beam line, front, magnet and rear. These sections are divided with respect to the spectrometer magnet which is responsible for bending particle tracks in order to determine track momentum. Any track used in the DVCS analysis portion of this chapter must be registered by tracking detectors in both the front and the rear of the spectrometer. The detectors used for tracking in the DVCS analysis chapter of this thesis are all wire chambers which rely upon the principle of charge amplification in a gas and are split into two different categories—Multi-Wire Proportional Chambers (MWPCs) and Drift Chambers.

Multi-Wire Proportional Chambers

The structure of this type of detector is a three dimensional grid of anode (cathode) wires surrounded by a gas, all contained between cathode (anode) plates. Charged particles traverse the detector and in the process ionise the gaseous medium. The electric field inside the detector then accelerates the electron (positron) towards the anode (cathode) wires. In the process of this acceleration, the electron (positron) causes more ionisation and a cascade effect takes place, known as the Townsend Avalanche. This cascade effect scales proportionally to the number of primary interactions, and so can be used as a measurement of the original particle. The signal from the avalanche is detected at the anode (cathode) wires and read out. The TRD and MCs are examples within HERMES of this type of design.

Drift Chambers

The Drift Chambers are based on a similar design principle to the MWPCs, but the electric field within them is smaller, meaning that the Townsend avalanche never takes place. The drift time of the particle is instead used to calculate the intersection of the detector and track. The back and front chambers (BCs and FCs) are examples of this type of detector design.

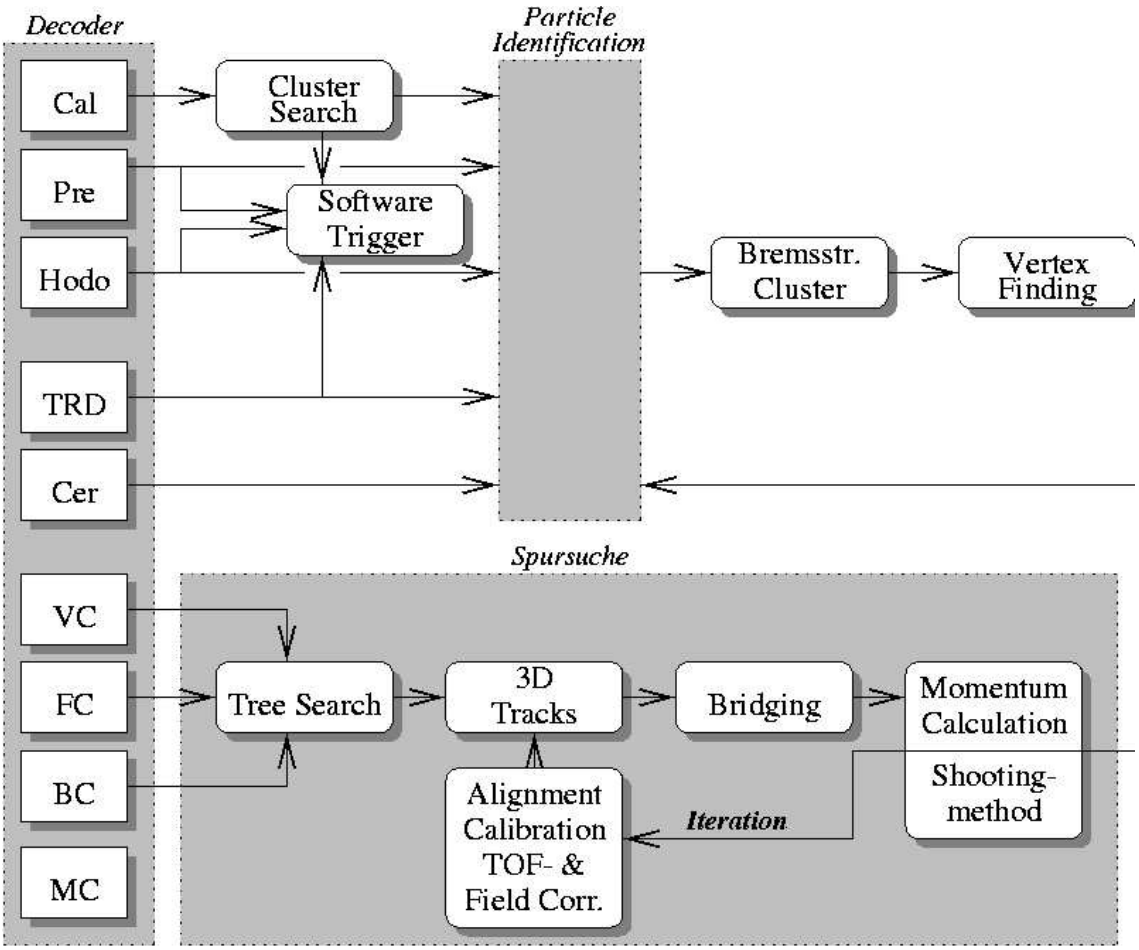

Figure 3.10: HRC software flow diagram from [Wan97]. In order to isolate a track through the spectrometer, several iterations of the tracking system are often needed, where information is combined from the various tracking detectors and the PID system to find the most likely candidate. Several tracking methods have been used in HERMES in order to connect tracks through the front and rear of the spectrometer, bridging the gap at the main magnet. All the data considered in this thesis uses only the long track method, where a positive match is made between tracks in the front and rear parts, although it is possible to set the reconstruction code to match tracks that have only a moderate probability of being part of a single track. This method is known as the "forced-bridging" technique.

3.5.1 HERMES Reconstruction Code

Tracks in the detector are reconstructed by the Hermes Reconstruction Code (HRC) [Wan97]. This is a special software package that uses the Treesearch algorithm that looks for space points in the tracking detectors and recursively searches for preset child patterns stored in a database both fore and aft of the spectrometer magnet until a unique track is established that can be 'bridged' over the gap for the magnet. The "shooting technique" referred to in figure 3.10 refers to the method of momentum determination by varying ascribed momentum to each partial front track in order to

match it with a rear track, although this technique is normally eschewed in favour of a refined look-up table technique. The track information is then combined with PID data from the individual PID detectors in order to achieve a final result that includes position, momentum and particle-type information.

HRC was designed early in the lifetime of the HERMES experiment, and has been expanded as extra detectors have been added, although the principals remain the same. The bolt-on code that has been applied to the software package over the lifetime of the experiment is referred to as eXtra Tracking Code, or XTC.

Photons—the Calorimeter

The above method does not work for uncharged particles, the paths of which are not bent by the spectrometer magnet. In this case, particles such as photons are only detected by the calorimeter, and all the information on the particle must come from this source. This causes the energy resolution of data on untracked particles to be poorer than that of tracked particles, and consequently in the analysis performed in chapter 5 a missing mass assumption is made so that a minimal amount of information about the photon from the calorimeter is used.

Further Processing

The final track information is stored in an ADAMO database [PTG93], with the information on each track broken down into tabular form, containing information on not only the track itself, but "slow control" information that relates to the status of the various detectors and beam conditions at the time of the track, and other such data quality information. These are then available to the interested analyser, either via the C API or through a database browsing package, Distributed Adamo Database (DAD), which is written in the Tcl/TK GUI scripting language.

Chapter 4

The Recoil Detector

The Recoil Detector was the last upgrade to the HERMES spectrometer before it shut down in 2007 [ea97]. Having anticipated the increased interest in GPDs and DVCS, the HERMES collaboration took steps to include an extra instrument in their detector setup that would be specifically designed to measure DVCS events, and allow exclusive measurements to be made. The spectrometer was designed in such a way that it was able to detect the real photon and scattered lepton from the DVCS events that happened in the target region, but not the recoiling proton, and it is for this particle that the detector is named.

The recoil detector was installed in the winter of 2005. This chapter will describe the detector as a whole and go into the detail of how the silicon strip subdetector system works. The detector was not in a suitable state such that data from the detector could be included in this thesis at all. It should be noted that the data analysis presented in chapter 5 took place with a transversely polarised target, which was removed for the installation of the recoil detector.

4.1 The Components of the Detector

The recoil detector was designed to sit in the target region of the spectrometer (figure 4.1) and provide tracking and momentum information on the proton that is involved in a DVCS event [ea97]. It extended the measurement range of HERMES into a lower t-region, and provided detection of the products of background processes.

To these ends, it comprised of a silicon strip subdetector system, the design of which was based on the Lambda Wheel detectors that had already been integrated

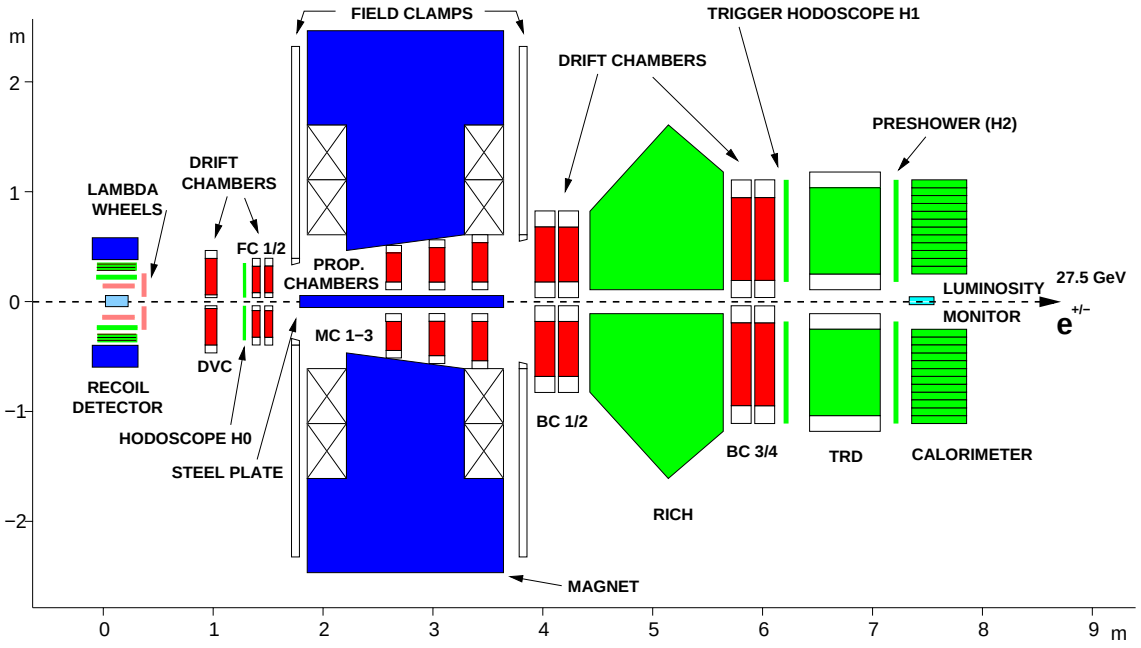

Figure 4.1: The HERMES detector showing the position of the recoil detector. The recoil detector takes the place previously occupied by the HERMES polarised target, c.f. figure 3.7. As in figure 3.7, PID detectors are shown in green, while tracking detectors are shown in red.

into the spectrometer two years previously; a scintillating fibre detector which was developed in the University of Giessen and a photon detector which sits outside the two previously mentioned detectors and provides information that aids background suppression and event selection. There was also a 1 T magnet which surrounds the detector and deflects charged tracks to aid in PID — see figure 4.2.

The silicon strip subdetector (figure 4.3) consisted of 16 TIGRE silicon strip sensors using both n- and p-doped silicon as detector material. Each silicon sensor was made of two oppositely-doped sides, n-side strips parallel to the beam, the p-side strips orthogonal to the n-side strips in their plane. The detector was designed to determine the momentum of the protons which interact with the beam leptons in a DVCS event. It also provided primitive tracking information which aided in the reconstruction of proton tracks which fail to impact on more than one of the scintillating fibre detector's fibres. It sat inside the beam pipe, so that the only material between it and the interaction was the 75 μm-thick aluminium wall of the target cell.

The scintillating fibre detector (figure 4.4) sat just outside the beam pipe [Hoe06]. It was the "workhorse" of the recoil detector, with the largest momentum range detection, and the most precise tracking information of any of the detectors – although most of the events it was built to detect fell within the acceptance of the

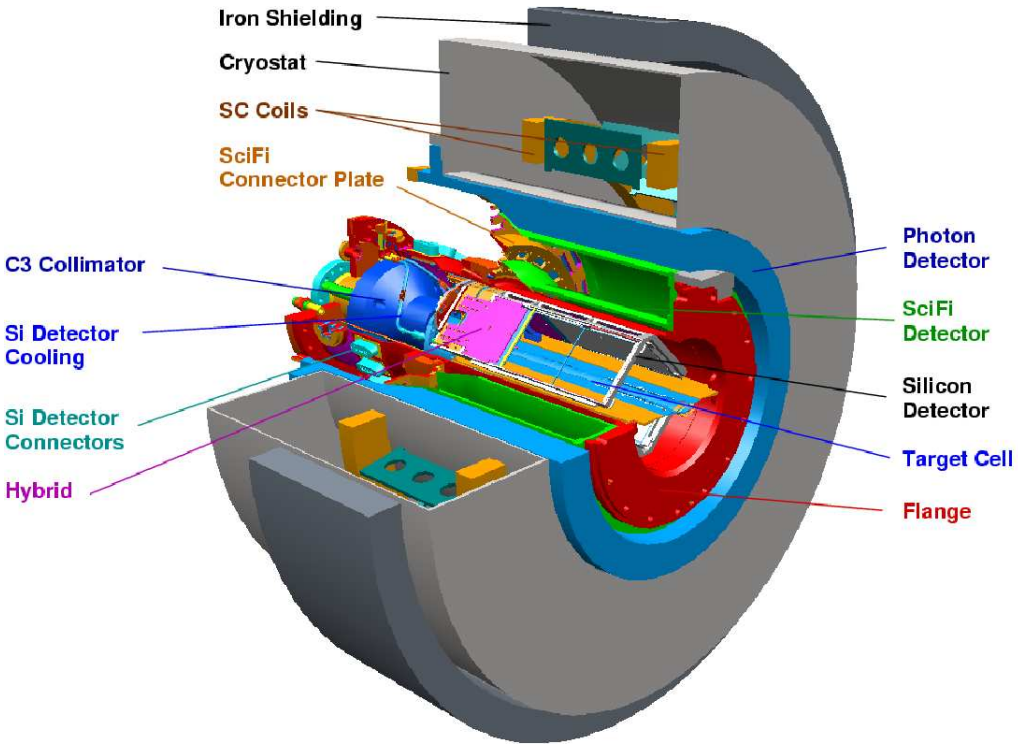

Figure 4.2: A 3D representation of the recoil detector. The silicon sensors sit in the centre of the detector, within the beam pipe. Surrounding the beam pipe is the Scintillating Fibre detector, surrounded in turn by the photon detector. The entire sensing apparatus sits in the bore of a 1T superconducting dual Helmholtz coil. The storage cell used in the polarised target has been replaced by a new cell, described in section 4.2.

silicon detector. It consisted of over 7000 scintillating fibres arranged in eight layers (2 "barrels" of 4 layers each) around the beam pipe, two layers parallel to the beam, and two offset by 10^o, referred to as the "stereo layers". Each barrel consisted of two parallel and two stereo layer. The barrels were arranged with as much distance between them as possible given the constraints imposed by other detectors. This was necessary if the detector was to be suitably precise with its tracking information. The detector's design was constrained by tight space issues — it was sandwiched between the beam pipe and the photon detector and could not be accessed from up or downstream. Instead it is built in a self-supporting structure which was mechanically clipped onto the rest of the spectrometer setup. It had no external structure in order to minimise the amount of material between the sensory fibres of the detector and the particles it was built to detect.

The two detectors, silicon and scintillating fibre, are the parts of the detector which are central to the detection of DVCS events. They form the basis of the detection system for DVCS events and provide the information that is used for momentum reconstruction. The outer photon detector is designed primarily to detect photons

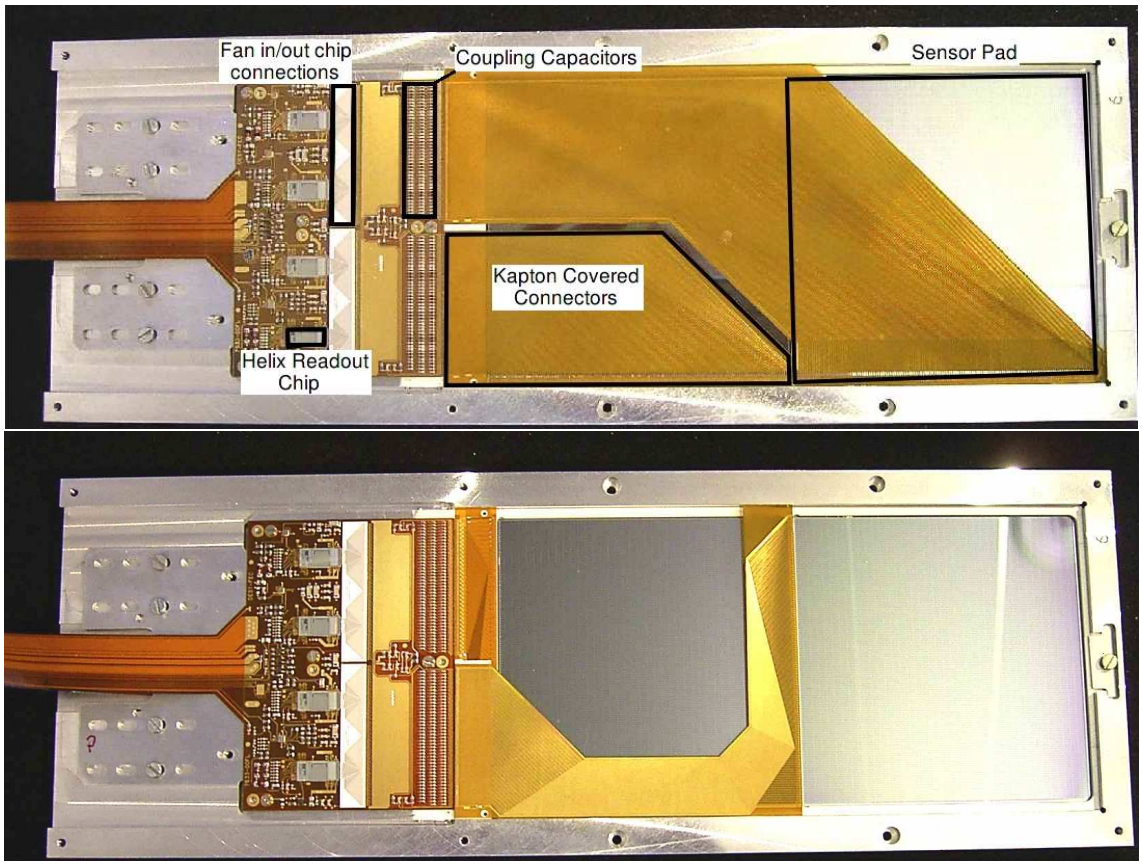

Figure 4.3: Photographs of a silicon detector module, n-side shown in the top picture, p-side shown in the bottom picture. The n-side picture has labels showing the most important parts of the silicon detector, highlighting one of the 4 readout chips on each side, and the connections between the chip and the sensor. The kapton foils that surround the connections are also labelled.

from Δ^+ decays. The decay channels, $\Delta^+ \rightarrow p\pi^0$ and $\Delta^+ \rightarrow n\pi^+$ both involve nucleons which could be mistaken for products of a DVCS event. Therefore, the recoil detector must, as a requirement, be able to distinguish between a Δ^+ decay (known as "associated DVCS", or "associated production") and a DVCS event and so the photon detector can detect the photons from a $\pi^0 \rightarrow \gamma\gamma$ decay. Tracks from π^+ particles from Δ^+ decays can be detected and identified by the scintillating fibre detector. See figure 4.5

The photon detector consists of three layers of tungsten which acts as a radiator for three layers of plastic scintillator, the six layers arranged in a segmented shower design with he first layer of tungsten two radiation-length thicknesses, the others a thickness corresponding to one radiation length. The scintillating material is segmented in a manner that allows the reconstruction of a decayed π^0, should two photons be detected. The innermost layer consists of 60 scintillator strips 30 cm×2 cm×1 cm arranged parallel to the beam axis. The other two layers

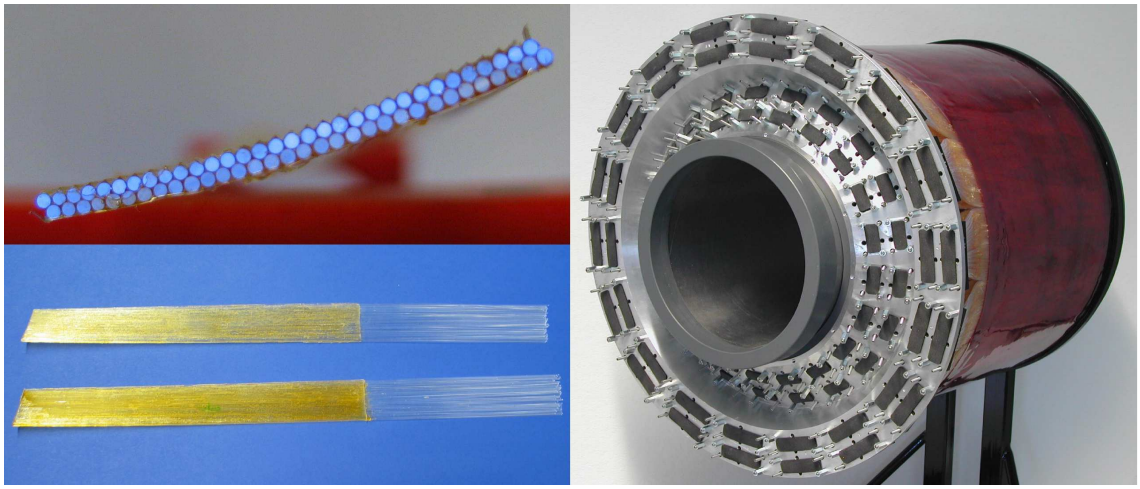

Figure 4.4: The scintillating fibre detector modules. The leftmost photographs show a partly assembled module with its close-packed cross section (top) which is laid flat (bottom) prior to being wrapped around the supporting barrel of the detector. The right most photograph shows the assembled detector prior to being incorporated into the recoil detector.

have a rotational offset of 45^o with respect to the beam axis and consist of 44 strips of scintillator material each. The photon detector is shown in figure 4.6.

The recoil detector is surrounded by a superconducting magnet, the presence of which is designed to bend the tracks of charged particles so that they can be identified by the scintillating fibre detector. It is comprised of two Helmholtz coils immersed in a bath of liquid Helium. It provides a field of 1 T in the bore and the field outside the bore is attenuated by an iron yoke that surrounds the magnet. This is absolutely necessary as the vacuum pump system for the rest of the spectrometer, and several other detector subsystems of the spectrometer lie within 5 m of the magnet, all of which could be rendered inoperable by a magnetic field of significant size and strength. The recoil magnet was designed with the intention that its field drop to no more than 200 Gauss (0.02 T) within 2 m of the bore.

4.2 The Storage Cell

In order to detect exclusive events with the intention of performing analyses of BSA and BCA observables, the standard HERMES polarised target was replaced with a unpolarised storage cell which was filled only with Hydrogen gas at higher densities than have previously been used at HERMES. A photograph of the target cell can be seen in figure 4.7.

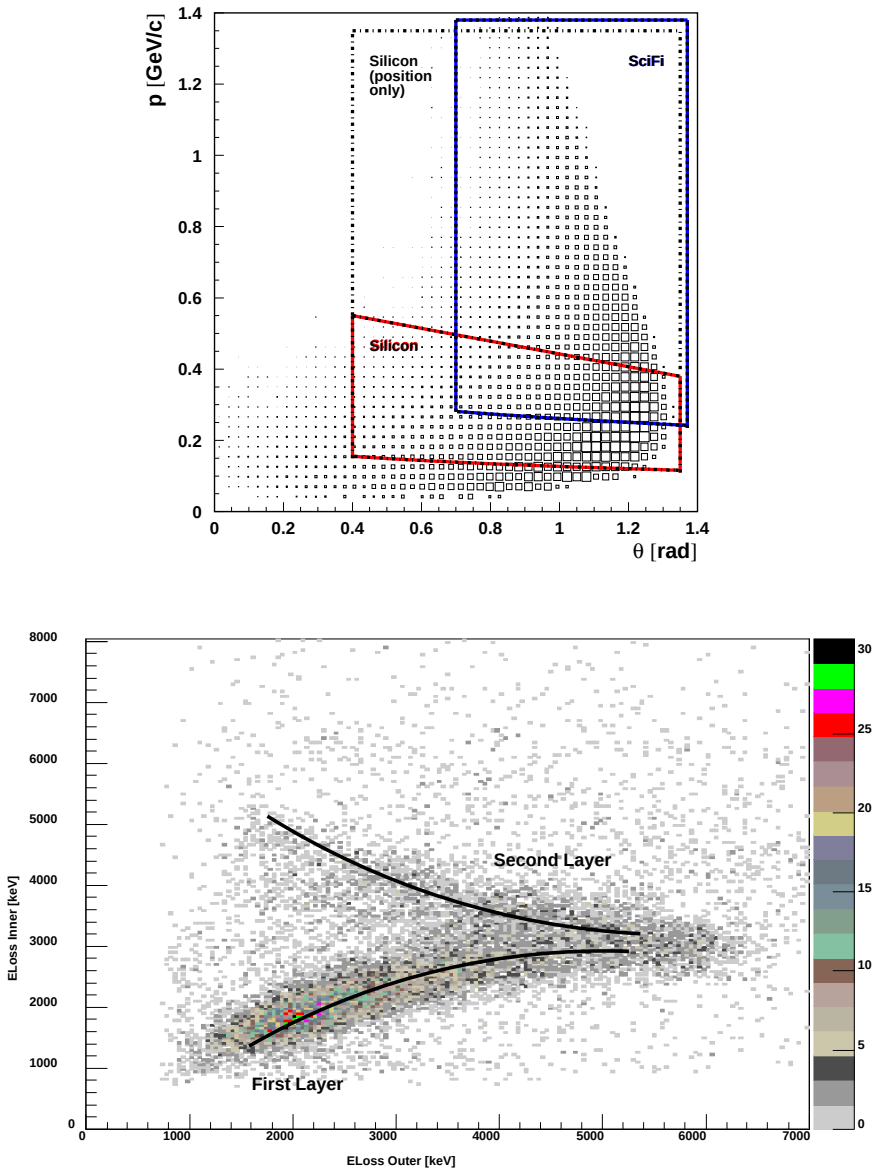

Figure 4.5: Two plots: one (top) shows the different momentum ranges of the particles detected by different subdetectors; one (bottom) shows the amount of energy deposited in the silicon detector as a function of the original momentum of the proton detected. Starting with a minimal momentum (just enough to exit the target cell), the proton deposits a small amount of energy in the first layer of the silicon detector before it is stopped. As the momentum of a detected particle increases, so does the amount of energy deposited in the first layer of the detector, until it has sufficient momentum to punch through the first layer into the second layer. At this point, the energy deposited in the first layer starts to drop, as the proton passes through that layer easily. The cycle repeats with the second layer. Once a proton has sufficient momentum, it passes easily through the second layer, depositing only a small amount of energy in the detector. These protons exit the beam pipe and are detected in the scintillating fibre detector.

Figure 4.6: Photographs of the Photon Detector (left) and the magnet (right). The photon detector fits flush inside the bore of the magnet in the final assembly.

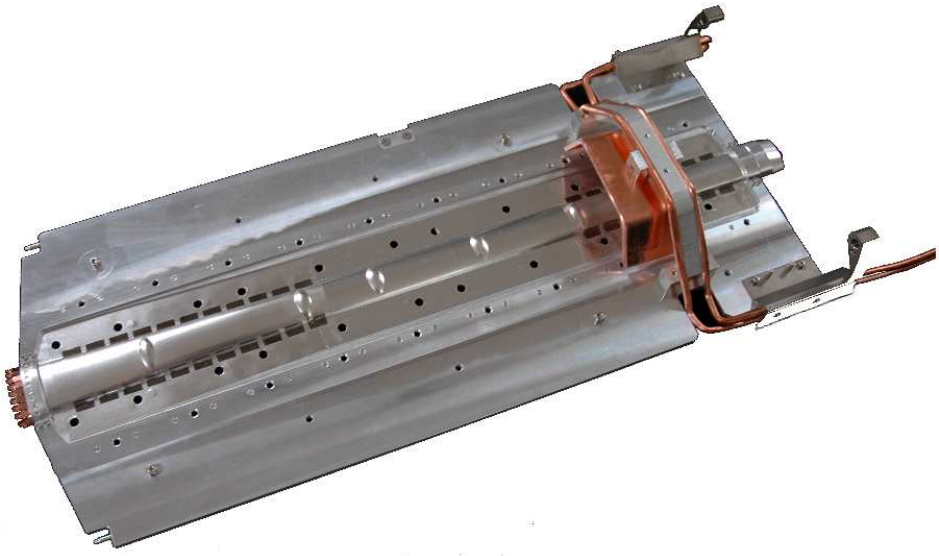

Figure 4.7: The revised target cell, made of 75 μ-thick aluminium which will hold unpolarised Hydrogen gas as a target for the rest of the experimental running time. The copper pipes on the picture form part of the cooling system that supplies the copper heat sink. The copper connections at the left end of the cell ensure that the cell forms a proper electrical contact with the beam pipe.

4.3 The Silicon Detector

The silicon detector is the most complex detector in the recoil setup. The active detection parts of the detector are TIGRE sensors from Micron Semiconductor [Kra05]. Each silicon sensor side has 128 strips which each has two different readout modes, high and low gain. These two readout modes are achieved by capacitive splitting which allows the silicon detector to amplify low-strength signals from very fast and very slow particles which either pass through the detector with little interaction, or have barely enough energy to escape the target cell, and cause only a small signal in the detector [ea97]. This means that the momentum range of the silicon detector is maximised, allowing the detection of Minimally Ionising Particles (MIPs) (kinetic energy of ≈ 300 MeV) through to slow protons (kinetic energy of ≈ 10 MeV) which are completely stopped by the detector. This means that the silicon detector has a dynamic range of 70+ MIPs which is unusual in this class of detector. One consequence of maximising the momentum range is that the detector requires a custom-built readout electronic set, as the data rates from readout are very high — especially in the HERMES environment where trigger rates can reach 1 kHz. The detector was calibrated in two test beams, one at Erlangen University and the other at the T22 test facility at DESY.

4.3.1 The Silicon Sensors

The silicon sensor pads are 128-strip double-sided TIGRE sensors, developed at Micron Semiconductor and are similar to those used previously at HERMES in a silicon test detector. Their design was originally developed for a space mission but has been modified according to the needs of the recoil detector setup. Each strip has coupled capacitors attached to it in order to maximise the momentum readout range. The value of 15pF was chosen after extensive tests at DESY in Zeuthen using a laser as an energy source.

Readout is controlled by the on-board readout chip, the Helix-128 3.0. A version of this chip was also developed for use elsewhere in DESY at the H1 experiment. It has 128 channels and is readout on a FIFO basis, meaning that one chip is needed for every side of silicon. It is triggered to readout through the Helix Control Units (HLCUs) which were developed in tandem with the Hermes Analogue-to-Digital Converters (HADCs) at Nikhef Institute. The Helix chips are mounted on the hybrid part of the module. The hybrids also have radiation monitors and thermometers mounted on them, for the purpose of monitoring conditions inside the beampipe.

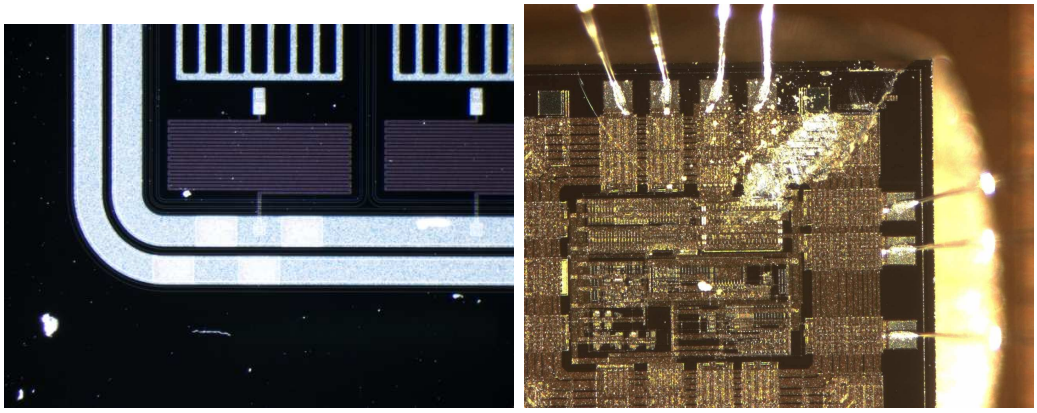

Figure 4.8: Microscope photograph of the detailed structure of the silicon detector. The vertical strips in the photo are the silicon strips and are attached to the silicon frame through the coupling capacitor seen as the small rectangle. The thicker rectangle is the silicon frame in which the detector strips are held. The photograph is taken at a wavelength chosen to render the kapton covering invisible. The second photograph is a Helix readout chip, seen at high resolution.

High magnification pictures of silicon detector parts can be seen in figure 4.8.

4.3.2 The Readout Electronics

The Silicon Detector utilises custom-designed electronics. These are necessary due to the high trigger rate at HERMES. The three readout units are Analogue Clock Control (ACC) units, Helix Control Units (HLCUs) and Hermes Analogue-to-Digital Converters (HADCs) (c.f. figure 4.9). The ACCs provide an interface between the Helix chips on the silicon modules and the HLCUs and HADCs—it is from the ACCs that radiation and temperature information from the modules enters the HERMES slow control chain. The ACCs also feature line driver chips to push the signals from the Helix chips through to the HADCs which are more than 35m from the experiment, housed in the HERMES electronic trailer. The HLCUs, as the name implies, control the Helix chips which then provide a trigger to the HADCs calling for readout. The HLCUs in addition act as an interface to program the Helix chips with various internal settings. The HADCs are the most complicated of the readout electronics, featuring four ADCs per HADC module, each reading out two of the Helix chips on the onboard electronics. This means that one HADC can readout two silicon modules, resulting in four HADCs needed to read out the entire detector.

Each ADC on an HADCs has 1024 channels, and is preceded in the readout chain by a set of DC-coupling circuits, which clean the signal in preparation for measurement. Each HADC is capable of subtracting pedestal signals pre-loaded into the module

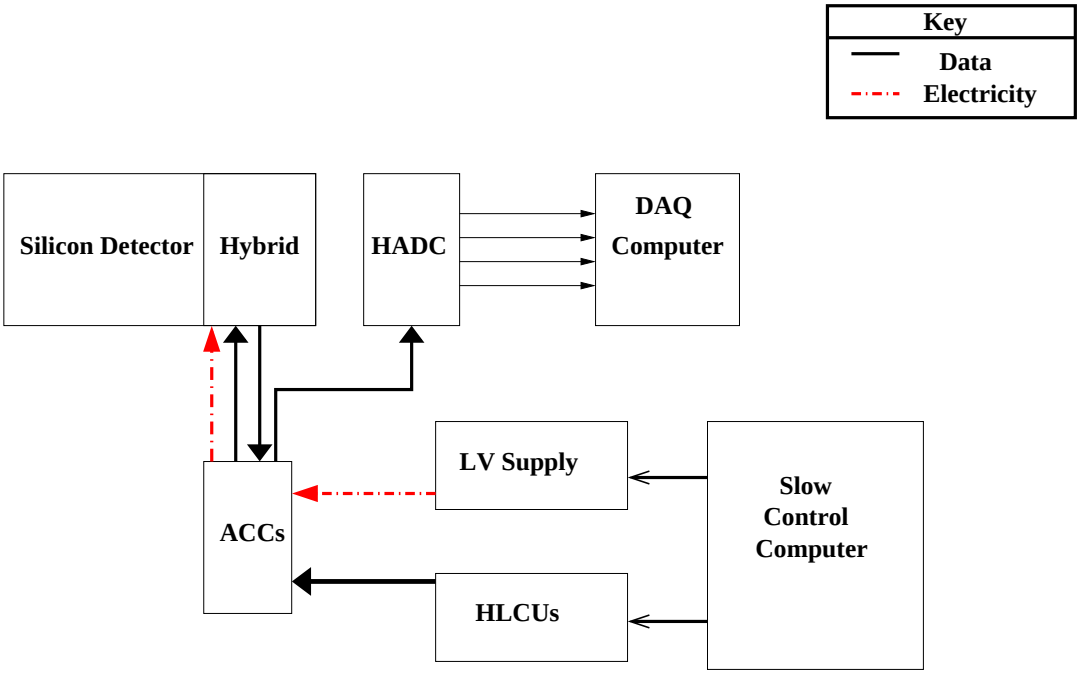

Figure 4.9: A schematic diagram of the silicon detector showing the layout system of the electronics modules that are used to control the information flow. HADCs and HLCUs are powered by a custom-built Low Voltage power supply

(i.e. the base offset read by the module when there is no data to be readout) for which there are dedicated runs every three hours by HERMES. It is also capable of masking readout of channels which have no information to impart ("Zero-Suppression") and performing Common Mode Noise Correction (CMN). This CMN is calculated by taking the reading from a random 16 of the first 32 channels of each Helix chip and comparing the levels found in strips that do not show a signal above pedestal. The order of these calculations can be seen in figure 4.10.

The HADCs were the subject of considerable effort in the Nuclear Physics Group in Glasgow University, which was responsible for their manufacture and testing. Although the modules were based on those used in the Lambda Wheel detectors at HERMES, they were extensively modified by Glasgow technicians with the help of the original designers at Nikhef, replacing some capacitors and resistors in the circuit board to improve the original design. This means that although the name is the same as the Lambda Wheel ADCs, the two modules are incompatible, and software to read out the HADCs used in the recoil project had to be developed separately in Glasgow and Erlangen university. A third system exists, built by students from Zeuthen and Gent institutes, but this was used only for testing and calibration. The Erlangen software is production software, used in the day-to-day running of the modules, whereas the Glaswegian software is a more comprehensive package that

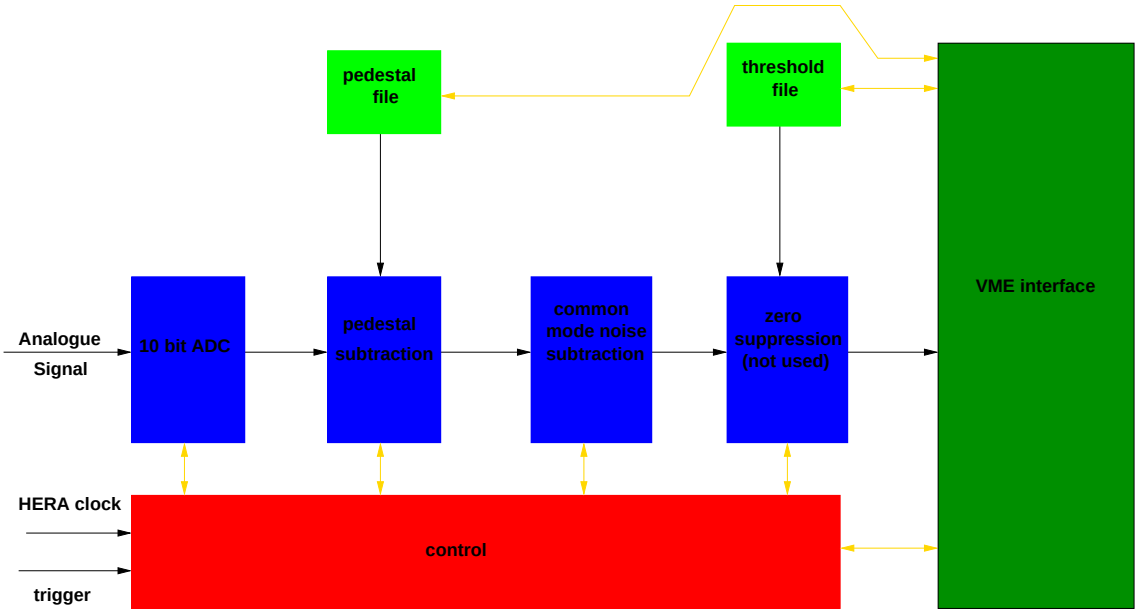

Figure 4.10: A schematic diagram of the electronics process of the HADC showing the data processing flow inside the HADC.

allows for testing loops to be implemented, memory checks to be run and feature testing. This software, which the author developed, took approximately one month to design and test, and will be extended in the future for work on other projects.

4.4 Calibration and Testing of the Recoil Detector

In order to be able to understand data from the silicon detector, it was necessary to perform several calibrations in DESY-Zeuthen, GSI-Darmstadt, DESY-Hamburg and Erlangen University. The Zeuthen tests were tests with a laser as a data source and formed the basis of many design decisions of the silicon detector [GHK+04b], but were performed prior to the author joining the collaboration. This section refers only to the tests and calibrations that have been performed since the author has been involved in the project. The author was involved for the most part with the T22 tests and they are discussed here at length. The author was also involved with the running and data taking with the cosmics test, but was not responsible for the analysis of that data, so it is not discussed to any particular depth.

4.4.1 The GSI Tests

The GSI laboratory in Darmstadt is currently undergoing a transformation into a international laboratory capable of sustaining the FAIR accelerator facility, but in November 2003 it was a national facility that sublet beamtime in one of four caves available to researchers. Measurements were made with a proton-pion beam with kinetic energies of 300 MeV, 450 MeV, 600 MeV and 900 MeV available according to user-specification. It was at this testbeam facility that the constituent parts for the recoil detector were assembled for the first time. The time spent here was used to verify that each detector could be read out in a beam for the first time. Key results from this test beam include investigation of the angular dependence of energy deposition in the silicon detector (see figure 4.11) and the measurement of efficiencies, single-fibre response functions and MIP detection capability of the Scintillating Fibre detector [HHK+05] (see figure 4.12).

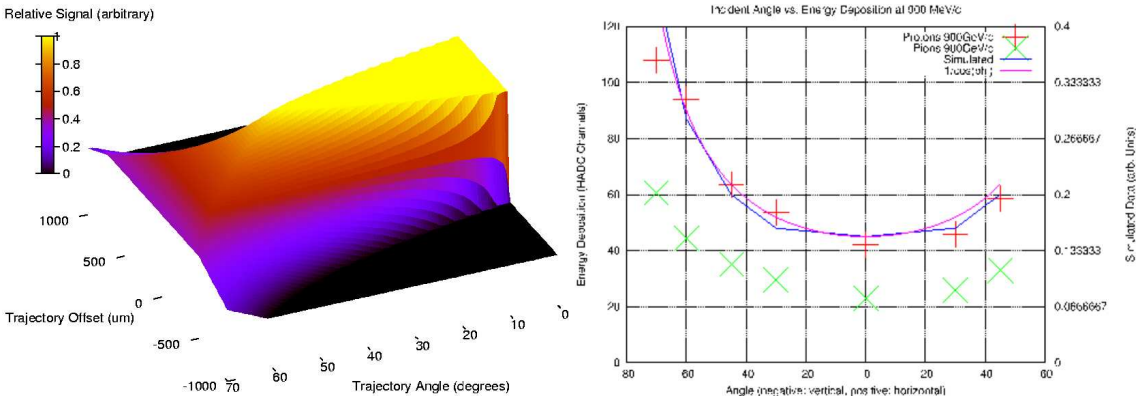

Figure 4.11: The left plot shows the expected relative energy deposition of a proton in silicon strip as a function of angle and impact offset from the centre of the strip. The right plot shows the angular dependence extracted from the GSI data for protons and pions, as compared to simulations and and a naive $\frac{1}{\cos\theta}$ model.

The Erlangen Calibrations

Tests at Erlangen University in southern Germany [Gro05] were designed to calibrate both readout modes of the silicon detector. A Tandem-style accelerator provided a beam of protons with which the response of the detector was tested. In order to access both readout channels of the detector, each module was tested with protons which had 4 and 9 MeV kinetic energy. An additional measurement was made at 6 MeV in order to allow studies of systematic errors. The silicon detector was kept in a vacuum chamber for the duration of the tests with cooling provided by a

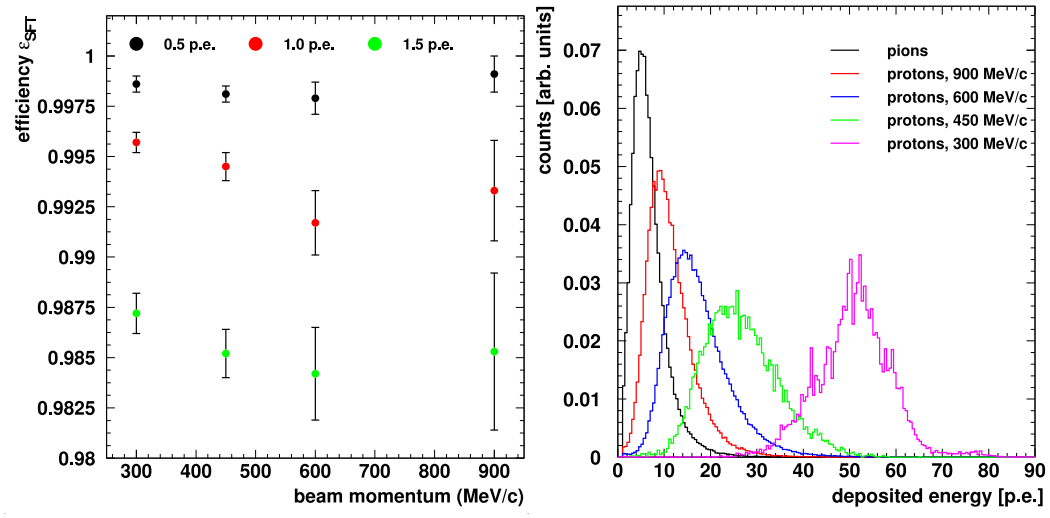

Figure 4.12: Data from the Scintillating Fibre detector test at GSI. The left plot shows the efficiency of the SF detector at detecting pions — an essential quantity as pions are minimally ionising in the SF detector, so this plot shows the poorest efficiencies of the detector. Efficiencies are dependent upon detection thresholds measured in photo-electron peaks, and in the final experiment a threshold of 1.0 photo-electron peaks was chosen as an acceptable balance between decreasing efficiency and increasing noise. The right plot shows the energy deposition of the various particle beams and energies in the module of the SF detector tested at GSI. These quantities (known as single fibre response functions) are essential for a calibration of the SF detector and will form the basis of the SF detector-enabled PID system used in the final experiment.

water-cooled copper heatsink. Triggering of the readout was provided by a 100 μm-thick scintillator piece that was placed before the silicon detector in the test setup for use with 4 and 6 MeV protons (since these protons were fully stopped in the detector) and after the the detector in the case of the 9 MeV measurements, since at energies around and above 6 MeV the proton has enough energy to punch through the detector. Due to energy loss in the trigger scintillator, the amount of energy deposited in the silicon sensor for calibration at a proton energy of 4 MeV resulted in protons of $\sim$2 MeV actually reaching the sensor, becoming fully stopped before entirely traversing the 300 μm-thick sensor width. At this level of deposited energy the low gain readout channel responded to the proton signal, but without the high gain readout channel reaching saturation. At 9 MeV, the proton has enough energy to punch through the silicon detector cleanly, providing an easily calculable deposit in the silicon detector and since the proton does not need to traverse a scintillator piece the spread in proton energies at the silicon detector is small, allowing for a well-defined beam energy resolution. This means that the 4 MeV data can be used to compare and contrast the response of the high and low gain readout channels, whereas the 9 MeV data can be used to provide the detector with a single-strip calibration. The entire data set has been used to study the crosstalk effect in the

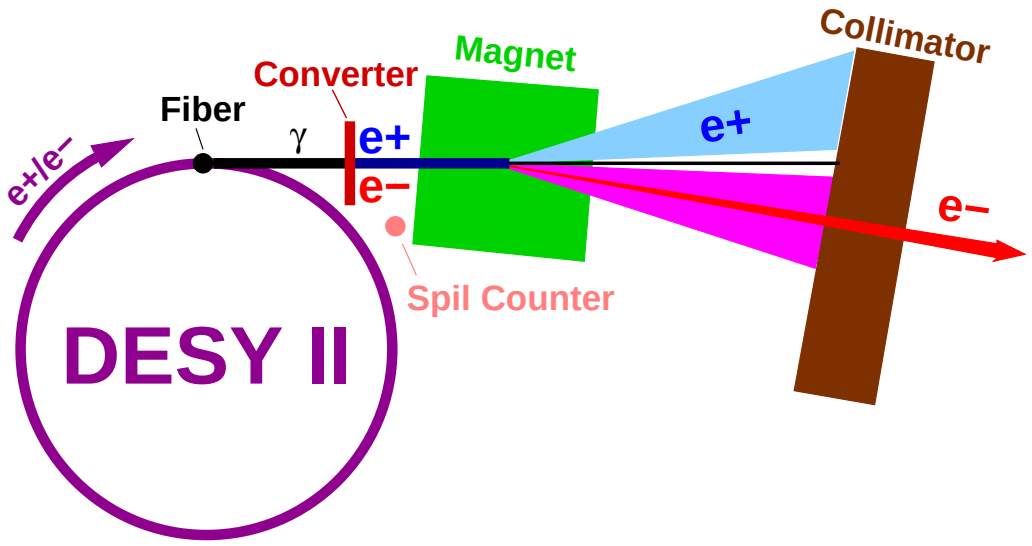

Figure 4.13: The DESY II test facilities available at the DESY institute in Hamburg. The beam is produced by the DESY II accelerator and split between three halls. Each hall is provided with a bunched electron beam with a density of 1000 particles/cm^2 with a user-defined energy of between 1-6 GeV with a spread of $\tilde{5}$%. The user can then choose which beam energy to receive in the test area by changing the power of the bending magnet that is used to steer the beam into the test area.

silicon sensor, where the impact of a particle on one strip has the effect of creating a signal in another strip.

The T22 Tests

The T22 test facility at DESY was used repeatedly in the design and development of the recoil detector. At the start of the project, the beam was used to provide information on the viability of the capacitive splitting technique on the silicon detector that allows the detector to have such a wide range, yet still achieve a good resolution at low energy deposit levels [GHK$^+$04a]. Towards the final stages of the project the facility was used by the Scintillating Fibre development group to provide alignment information on the individual fibres of the detector, essential for determination of a high quality angular resolution. Whilst the author was involved in the latter, more details are provided in reference [Hoe06] and that procedure will not be discussed here. Instead, this section will remain concerned with the 1-MIP calibration test that was run in July and August 2004 at the T22 facility, including a small discussion of the facilities on offer and some sample results [HM05].

The T22 facility (see fig. 4.13) provides a user-controlled beam of e^-. The possible energy range is 1-6 GeV, with a 5% spread in the chosen value. This range is consistent with the area on the Bethe-Bloch curve that represents a MIP in 300 μm

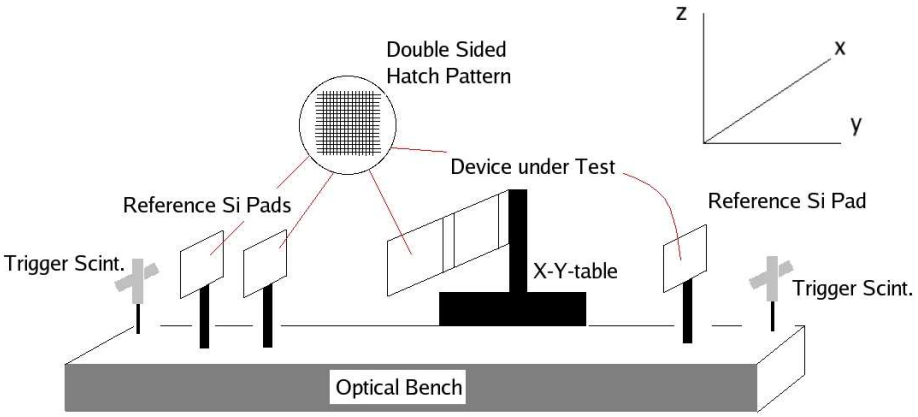

Figure 4.14: The "silicon telescope" used in the calibrations. The beam direction is the y-direction in the figure. Triggering comes from the scintillators placed fore and aft of the telescope. The reference silicon sensors are also double-sided TIGRE sensors made by the same manufacturer for use in the Zeus Micro Vertex Detector. Readout of these is performed by standard CAEN ADCs which are sufficient in this case due to the low trigger rate compared to the trigger rate expected when the Recoil Detector is read-out as a part of the HERMES experiment. Readout of the RD silicon detector is performed by an HADC.

thick silicon strip. The beam is bunched, with a density of 1000 particles/cm^2 . The beam seen at T22 is produced by lepton-production of photons from a carbon fibre target, with the initial leptons being taken from the DESY II pre-injector that services HERA. The produced photons are converted into $e^{\pm}$ pairs by a number of various targets that can be changed according to user demands, and these different converter types and thicknesses control the rates seen in the test beam area. The resultant spread from the γ-converter is then formed into a beam through the use of a lead collimator. The measurements discussed in this section were made at 6 GeV. A reference system that was developed for the ZEUS Micro Vertex silicon detector system (see figure 4.14) was used to track particles through the silicon detector, and provide a trigger for the detector. This reference system—referred to as a "silicon telescope"—was also used to compare noise in the silicon detector with a similar system, and to ensure that performace targets were reached.

The silicon piece under test was mounted on a movable table and scanned in a diagonal pattern to ensure that every strip was read out. Several technical obstacles had

to be overcome during this testing phase, which are more thoroughly documented in report [HM05] but will be discussed briefly here.

The object of the T22 procedures was two-fold, firstly to establish noise and pedestal characterstics of the silicon module and secondly to explore the possibilities of calibrating the silicon modules, in particular the response of the detector to MIPs, as before the tests there was some uncertainty as to the ability of the detector to resolve such low energy deposits, with some possibility that these small signals may be drowned by the pedestal signal.

Physical Alignment and Pedestal Correction

The first technical obstacle to overcome was to make certain that results would always provide data for all strips of the detector. To this end, several alignment runs were performed for each sensor, with positional readout showing the position of the 1 cm×1 cm beam on the silicon detector. These can be seen in figure 4.15. After this was corrected, 1000 pedestal runs were taken for the sensor with no beam. It was found that after every 100 runs there was a distinct shift in the average value of a pedestal. This shift is attributed to the effect or reprogramming the Helix readout chips, which also took place every 100 runs. There have been several reports that reprogramming the Helix Chips can result in the values read out by the Helix changing. In order to correct for this, the mean value every 100 runs was found over the 1000 run set and each block of 100 runs normalised to this average value. The result can be seen in figure 4.16.

Results

After alignment and pedestal correction, we have a set of pedestal values—one for each strip—that can be subtracted from the measured data during runtime in order to leave just the signal data. This signal data is then fitted with a Landau-Gauss convolution function, Landau for the data and Gaussian to represent distorting features of the electronics, and the mean value taken as the response of the silicon detector to a 1 MIP signal (see figure 4.17). By looking at these values across one sensor as in figure 4.18, the variation in response of individual strips of the silicon detector can be seen to be quite small.

Several things can be deduced from figures 4.17 and 4.18. Firstly, the silicon detector is definitely capable of registering a 1 MIP signal, thus exceeding design parameters,

which called for a range floor of 3 MIPs. Secondly, across a sensor, the variation is very small, even across strips that had previously needed to be repaired. This

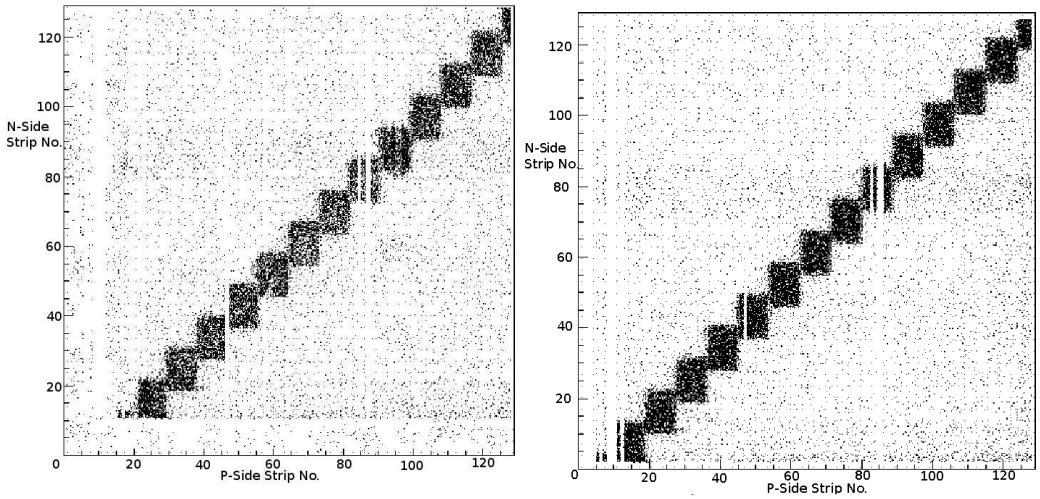

Figure 4.15: In order to guarantee that all strips can be calibrated, some alignment of the x-y table used was obviously necessary. Since the placement of the silicon detectors in their frames was slightly different for each module, alignment runs were taken for every detector. Two typical cases can be seen above. By moving the detector in a diagonal direction transverse to the beam plane, all strips were subject to the beam and this movement pattern ensured that no time was wasted. The situation before alignment is shown on the left, after is shown on the right. The beam profile of a 1 cm$\times$1 cm square can be seen clearly, as can instances where the module had non-functioning or unbonded strips. This is especially prevalent in the above module in channels 1-10 and in channels 80-90 on the p-side of the module.

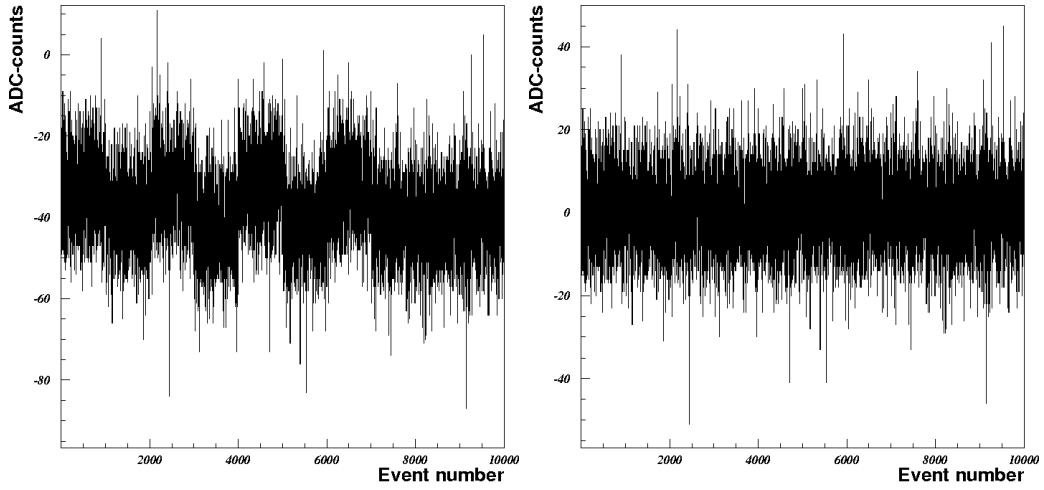

Figure 4.16: Plots of the width of the pedestal signal as a variance with run number. Every time the helix chips were reprogrammed, the width of the pedestal changed—this can be seen in the above plot by consideration of the variation in width every 100 runs (left plot). This was corrected by setting a common baseline for the pedestal value across all runs, resulting in the right plot, which shows a good consistency for absolute pedestal value across all the runs taken.

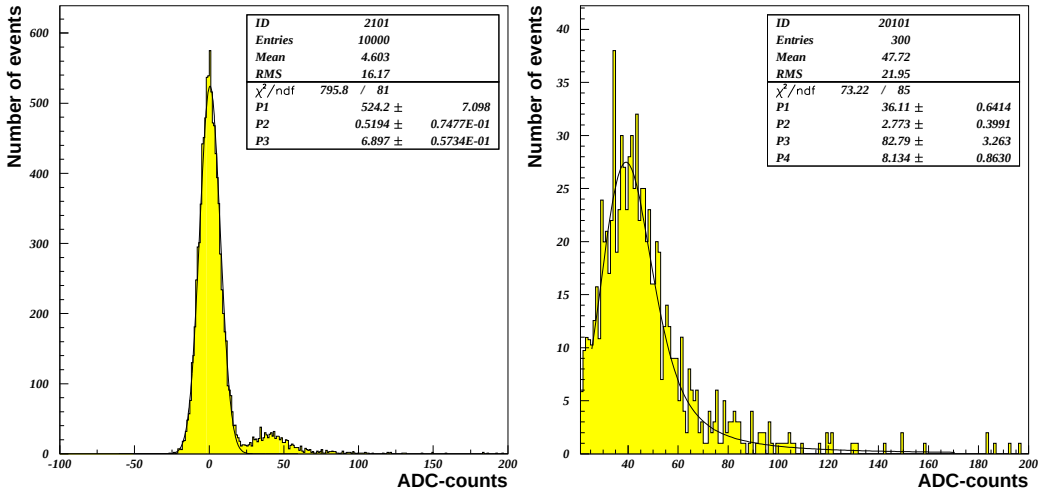

Figure 4.17: The response of the silicon detector to a 1 MIP signal. On the left plot the entire signal with the pedestal value is seen over 1000 runs. The right plot shows the same picture with the pedestal cut away. The shape is well described by a Gaussian distribution convoluted with a Landau distribution. See text.

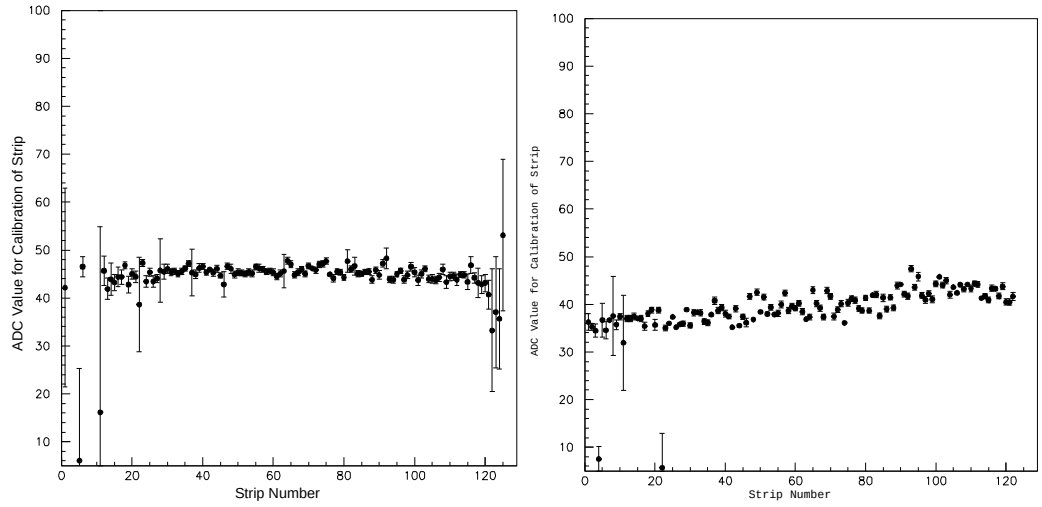

Figure 4.18: The response of each strip for one sensor n-side (left) and p-side (right). The lack of variation is important as it points to the fact that even unbonded strips can be assumed to have a similar response once repaired. This means that those strips that were unbonded at the time of calibration can be assumed to have some calibration value similar to there surrounding strips, allowing full use of the sensor. The error bars reflect the spread in values returned by the sensor strip over the 10,000 run period.

is significant because at the time that this calibration took place, some strips were unbonded (this can be seen clearly in figure 4.15) due to manufacturing faults. Due to the lack of variation, it could be possible that through consideration of the calibration values for surrounding strips, an interpolated value could give an acceptable calibration value for one of these unbonded strips. Thirdly, there is a tendency for there to be a geometric variation in values across the sensor e.g. the

strips on the edge of an n-side sensor have lower values than those in the centre. From this one can conclude that, if a strip's calibration value is to be estimated, it should be from other strips immediately in the vicinity. In addition to verifying the response of the silicon detector to a 1 MIP signal, the tests at T22 can be used to measure the efficiencies of the detectors. Under the supposition that the telescope arrangement, with three overlapping sensors and two scintillator panels provides a perfectly efficient reference system, efficiencies for the silicon detector have been calculated on a per-strip basis for each 10,000 runs sample size, and a sample plot is shown in figure 4.19.

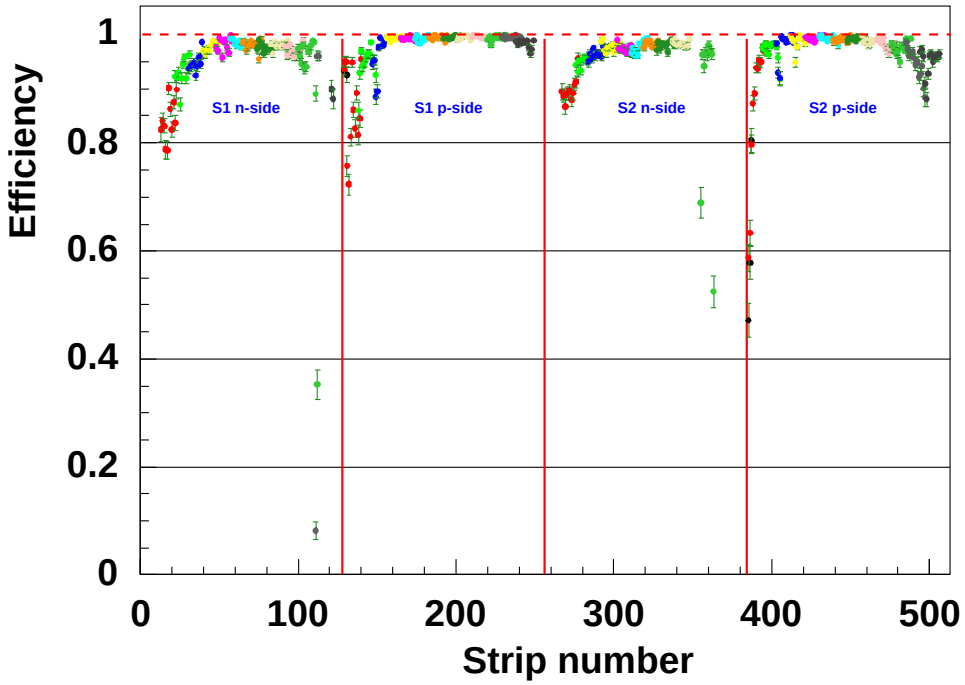

Figure 4.19: The efficiencies of a typical silicon module, for n-side (far left) and p-side (centre left) of the upstream sensor and n-side (centre right) and p-side (far right) for the downstream sensor. The usual geometrical features that were first noticed in this test are easily apparent here in the substandard efficiencies of the detector in the first and last ten strips of each sensor. The different coloured points correspond to different data runs, corresponding to the squares found on the plots in figure 4.15.

4.4.2 The Cosmics Test

In order for a detector as complicated as the recoil detector to be installed into a system as vast as the HERMES spectrometer, a period of four weeks or so is needed. Since HERMES shares the HERA ring with two other major experiments a shutdown period has to be agreed throughout the entire DESY institute and there was therefore a period of four months where the recoil detector was ready to be

assembled, but could not be integrated with the spectrometer. As a proof-of-concept experiment, and in order to practice and make certain that all the detector pieces fit together as planned, the recoil detector was assembled as a stand alone unit in the East Hall [PVZ05]. After mechanical assembly, the photon detector was configured to act as a trigger for cosmic muons in order to test the readout capabilities of the assembled detector. More than 1TB of data was taken, and the passage of muons was tracked through all three subdetectors, as seen in figure 4.20.

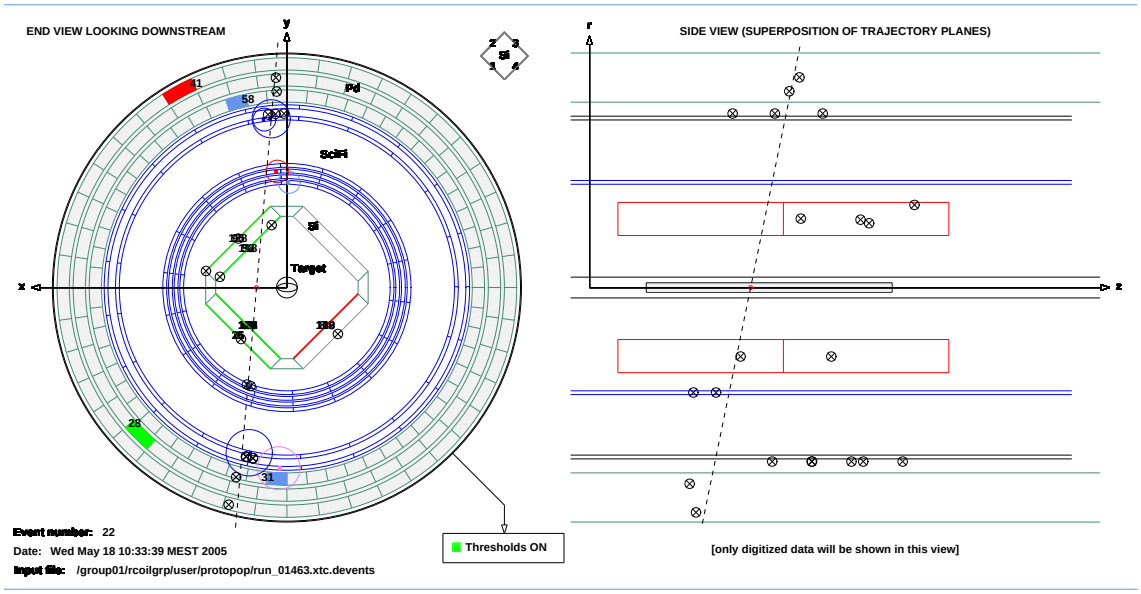

Figure 4.20: A single cosmics event track as seen through the Recoil Detector. The left picture shows the track and recoil detector face on, from the downstream direction. The right picture shows the event as seen by a viewer standing parallel to the recoil detector in the beam direction. The straight lines on the left-side picture do not pass through the particle vertices as they indicate the original ϕ-angle before the track is bent by the magnetic field.

4.5 Integration with the HERMES Spectrometer

The Recoil Detector was installed in the HERMES spectrometer in November 2005 [LPR+06]. Installed around the target cell, it has been confirmed as working to within operational parameters, with software development for tracking and particle identification constantly undergoing improvements. Protons from DVCS event candidates have been detected and tracked through the detector, and at time of writing, more than 40 million DIS events have been recorded across the whole system. The tracking system is a backend C-code with a front end visual display written in Tcl/Tk capable of displaying the track both face on to the detector and with a view

parallel to the beam pipe, as in figure 4.21. Tracking efficiency is expected to rise to 99% after work on the software has been completed. Resolution for the tracking is limited only by the hardware.

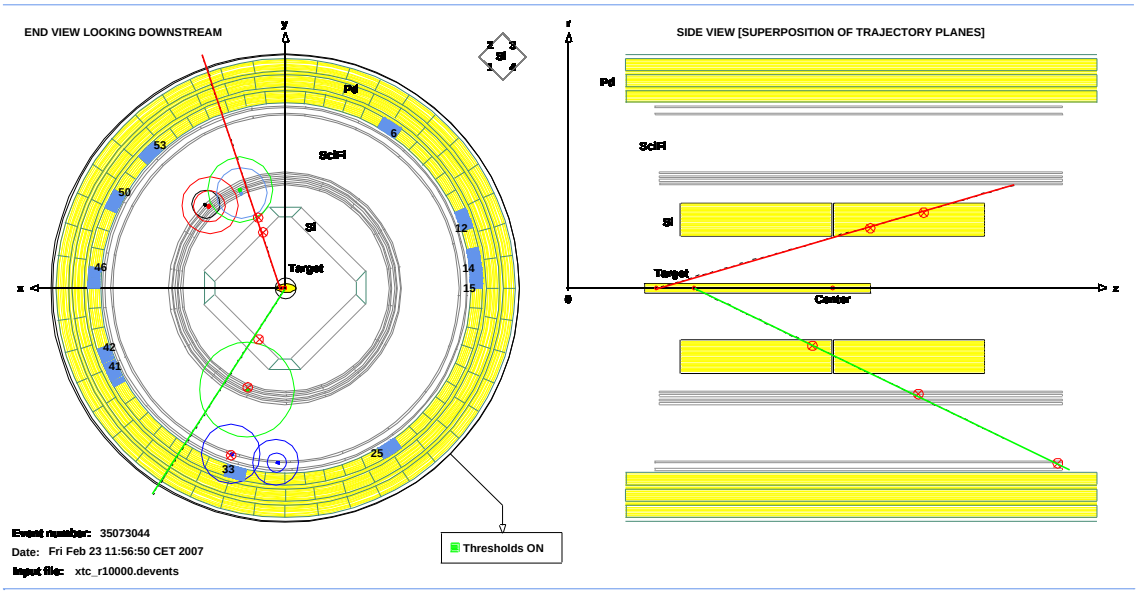

Figure 4.21: Event display picture showing reconstruction of tracks using two different tracking methods. The red track is reconstructed from the energy deposited in the silicon detector and the green track is reconstructed by the inhomogeneous field technique which uses data from both the silicon and SFT subdetectors.

This chapter has described in some detail the work that the author has been involved in regarding the HERMES recoil detector. The design and particulars of the silicon components have been discussed and the calibration tests that the detector underwent have been described. The data from the detector once integrated into the HERMES spectrometer has not been discussed, as it is ongoing work in which the author has not been involved.

The DVCS group at HERMES is currently concentrating on analysis with the Recoil Detector. An analysis schedule is expected to be completed in 2007 and will focus on the extraction of Beam Charge and Beam Spin Asymmetries in DVCS data from the Recoil + HERMES dataset.

Chapter 5

Transverse Target Spin Asymmetries in DVCS

As alluded to in chapter 2, the DVCS interaction is difficult to access at the HERMES experiment. From raw data to the constraint on the total angular momentum contribution of the quarks to the nucleon, there are three separate steps:

1. Extraction of the Exclusive Event Sample;
2. Extraction of the TTSA amplitude from the data sample;
3. Extraction of the constraint on J_u+J_d through combination of simulated asymmetries and extracted TTSA amplitude from step 2.

The first two items on this list are covered in this chapter, the third is covered in chapter 6.

5.1 Extraction of the Event Sample

The final state of the DVCS sample is identical to the final state of the Bethe-Heitler process as described in chapter 2. In this previous chapter, it is explained that the best strategy for accessing the DVCS asymmetries at HERMES lies in the consideration of the interference term in the final cross section. Prior to explaining exactly how this can be done, some kinematic definitions are necessary, and some explanations of the features and limitations of the subdetectors that are used in the HERMES spectrometer. It is stated here for completeness that every piece

of data discussed herein was obtained using an e^+ or e^- beam and a transversely polarised Hydrogen target as described in chapter 3. The format of the HERMES data structure, seen in figure 5.1, means that the cut is applied on a run, burst or event level. This will be stated in the relevant explanations.

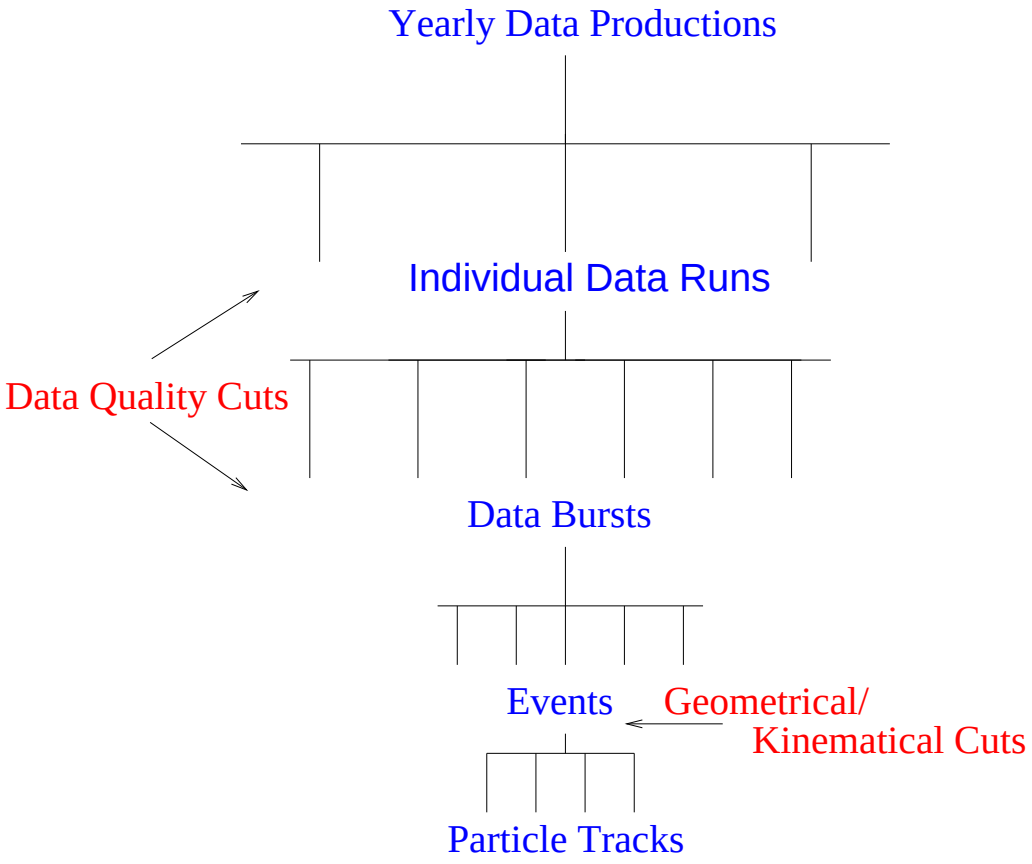

Figure 5.1: The HERMES data structure, with an indication on which level the data cuts are applied. Due to the nature of the HERA beam and the HERMES DAQ, each yearly run period is split into data runs which occupy ∼450 Mb storage space each. These runs then have a burst structure which lasts 10 s. Within each burst there are time–discrete events, which are analysed as physics events.

In chapter 2 the kinematics of a regular DIS event were discussed, and the variables Q^2, x_B and t were used, and described. In the next section, the process is described in detail, with all the variables defined. The kinematic range over which the measurement is made is also defined.

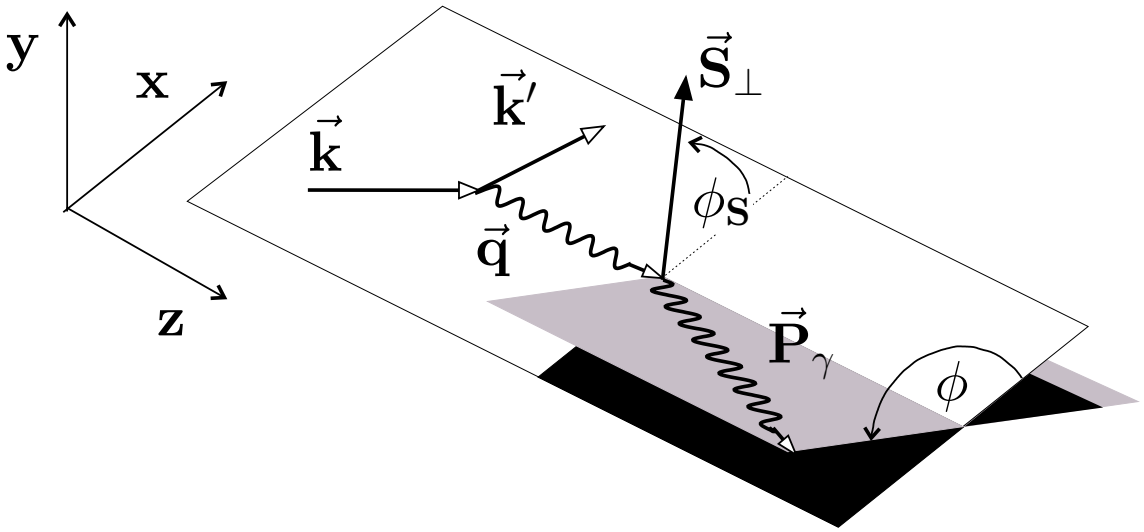

Figure 5.2: Angle definitions for TTSA calculations. $S_\perp$ is the direction of the target polarisation, ϕ is the angle between the lepton scattering plane and the produced photon plane and ϕ_s is the angle between the target polarisation direction and the lepton scattering plane.

5.1.1 Kinematic Definitions

As stated previously, a DVCS event involves a lepton scattering from a proton via the virtual mechanism, with both incidental particles present in the final state, in addition to a produced photon. In the rest of this discussion, the following definitions will be used:

- **k** is the four momentum of the initial (beam) lepton.
- **P** is the four momentum of the initial (target) proton, taken as being at rest.
- **k'** is the four momentum of the scattered (detected) lepton.
- **P'** is the four momentum of the scattered (not-detected) proton.
- **q'** is the four momentum of the produced (detected) photon.

These five terms add to produce the equation of the interaction:

$$e^{\pm}(\mathbf{k}) + P(\mathbf{P}) \rightarrow e^{\pm}(\mathbf{k'}) + P(\mathbf{P'}) + \gamma(\mathbf{q'}). \tag{5.1}$$

In the following, the convention from chapter 2 that $\cong$ means "in the lab frame" is used.

The angles used in the following analysis can be seen in figure 5.2 and are described thus:

- ϕ is the azimuthal angle between the lepton plane and the track of the produced photon. It is is calculated as

$$\phi = \frac{\vec{q} \times \vec{k} \cdot \vec{P_\gamma}}{\left| \vec{q} \times \vec{k} \cdot \vec{P_\gamma} \right|} \cdot \arccos\left(\frac{\vec{q} \times \vec{k}}{\left| \vec{q} \times \vec{k} \right|} \cdot \frac{\vec{q} \times \vec{P_\gamma}}{\left| \vec{q} \times \vec{P_\gamma} \right|} \right). \tag{5.2}$$

- ϕ_s is the azimuthal angle between the target polarisation direction and the lepton plane. It is defined in a way similar to ϕ as follows:

$$\phi_s = \frac{\vec{q} \times \vec{k} \cdot \vec{S_\perp}}{\left| \vec{q} \times \vec{k} \cdot \vec{S_\perp} \right|} \cdot \arccos\left(\frac{\vec{q} \times \vec{k}}{\left| \vec{q} \times \vec{k} \right|} \cdot \frac{\vec{q} \times \vec{S_\perp}}{\left| \vec{q} \times \vec{S_\perp} \right|} \right). \tag{5.3}$$

The results are binned in three kinematic quantities. One of these is Q^2, defined as

$$Q^2 = -\mathbf{q}^2 = -(\mathbf{k} - \mathbf{k}')^2 \cong 4EE' \sin^2\left(\frac{\theta}{2}\right). \tag{5.4}$$

It is the negative square of the four-momentum of the exchanged virtual photon, whose characteristics can be discovered by the subtraction of the scattered lepton from the initial beam lepton. It was first discussed in section 2.1, but is redefined here for clarity.

The energy of the virtual photon is referred to as ν, the same as DIS in section 2.1, and is defined as:

$$\nu = \frac{\mathbf{P.q}}{M_p} \cong E - E' \tag{5.5}$$

where M_p is the rest mass of the proton. The fraction of the proton's momentum that the struck quark carries is the second binning variable and is called x-Bjorken, x_B,

$$x_B \equiv \frac{Q^2}{2\mathbf{P.q}} \cong \frac{Q^2}{2M_p\nu}. \tag{5.6}$$

The Mandelstam invariant mass variable t can be calculated using either the protons or photons of the interaction:

$$t = (\mathbf{P} - \mathbf{P'})^2 = (\mathbf{q} - \mathbf{q'})^2 \cong -Q^2 - 2E_\gamma(\nu - \sqrt{\nu^2 + Q^2}\cos\theta_{\gamma\gamma^*}) \tag{5.7}$$

but since, at HERMES, the scattered proton is undetected, it is usually calculated using the photons. The missing mass of the interaction is defined as

$$M_x^2 = M_p^2 + 2M_p(\nu - E_\gamma) + t. \tag{5.8}$$

If we assume that $M_x \equiv M_p$ for our reaction sample, i.e. that we are dealing solely with exclusive events, then we get a new way to calculate the photon energy that doesn't rely upon the calorimeter resolution,

$$E_\gamma = \frac{t}{2M_p} + \nu \tag{5.9}$$

which can be put into the expansion of t from eqn. (5.7) to give a "constrained t", written t_c and is defined as

$$t_c = \frac{-Q^2 - 2\nu(\nu - \sqrt{\nu^2 + Q^2}\cos\theta_{\gamma\gamma^*})}{1 + \frac{1}{M_p}(\nu - \sqrt{\nu^2 + Q^2}\cos\theta_{\gamma\gamma^*})}. \tag{5.10}$$

As explained in chapter 3, this is important since the only measurement of momentum of the photon is given by the calorimeter (since charge-neutral particles are invisible to the regular HERMES momentum reconstruction method). This momentum measurement has a resolution of 5%, which is an order of magnitude higher than the calculated resolution for elastic events. More details on the effects of using t_c as opposed to t can be found in references [Ye06] and [Ell04]. t_c is used in this analysis and it is t_c which is the third binning variable.

For the purpose of the DIS cuts another variable, W (the squared invariant mass of the proton-virtual photon system) is defined as

$$W^2 = (\mathbf{P} + \mathbf{q})^2 \cong M_p^2 + 2M_p\nu - Q^2. \tag{5.11}$$

Using these definitions, events can be cut away to leave a DIS sample and an exclusive sample. The cuts for the standard HERMES DIS sample require

- $W^2 > 9$ GeV^2 ensures that the Monte Carlo fragmentation model (which is used as a standard way of estimating and subtracting the background) works.

- $Q^2 > 1$ GeV^2 is needed to satisfy the requirement of factorisation of the DIS process. Ideally, the requirement would be that $Q^2 \gg 1$ GeV^2, however the HERMES data set reduces exponentially as Q^2 increases linearly and this requirement would remove too many events from the data set.

- $\nu < 22$ GeV is a companion cut to the $\gamma > 5$ GeV cut described above and discards events in which the efficiency of the calorimeter is believed to be suspect [YMMN06].

In addition, cuts to the data sample are applied in order to remove the non-exclusive events. These cuts are as follows:

- The missing mass term M_x^2 as defined in equation (5.8) is examined in order to ensure that only events with missing mass terms that are consistent with that of a proton are included in the data sample:

  $-2.25\ GeV^2 < M_x^2 < 2.89\ GeV^2$. This corresponds to the exclusive peak in the data sample and helps to remove some background events — see figure 5.3. The upper cut of 2.89 GeV^2 corresponds to the point at which the contribution to the event sample from DVCS events is equal to that of associated production.

- In order to aid in background subtraction, a cut on t_c is applied. Since exclusive events have vanishing momentum transfer, t_c offers another possibility to determine an exclusive event sample, alongside the cut on missing mass. The cut applied is $\mid t_c \mid < 0.7$ GeV^2. More details on this cut can be found in reference [Ell04].

- Finally, in order to define a strict kinematic regime for the results of the analysis, boundary cuts $0.03 < x_B < 0.35$ and $Q^2 < 10\ GeV^2$ are applied. These have a minimal effect, as almost all of the events which pass the other cuts also pass these.

Having defined kinematic and physics cuts for the event sample, some consideration must be made for more practical aspects of data selection. Cuts on the data sample must be made with the behaviour of the experimental apparatus evaluated. Such cuts are described in the next section.

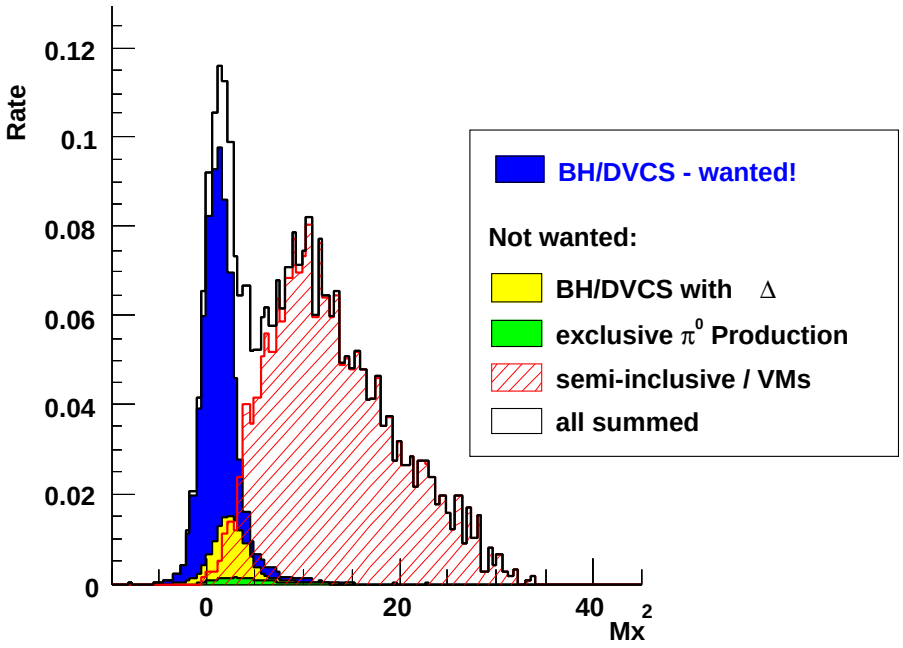

Figure 5.3: The missing mass distribution at HERMES kinematics from a Monte Carlo simulation. Of the competing processes, the analysis in this thesis is performed on the BH/DVCS interference term, and the missing mass cut of $-2.25\ GeV^2 < M_x^2 < 2.89\ GeV^2$ is chosen to isolate that sample. The main background process is associated production, on the 10% level. The cut extends into the negative mass region due to smearing effects in the detector.

5.1.2 Data Quality Cuts

The HERMES spectrometer is a mature detector, having been operational for a decade. During this time many studies have been performed in order to ensure that a distinct set of criteria can be defined such that any data burst that passes these can be considered free of undue influence arising from rise time in detectors, poor beam conditions or other detrimental factors. A set of lists of these is therefore presented, and the reasons for the cuts. These lists are based upon those presented in [YMMN06]. The first list is compiled by the data quality group in HERMES, who mark each data burst with a bit pattern (0x5D9FFFDD) that corresponds with the following criteria:

- Poor data taking conditions can arise from many different sources, not all of them are detected by the HERMES automatic monitoring system. Therefore, each analysed run was marked as analysable by the shift leader responsible for that data taking period.
- There were no high voltage trips in the tracking chambers.

- No faults were reported by the luminosity monitor, the calorimeter, the preshower detector or the Transitional Radiation Detector.
- The measured beam current I_{beam} conformed to normal running parameters, i.e. $2 \leq I_{beam} \leq 50mA$.
- The last measurement of the beam polarisation was less than 5 minutes prior to the data taking period.
- The nucleon target's spin was not in an incorrect direction.
- The ratio of luminosity to current L/I_{beam} was within normal operational parameters i.e. $1 \leq L/I_{beam} \leq 50$.
- The DAQ system was operational more than 50% of the time i.e $0.5 \leq DAQ \leq 1.0$.
- The burst length was observed to be of a normal duration i.e $0 \leq time_{burst} \leq 11$.
- The burst was not the first burst in a run, meaning that no detectors are operating within their rise period.

In addition to these cuts defined by the data quality group, the DVCS group at HERMES has its own set of cuts to ensure that the data used is of high quality. In the following lists, quantities are referred to as `name1.name2` where `name1` is the name of the μDST-table containing the information and `name2` is the name of the variable within that table. As with the above list, these cuts are applied on a burst level:

- `g1Quality.iTrdDQ==3` ensures that, if there was no information available on the status of the TRD, the burst is discarded.
- $-80 <$`g1Beam.rPolFit`< 80 || (`g1Beam.rPolFit==0 &&` $-80 <$`g1Beam.rPol`< 80) restricts the measured beam polarisation levels to those that can truly be measured by the polarimeters.
- `(g1DAQ.iTargetBit & 0x02)!=2` ensures that the target was not in a state of spin flip.
- $5 <|$`g1Target.rPol`$|< 1.5$ ensures that the target polarisation, uncorrected for atomic fraction (defined in equation (3.8)), is suitably large.

- 5 <`g1Beam.rLumiRate`< 3000 ensures that the measured luminosity rate is of a reasonable size.
- 0.8 <`g1DAQ.rDeadCorr21`$\leq$ 1.0 ensures that the DAQ is active for more than 80% of the burst.
- `g1Beam.HeraE1Energy`>`27GeV` ensures that the beam energy is marked correctly.

If the data for a burst passes all these criteria, the burst is marked as analysable. This does not, however, mean that all the events inside the burst are acceptable. Due to limitations of the detectors, several other quality cuts are applied, strictly on a per-track basis. These relate to geometrical features of the detector.

5.1.3 Geometrical Cuts

The HERMES spectrometer has several unique geometrical features that can deflect a particle track internally, or cause the reconstruction of the track to become suspect. The cuts applied to minimise these effects are detailed as follows:

- `(g1Track.iSelect & 0x0100) && (g1Track.iSelect & 0x0200)` ensures that the long tracking method is used inside the spectrometer reconstruction code—that the track passed through all the tracking detectors in the spectrometer.
- `g1Track.bTMCStat` & `0x80000000==0` for 2002 and 2005 data and `g1Track.bTMCStat` & `0x00008000==0` for 2003 and 2004 data. All charged tracks in the target region of the spectrometer are partially deflected by the transverse target magnet. There are two different correction methods available to compensate for this, but one requires an accurate field map of the magnet, which is not available in all years. This cut ensures that the influence of the transverse magnet is nullified by whichever one of these correction methods is deemed most suitable by the HERMES data quality group.
- $|\ z_{vtx}^{e^\pm}\ |<$ 18 `cm` ensures that the z-position of the interaction is within the target cell.
- $|\ x_{calo}^{e^\pm}\ |<$ 175 `cm`,30 `cm`$|\ y_{calo}^{e^\pm}\ |<$ 108 `cm` ensures that the position of the scattered lepton in the calorimeter is such that the calorimeter is able to faithfully reproduce the energy of the particle.

- $|\ x^{\gamma}_{calo}\ | < 125$ `cm, 33 cm`$< |\ y^{\gamma}_{calo}\ | < 105$ `cm` ensures that the position of the real produced photon in the calorimeter is such that the calorimeter is able to faithfully reproduce the energy of the particle. This cut is different to that of the corresponding one for a lepton due to the different behaviour of a photon and a lepton shower in the calorimeter.

- |`smTrack.rxOff+172`$\times \tan\theta_x\ | < 31$ `cm`,
  `7cm`$<$|`smTrack.ryOff+172`$\times \tan\theta_y\ | < 54$ `cm`,
  |`smTrack.rXpos+108`$\times$`smTrack.rXslope`$| \leq 100$ `cm` and
  |`smTrack.rYpos+108`$\times$`smTrack.rYslope`$| \leq 54$ `cm` ensure that the lepton track inside the spectrometer does not get deflected by the septum magnet plates that encroach on the possible track paths inside the spectrometer.

- The photon should create a signal in the preshower detector in order that it does create a shower in the calorimeter, allowing an accurate energy reconstruction, i.e. $\mathrm{E}_{pre} >$`1 MeV`.

- The energy of the photon in the in the calorimeter should be large enough that the calorimeter can accurately measure it, i.e. $\mathrm{E}_{\gamma} > 5$ GeV.

- $\theta_{\gamma\gamma^*}$, the angle between the virtual photon and real photon trajectories should be in a region where smearing effects do not allow for the possibility that $\theta_{\gamma\gamma^*} \leq 0$ mrad since, from the definitions made earlier, the azimuthal angle ϕ is not defined in this region. An upper cut is necessary since at an angle of $\theta_{\gamma\gamma^*} <$ 70 mrad, acceptance in ϕ is no longer complete. Information from a Monte-Carlo study shows that for $\theta_{\gamma\gamma^*} > 45$ mrad is dominated by background events and so a final cut of `5 mrad`$\leq \theta_{\gamma\gamma^*} \leq$`45 mrad` is applied. More information on this cut is to be found in ref. [Ell04].

If an event passes these conditions then it is taken to be a good event and is a candidate to be considered for inclusion in the exclusive data sample. However, the event itself then needs to meet the criteria for a BH/DVCS event. In order to exclude events that originate from interactions other than BH/DVCS, some simple cuts are made to ensure that there is just one photon and just one lepton in any event.

- The number of tracks (i.e. charged particles) detected by the spectrometer is exactly one and this track has the same sign as the incident lepton beam.

- This track is identified as a lepton by the HERMES tracking system, i.e `g1Track.PID2 + g1Track.PID5 >2`.

- Exactly one trackless cluster is detected by the calorimeter, i.e. one photon.

Upon applying these cuts to the HERMES productions 02c0, 03b1 and 04b1 an exclusive event sample of 3813 events remains. This is then the total event sample which HERMES has taken with an e^+ beam. Applying the cuts to the 05b1 data set, a total of 6138 events were obtained with an e^- beam. TTSA amplitudes can now be extracted from these event samples.

5.2 Extraction of the TTSA Amplitude

As written in chapter 2, the TTSA asymmetry in DVCS can be described as

$$A_{TTSA} \approx A^{sc}_{TTSA} \sin(\phi - \phi_s)\cos(\phi) + A^{cs}_{TTSA} \cos(\phi - \phi_s)\sin(\phi) \tag{5.12}$$

and in order to extract the TTSA amplitude from the data set, the angles ϕ and ϕ_s are taken from each event in the exclusive data sample described above and these are fitted with a suitable function. Whilst many physics analyses use a χ^2-fit, the fitting procedure is not always well understood. The next subsection will endeavour to explain why such a fitting method is not always optimal and suggest a more suitable alternative.

5.2.1 Least Squares Fitting

Regular Least Squares (or χ^2) fitting is a particular implementation of maximum likelihood fitting which seeks to vary a parameter set $[a_1 \ldots a_n]$ in order to find which values of the parameter set have the maximum probability of describing the data set by minimising a probability distribution function (p.d.f) [Bev94]:

$$\chi^2 = \sum_{i=1}^{n} \left\{ \frac{1}{\sigma_i^2} [y_i - y(x_i)]^2 \right\} \tag{5.13}$$

where σ_i is the deviation of the data point y_i from the mean distribution of the bin, and $y(x_i)$ is the function believed to describe the data. Such a definition naturally raises some questions:

How valid is this p.d.f for a data set describing only one variable for which there is no describing function? The traditional response to this problem is to histogram

the data set into frequencies, and find a function to describe the shape of that histogram. Such a histogram is naturally dependent on decisions made about its binning and range. Such decisions can influence the shape of the histogram and are taken on aesthetic considerations — the binning can be be said to look good, the resolution of the bins can be said to look correct, or be good enough. Such arbitrary conditions can obviously lead to two different interpretations of the same data set, which in a purely scientific context is less than optimal. We speak of sensible binning considerations, with no easy way to quantitatively express what is meant by the word "sensible", and hence no standard way to arrive at a technique that can be implemented in a consistent manner to achieve an optimal binning for any histogram.

Reducing bin size to the resolution of the measurements is also unsatisfactory, for several reasons. Empty bins can significantly influence the result of the fit, and events within one bin which are not distributed around a Gaussian function whose mean is the centre of the bin can distort the shape and results of a fit, making the fit function appear to be a better or worse fit to the data than it really is. Any such fit is in fact not a fit to the data, but a fit to *that particular* histogram of the data.

Naturally for a technique that is so widely used, the χ^2 fitting method has many advantages. It is relatively simple to implement and computationally cheap—each fit point relates to a bin of a histogram, rather than a data point and since in many experimental situations there can be hundreds or thousands of data points in each bin, this is a distinct advantage. Such experiments also benefit from the fact that in most cases a histogram can be chosen such that the events within one bin *do* cluster around a Gaussian distribution whose mean is at the centre of the bin, or a modified version of the fit can be adjusted to take this deviation from bin centre into account. The $\chi^2/d.o.f$ consideration provides a ready-made examination of the quality of the fit. For all these reasons, the χ^2 fit technique remains the standard method of fitting within almost all collaborations in the physics community. However, suppose instead the data set to be measured is one with modest statistics and one for which no obvious binning exists. In this case, some of the advantages of the χ^2 fit become disadvantages. With ever-increasing computer power, computational time is cheap, and for lower statistics no longer a significant consideration [Nyl97]. The distributions of events within histogram bins do become significant for investigations with lower statistics, and the potential introduction of empty bins into the histogram can cause problems. In such a case, it becomes worthwhile to revert to the fitting theory behind the χ^2 fit in an attempt to find a better technique.

5.2.2 The Maximum Likelihood Fitting Technique

The Maximum Likelihood fitting technique is the standard fitting technique used in the high energy physics community, implemented in the CERN MINUIT library and the RooFit ROOT-library. In general terms, the fitting technique is that of finding a p.d.f that can describe the data set which is dependent upon parameter set $[a_1 \dots a_n]$ and varying those parameters, sometimes within a set of limits, in order to maximise the function, i.e.

$$\mathcal{L}(\vec{\alpha}) = \prod_{i}^{n} p(x_i, \vec{\alpha}) \tag{5.14}$$

where $p(x_i, \vec{\alpha})$ is the probability of parameter set $\vec{\alpha}$ describing each data point x_i. In reality, since $\mathcal{L}$ is maximised at the same parameter set $\vec{\alpha}$ that $-\ln \mathcal{L}$ is minimised, the goal of the fitting procedure is usually to minimise the latter, as a large product of small numbers can lead to rounding errors in a standard computing environment and the negative logarithm of the likelihood has been shown to often be analytically simple in the region of its minimum. Therefore

$$-\ln \mathcal{L}(\vec{\alpha}) = -\sum_{i}^{n} \ln(p_i, \vec{\alpha}) \tag{5.15}$$

is often the function to be minimised.

Putting the "fun" in Fitting Function

As a probability density function, the fitting function that is to be minimised absolutely requires to be normalised to its integral. In the case of the TTSA asymmetry in DVCS, this means finding a normalisation of the function seen in equation (2.34) as applied to the HERMES spectrometer, taking into account the efficiency and acceptance of the spectrometer. This leads to a functional form of

$$
\begin{aligned}
f_{\pm}(\phi, \phi_s, t, x_B, Q^2, \vec{\alpha}) \;=\; & \frac{1}{C^{\pm}(\vec{\alpha})} \cdot \\
& \epsilon(\phi, \phi_s, t, x_B, Q^2) \cdot \sigma_{UU}(\phi, t, x_B, Q^2) \cdot \\
& \Big[1 \pm A_{UT}^{s(\phi-\phi_s)c\phi}(t, x_B, Q^2) \sin(\phi - \phi_s) \cos\phi \pm \\
& A_{UT}^{c(\phi-\phi_s)s\phi}(t, x_B, Q^2) \cos(\phi - \phi_s) \sin\phi \Big]
\end{aligned}
\tag{5.16}
$$

where:

- $\pm$ refers to the target polarisation state
- $\epsilon(\phi, \phi_s, t, x_B, Q^2)$ is the detection efficiency
- $\sigma_{UU}(\phi, t, x_B, Q^2)$ is the cross section of an unpolarised beam on an unpolarised target
- $A_{UT}^{s(\phi-\phi_s)c\phi}$ is the first asymmetry amplitude, which has an additional dependence on $|S_\perp|$, the target polarisation
- $A_{UT}^{c(\phi-\phi_s)s\phi}$ is the second asymmetry amplitude, which also has an additional dependence on the target polarisation
- $C^{\pm}(\vec{\alpha})$ is the set of normalisation integrals which act in order to turn equation (5.16) into a probability density function.

Note from equation (5.16) that the effects for efficiency ϵ and the unpolarised acceptance σ_{UU} do not depend upon the parameter set $\vec{\alpha}$ and so can be safely ignored when finding the values of $\vec{\alpha}$ as they will not change the minimal point of the log likelihood function in parameter space.

Normalisation equations $C_{\pm}(\vec{\alpha})$ must be evaluated with regard to ϵ and σ_{UU} in order to provide a correct normalisation however. This leads to a second set of equations that are referred to as the *reduced* likelihood:

$$
\begin{aligned}
\mathcal{L}'_{\pm}(\vec{\alpha}) \;&=\; \mathcal{L}'_{+}(\vec{\alpha}) \cdot \mathcal{L}'_{-}(\vec{\alpha}) \\
&=\; \prod_{i=1}^{N^*_{\pm}} \frac{\Big[1 \pm A_{UT,i}^{s(\phi-\phi_s)c\phi}(\vec{\alpha}) \sin(\phi_i - \phi_{s,i}) \cos\phi_i \pm A_{UT,i}^{c(\phi-\phi_s)s\phi}(\vec{\alpha}) \cos(\phi_i - \phi_{s,i}) \sin\phi_i \Big]}{C'_{\pm,i}}
\end{aligned}
\tag{5.17}
$$

where N^* refers to the number of events in the exclusive event sample and only the parameter dependent parts of the likelihood function are evaluated. In equation (5.17) $C'_{\pm,i}$ refers to the fit parameter dependent parts of the normalisation integrals:

$$C'_{\pm,i}(\vec{\alpha}) = \frac{1}{N^{DIS^+}} \sum_{i=1}^{N^*_+} \mathcal{A}_{TTSA,i}(\vec{\alpha}) + \frac{1}{N^{DIS^-}} \sum_{i=1}^{N^*_-} \mathcal{A}_{TTSA,i}(\vec{\alpha}) \tag{5.18}$$

where N^{DIS} refers to the total number of DIS events seen in that production and

$$\mathcal{A}_{TTSA,i}(\vec{\alpha}) = 1 \pm A_{UT,i}^{s(\phi-\phi_s)c\phi}(\vec{\alpha}) \sin(\phi_i - \phi_{s,i}) \cos\phi_i \pm A_{UT,i}^{c(\phi-\phi_s)s\phi}(\vec{\alpha}) \cos(\phi_i - \phi_{s,i}) \sin\phi_i \tag{5.19}$$

However, as per equation (5.15), it is the negative natural logarithm of the likelihood which is evaluated computationally, and so we arrive at the eventual fitting function

$$\begin{aligned} -\ln(\mathcal{L}') &= -\Bigg(\sum_{i=1}^{N^*_+} \Big[\ln(1 + A_{1,i}(\vec{\alpha}) \sin(\phi_i - \phi_{s,i}) \cos\phi_i + A_{2,i}(\vec{\alpha}) \cos(\phi_i - \phi_{s,i}) \sin\phi_i) \Big] \\ &+ \sum_{i=1}^{N^*_-} \Big[\ln(1 - A_{1,i}(\vec{\alpha}) \sin(\phi_i - \phi_{s,i}) \cos\phi_i - A_{2,i}(\vec{\alpha}) \cos(\phi_i - \phi_{s,i}) \sin\phi_i) \Big] \\ &- 2 \times \log \Big[\sum_{i=1}^{N^*} (1 + A_{1,i}(\vec{\alpha}) \sin(\phi_i - \phi_{s,i}) \cos\phi_i + A_{2,i}(\vec{\alpha}) \cos(\phi_i - \phi_{s,i}) \sin\phi_i) \Big] \\ &- 2 \times \log \Big[\sum_{i=1}^{N^*} (1 - A_{1,i}(\vec{\alpha}) \sin(\phi_i - \phi_{s,i}) \cos\phi_i - A_{2,i}(\vec{\alpha}) \cos(\phi_i - \phi_{s,i}) \sin\phi_i) \Big] \Bigg) \\ &+ \ldots \end{aligned} \tag{5.20}$$

where ... relates to terms dependent upon DIS numbers for each target state, having no affect on the position of the minimum of the function in parameter space.

One additional item that must be noted is that the target polarisation of the data set is included in the $A_{1,2}$ values given in equation (5.20). In order to achieve the true values of the TTSAs, one must then divide $A_{1,2}$ by the target polarisation, i.e:

$$\begin{aligned} A_{sc} &= \frac{A_1}{\langle T_{pol} \rangle} \\ A_{cs} &= \frac{A_2}{\langle T_{pol} \rangle}. \end{aligned} \tag{5.21}$$

The Maximum Likelihood method has some drawbacks. It is computationally ex-

pensive, as the fit must work over all events, rather than just a binned set of events. There is no standard indicator of quality-of-fit, like the $\chi^2/d.o.f$ measurement provides. However, in order to extract the maximal amount of statistical information from the data, the Maximum Likelihood fitting technique will be used for the rest of the results presented in this chapter.

5.3 TTSA Amplitudes

Applying the Maximum Likelihood fit method by calling MINUIT from Root, the TTSA amplitudes for two different data sets are obtained. These are extracted from the 2002-04 data from HERMES, taken with a positron beam, and 2005 data from HERMES, taken with an electron beam. In order to check the effect that variation of parameters can have on the likelihood function shown in eqn. (5.15), the values of the likelihood function are plotted in figure 5.4. The results for the TTSA amplitudes are shown in figures 5.5 and 5.6. The error bars show the statistical errors for each asymmetry, whereas the bands show the systematic errors. The systematic errors for the 02-04 data set are taken from reference [Ye06] and the calculations made for the systematic errors for the 05 data set are discussed in section 5.4.

Figures 5.5 and 5.6 clearly show that $A_{sc}^{\sin(\phi-\phi_s)\cos\phi}$ has the power to differentiate between various values of J_u for the model discussed in chapter 6. This potential is explored in that chapter. The bands on the figures are the systematic error contribution, discussed further in section 5.4.

The differences between the 02-04 data set and the 05 data set should mainly stem from the pure DVCS contribution to the cross-section, which is independent of beam charge. In order to show the potential size of such a contribution, figure 5.7 shows the asymmetries for 02-04 added to 05 and divided by two. It can be seen that the DVCS cross-section contribution is in all bins consistent with zero. This conclusion strengthens the case made later in chapter 6 that the two data sets can be combined and that the pure DVCS term is unlikely to have much influence on such a combination.

5.4 Systematic Errors

The previous section outlined the extraction method used to obtain the asymmetry amplitudes and showed the errors related to the limited statistical certainty that can

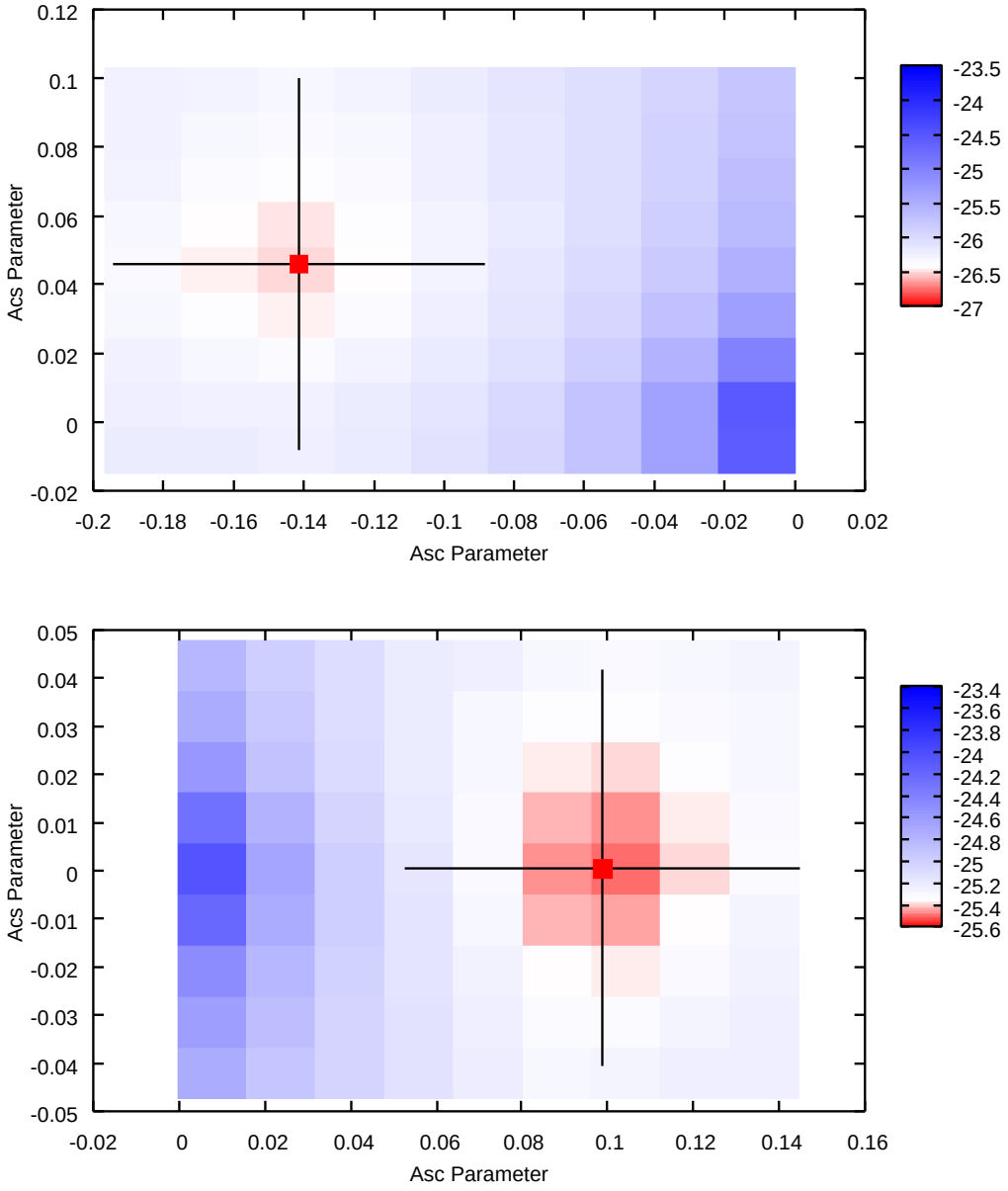

Figure 5.4: The top plot shows the shape of the negative log likelihood function for the 02-04 data set, whereas the bottom plot shows the shape of the same function for the 05 data set. A definite minimum can be seen at the co-ordinates given in table 5.4.

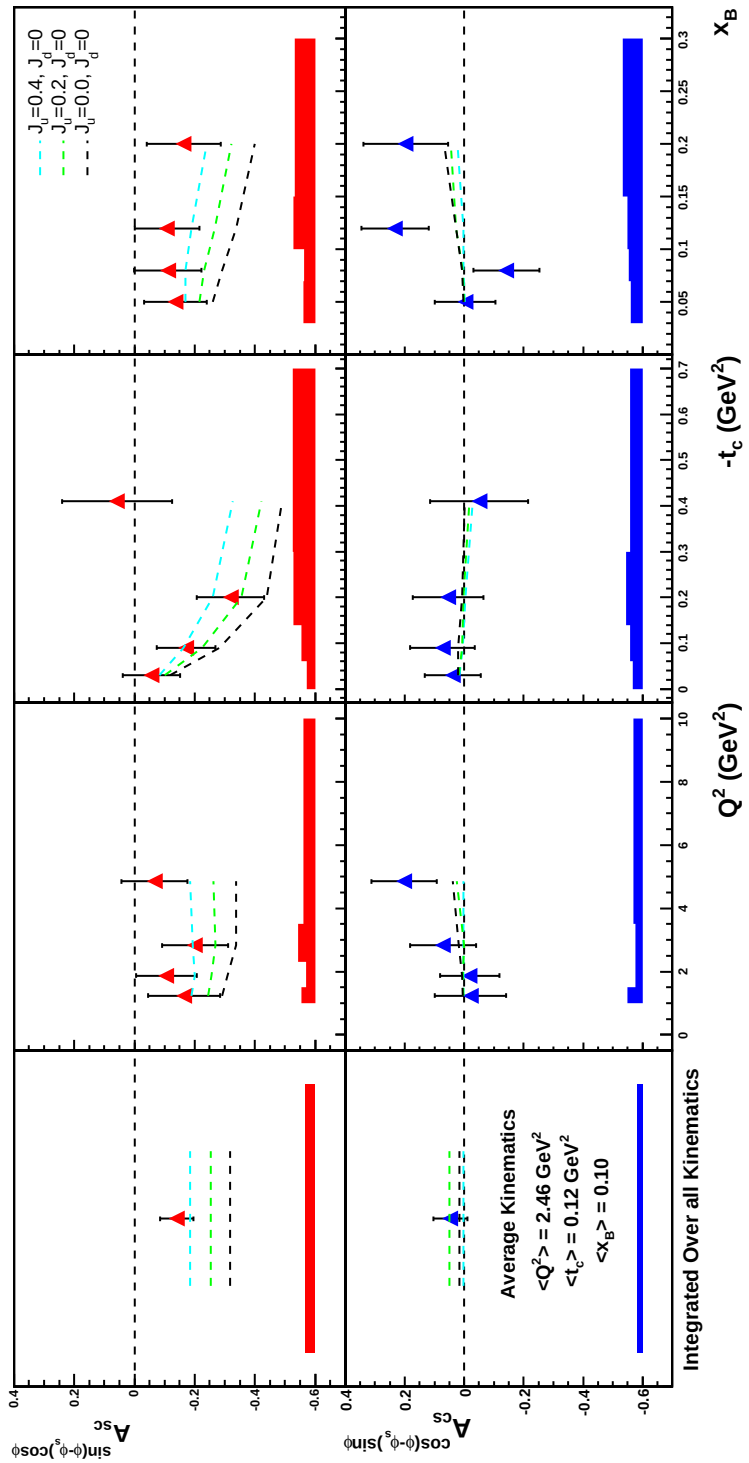

Figure 5.5: The TTSA asymmetries obtained from the 2002-04 data set from HERMES taken with a positron beam, $A_{sc}^{\sin(\phi-\phi_s)\cos\phi}$ in the top panels, $A_{cs}^{\cos(\phi-\phi_s)\sin\phi}$ in the bottom panels. The panels show asymmetries from the integrated data set (far left), binned in Q^2 (centre left), binned in $-t_c$ (centre right) and binned in x_B (far right). Predictions from the VGG model discussed in chapter 6 are shown for values where the contribution to the spin of the proton from the total angular momentum of up quarks is 0.4 (light blue), 0.2 (green) and 0.0 (black). Error bars are statistical errors, bands are systematic errors, taken from reference [Ye06].

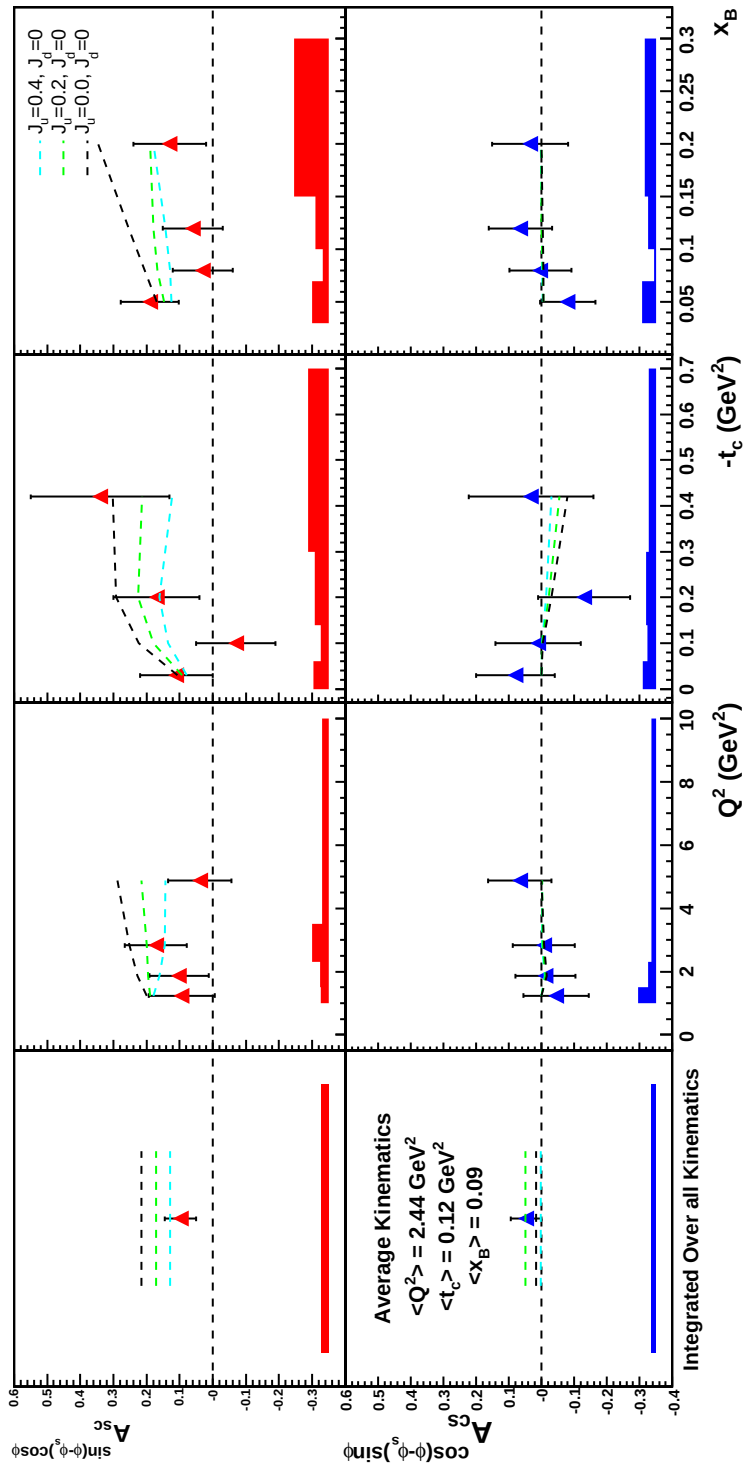

Figure 5.6: The TTSA asymmetries obtained from the 2005 data set from HERMES taken with an electron beam, $A_{sc}^{\sin(\phi-\phi_s)\cos\phi}$ in the top panels, $A_{cs}^{\cos(\phi-\phi_s)\sin\phi}$ in the bottom panels. The panels show asymmetries from the integrated data set (far left), binned in Q^2 (centre left), binned in $-t_c$ (centre right) and binned in x_B (far right). Predictions from the VGG model discussed in chapter 6 are shown for values where the contribution to the spin of the proton from the total angular momentum of up quarks is 0.4 (light blue), 0.2 (green) and 0.0 (black). Error bars are statistical, error bands are systematic. The calculations determining these bands are discussed in section 5.4.

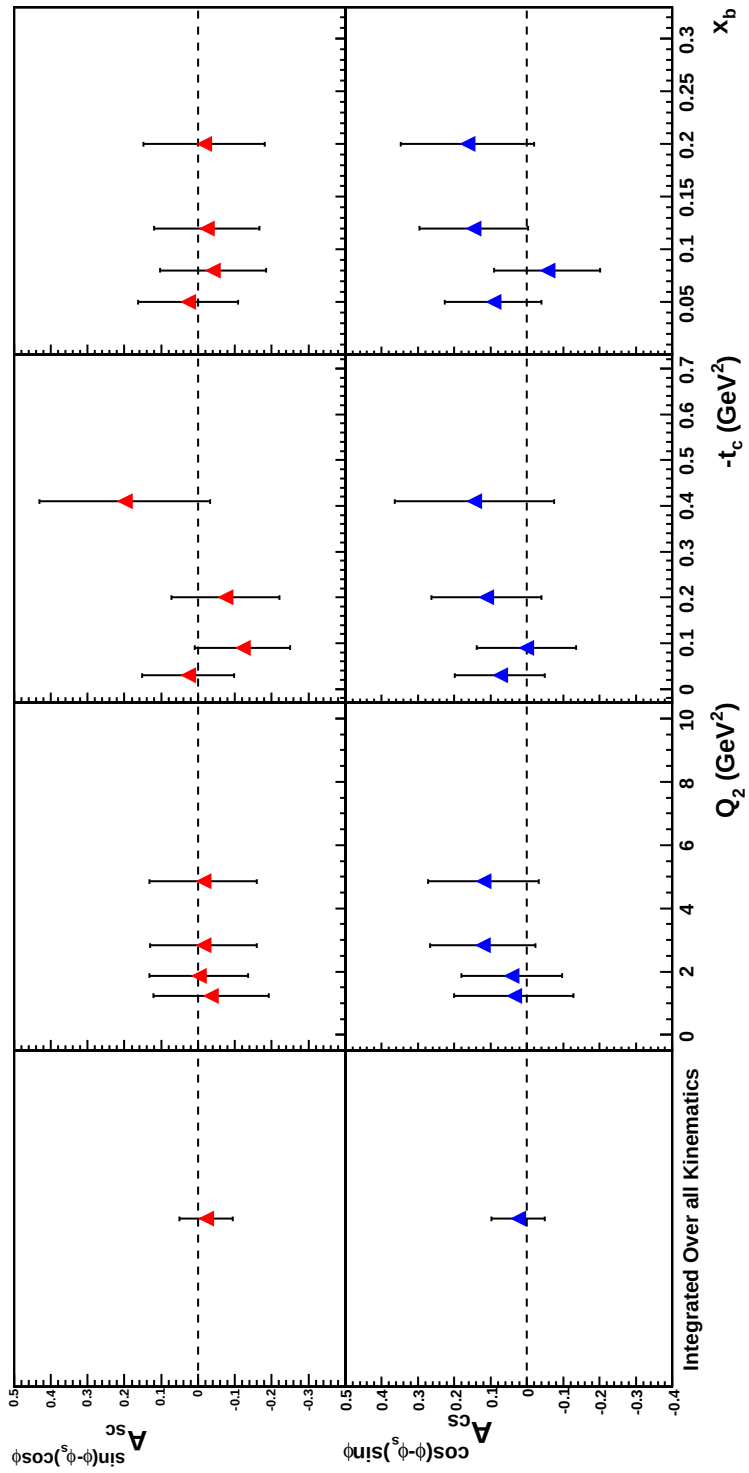

Figure 5.7: The difference in TTSA asymmetries between the 02-04 data set and the 05 data set in the same format as for figure 5.6. Once the two sets of asymmetries are added together, they are in all cases consistent with 0. This lends credence to the theory that the pure DVCS amplitude can safely be neglected at the current level of statistical precision.

be applied to theresults. A more detailed discussion of the potential contributions to the systematic error is also necessary. Due to time constraints, it was not possible to do a Monte-Carlo investigation of the systematic error contributions. Instead, figures from the investigation in [Ye06] are adapted as necessary. This is explained where relevant.

Target Polarisation

As discussed in section 3.2, there is an inherent error in the measurement of the target polarisation. Since our measurement of the asymmetries includes a division by the target polarisation in the final stage, this error must be included in our final measurements. Therefore, in determining the TTSA amplitudes, there is a $\approx 6.6\%$ error from the target polarisation in the 2002-2004 measurements and from the 2005 measurements, there is a $\approx 9.2\%$ error [Ye].

Luminosity

A standard analysis will depend upon the integrated luminosity of the data set. An acceptable alternative is to use the number of DIS events which should be proportional to the luminosity. Since the DIS terms drop out of the fitting function, no error is assigned related to any luminosity issues.

Fit Function

Previous measurements on the TTSA [Ye06] have shown that the extraction proves insensitive to the fit function, which may include 3 or 5 amplitudes in order to account for other asymmetries in the data, including contributions from higher twist processes. Repeating this method of varying the fit function for the 2005 data shows no significant change in the extracted asymmetries.

However, to ensure that there is no unexpected effect, the spread between the three fit functions is assigned as a systematic error. This value can be seen in tables 5.2 and 5.3.

Misalignment

Two variants of misalignment can affect measurements made with the HERMES spectrometer—internal misalignment, meaning that the positions of detectors shift relative to one another, arising from (as example) settling effects of the detector supports or external misalignment, meaning that the entire experimental setup is shifted from the co-ordinate system. This can be due to beam position shifts from different energies and magnet strengths year-on-year or can arise from poorly measured reference points on the spectrometer when first determining the alignment.

Internal misalignment at HERMES is corrected during each run period. Several times per period, the spectrometer is run without any magnetic fields acting on the system. The tracks of leptons through the spectrometer are then straight and so the relative alignments of the subdetectors can be determined. Through the collection of a sufficiently large data set during these runs, the internal misalignment effects can be detected at a resolution better than the resolution of the subdetectors themselves, and can be corrected when processing the raw data into its analysable form. Therefore it is not deemed necessary to take the internal misalignment of the detectors into account when considering the misalignment effects and thus the systematic error of the measurements.

2002-2003	x-slope (mrad)	y-slope (mrad)	x-offset (cm)	y-offset (cm)
Top	-0.18	-0.62	0.30	-0.08
Bottom	-0.42	0.49	0.29	0.11
2002-2003	x-slope (mrad)	y-slope (mrad)	x-offset (cm)	y-offset (cm)
Top	-0.041	-0.13	0.005	0.046
Bottom	0.095	0.059	0.016	0.045

Table 5.1: Spectrometer (top) and beam (bottom) misalignment slopes and offsets for 2002-2003

External misalignment, or offset and rotation of the spectrometer with respect to the beam and co-ordinate system is not so easily dismissed, however. The effect was studied in reference [Bru]. The offset of the spectrometer to the co-ordinate system can safely be ignored as, if we compare the maximum offset of the spectrometer (0.30 cm) from table 5.1 to the minimum distance of the photon detected in the calorimeter (33 cm) it becomes apparent that the potential for error finds a maximum at 1%. This error then is folded into the calculation of ϕ and ϕ_s. Since the error is

at maximum 1% in one direction with the other direction a maximum of 0.3%, this error becomes negligible.

Beam position at HERMES is measured by several monitors placed close to the entry point of the lepton beam to the spectrometer. By following the previous argument about the size of errors in comparison to the way they are folded into the calculations and eventual extracted asymmetries, the errors in the beam offset can also be neglected. The only potential issue that has not been addressed is the influence of the beam slope and spectrometer slope on the extracted asymmetries. This has been studied previously and been found not to affect, to any great degree, the extracted asymmetries. The study, in which the asymmetries for 2002-2004 were extracted with a data set corrected for slope misalignments, found that a suitable systematic error for this effect was 2%. As there is no reason to believe that there would be a significant difference for the 2005 data, this error is also used in this analysis. The precise value is given in tables 5.2 and 5.3.

Calibration of the Calorimeter

There is currently some consternation within the HERMES collaboration as to the accuracy of the calorimeter calibration, specifically, the reconstruction of the energy of photons impingent on the calorimeter. There have been several indications that photon energy is calculated with a 1% decrease of the photon energy reconstruction code used at HERMES. The most serious piece of evidence for this is the missing mass peak generated by Monte Carlo simulations — it is shifted by 1% in the negative direction with respect to the real data.

This could affect the TTSA calibrations by influencing the event selection arising from the cut on missing mass. All other variables involved in the analysis are independent of the photon energy since, in order to avoid relying on the poor energy resolution of the calorimeter, the Mandelstam variable t is calculated using the assumption that the missing mass is that of a proton and the binning variable used is actually the *constrained* Mandelstam variable, or t_c. The missing mass reconstruction however, relies upon the photon energy and is used to make the cut on the event selection so that a poor calibration of the calorimeter allows a significant background level to contaminate the event sample.

In order to check the possible effects of a 1% calorimeter miscalibration, a Monte Carlo study of the 2002-2004 data set was performed and the conclusion reached that such a calibration would have a negligible affect on the TTSA amplitudes

[Ye06]. An additional study was done by correcting the raw data by the suggested technique in reference [Van06] for the 2005 data set. Future plans in HERMES involve a recalibration of the calorimeter with the intention to reduce the potential for error to a minimum, and there are some questions about whether the correction in reference [Van06] is correct. The suggested correction of reducing the photon energy by 3% (relative) and correcting the z-position of the the photon within the calorimeter was performed on the 2005 data set for this publication. This correction results in asymmetry results of $A_{sc}^{\sin(\phi-\phi_s)\cos\phi} = 0.072$ and $A_{cs}^{\cos(\phi-\phi_s)\sin\phi} = 0.000$.

The large deviations from the results extracted using the normal HERMES method of determining photon energy in the calorimeter could arise from the fact that the correction was originally designed to be applied to a π^0 detection analysis, in which two photons, rather than one, are impingent upon the calorimeter. The deviations are so large that they are suspect, especially when compared against the results that come from the Monte Carlo study, and there have been indications [AV] in the HERMES collaboration that the calorimeter correction suggested in [Van06] is not suitable for a DVCS analysis. Due to these factors, a systematic error based upon the results from the Monte Carlo study in [Ye06] is applied to the data, which remains uncorrected for any negative influence from the calorimeter. The systematic error can be found in tables 5.2 and 5.3.

Detection Efficiency

Efficiencies can greatly affect a measurement of an asymmetry. If there are different detection efficiencies for events with different polarisation states of the target then an uncorrected inefficiency can introduce a false asymmetry into the measurements and render the entire exercise worthless.

The HERMES target flips spin orientation every 90 s and this period is sufficiently short that time-dependent efficiencies will be well distributed throughout the data set with no dependence on the spin state. Therefore the efficiencies that need to be considered are the efficiency of the tracking system in reconstructing the tracks of scattered leptons and produced photons and the efficiency of the trigger system in detecting DIS events.

The tracking system at HERMES has been examined with the ACE program. Tracking efficiency has been estimated for each individual subdetector, each tracking system (front and rear) and each half of the spectrometer, in addition to the overall global tracking efficiency. For the years 2002-05 this was found to be $\approx 99.8\%$.

The spectrometer trigger used for DIS analyses is trigger 21, which requires that the hodoscopes H0, H1 and H2 fire in conjunction with the calorimeter at the time of a HERA bunch. In order that the efficiency ϵ of a system is examined it is sufficient to assume that the bunch structure of the beam is rigid and examine the rate at which three of the detectors fire without the fourth detector firing simultaneously. This leads to the equation

$$\epsilon_{tr21} = \epsilon_{H0} \cdot \epsilon_{H1} \cdot \epsilon_{H2} \cdot \epsilon_{calo} \tag{5.22}$$

where, if N represents the number of event seen by that subsystem, the efficiency of the calorimeter can be written as

$$\epsilon_{calo} = \frac{N_{tr21}}{N_{H0+H1+H2}}. \tag{5.23}$$

Efficiencies can be functions of the scattering angle $\theta_x = \theta\cos\phi$ and $\theta_y = \theta\sin\phi$ and the momentum of the scattered lepton p_e. Previous studies [Ye06] have shown that the efficiencies of the calorimeter and the two hodoscopes H1 and H2 have little dependence on lepton momentum and only a 0.3% angular dependence.

The same studies showed that despite an angular dependence twice that of H1 and H2, the inefficiencies of H0 do not affect the extracted asymmetries for the 2002-2004 data set and are not accounted for in the systematic error in those measurements. In order that the same assumptions may apply for the 2005 data set, any runs that are marked as having a problem with the hodoscopes are discarded prior to the data quality cuts described in section 5.1.2. Therefore no systematic error was assigned to account for possible effects from detection efficiency effects.

Acceptance/Smearing Effects

A detailed Monte Carlo study [Ye06] has been performed on the smearing/acceptance effects present for TTSA amplitudes extracted from HERMES data [Ye06]. The gmc_dvcs generator described in [Kra05] was used to generate BH+DVCS events in the HERMES acceptance and in a 4π acceptance. The TTSA amplitudes were extracted for each generated data set. The conclusion was reached that comparing HERMES TTSA results binned in a kinematic variable, e.g. Q^2, against theoretical predictions would be difficult, as the HERMES acceptance for those variables has a non-negligible affect on the amplitudes. However, if the results from HERMES data

are averaged across all kinematics, as is the case for those presented in figure 5.6, then these results have only a small deviation from those that could be expected from TTSA amplitude extraction from a 4π data set. The same percentage errors as evidenced for the 2002-2004 data were applied as acceptance-derived errors for the 2005 data set.

The same study found that although it is possible to partially correct for smearing effects due to detector resolution, such a correction is imperfect and rather than apply a correction for smearing, a systematic error was assigned for the effect based on the difference between extracted results with and without smearing effects applied. The same systematic error found for 2002-2004 is assigned to the current data set, shown in tables 5.2 and 5.3.

Background Contributions

The background contributions from semi-inclusive and exclusive π^0 production have been studied in a Monte Carlo simulation [Ye06]. The outcome of the study was that limited statistics make it impossible to obtain a result on the size of any asymmetry arising from background contributions from such events. The magnitude of the contribution from these events however, is very small, being 0.8% and 0.4% respectively, although the amplitudes of any asymmetries from these contributions is unknown. In order to estimate the maximum contribution of this background to the TTSA amplitudes, the asymmetry amplitudes that may arise from background contributions have been set at 1, and assigned as systematic error, which is applied to amplitudes that remain uncorrected for background effects. See tables 5.2 and 5.3.

5.4.1 Total Systematic Errors

Tables 5.2 and 5.3 show the systematic errors in the various kinematic bins in which amplitudes are extracted. The "overall" value is calculated without taking into account the acceptance effect, as explained in ref [Ye06]. The final results of the 2005 analysis, complete with systematic and statistical errors for each bin, are presented in table 5.4.

This chapter has presented information on a way to access Transverse Target Spin Asymmetry (TTSA) amplitudes in Deeply Virtual Compton Scattering (DVCS) at HERMES, a subject first raised in chapter 2. The necessary cuts to data sets from

	Bin Range	δ_{targpol}	δ_{fit}	δ_{misalign}	δ_{calo}	δ_{smear}	δ_{bground}	δ_{overall}	δ_{acc}
$-t_c$ (GeV^2)	0.000–0.006	0.010	0.002	0.020	0.014	0.016	0.035	0.047	0.033
	0.060–0.140	0.007	0.006	0.009	0.010	0.010	0.013	0.023	0.012
	0.140–0.300	0.016	0.013	0.017	0.017	0.018	0.021	0.042	0.016
	0.300–0.700	0.032	0.001	0.004	0.037	0.036	0.101	0.062	0.166
x_B	0.030–0.070	0.007	0.026	0.006	0.027	0.031	0.011	0.051	0.065
	0.070–0.100	0.001	0.012	0.005	0.013	0.001	0.001	0.018	0.011
	0.100–0.150	0.012	0.002	0.011	0.028	0.018	0.011	0.039	0.005
	0.150–0.300	0.003	0.090	0.002	0.002	0.024	0.045	0.104	0.011
Q^2 (MeV^2)	1.000–1.500	0.009	0.000	0.013	0.002	0.011	0.015	0.024	0.017
	1.500–2.300	0.009	0.007	0.015	0.004	0.008	0.016	0.026	0.039
	2.300–3.500	0.016	0.012	0.019	0.029	0.021	0.021	0.050	0.025
	3.500–10.00	0.004	0.011	0.008	0.004	0.010	0.010	0.020	0.002
Overall		0.009	0.005	0.002	0.003	0.011	0.014	0.021	0.0173

Table 5.2: Systematic errors in A_{sc} for 2005 data.

	Bin Range	δ_{targpol}	δ_{fit}	δ_{misalign}	δ_{calo}	δ_{smear}	δ_{bground}	δ_{overall}	δ_{acc}
$-t_c$ (GeV^2)	0.000–0.006	0.007	0.010	0.014	0.023	0.011	0.026	0.041	0.043
	0.060–0.140	0.001	0.003	0.001	0.026	0.001	0.002	0.026	0.003
	0.140–0.300	0.012	0.005	0.013	0.014	0.014	0.016	0.031	0.040
	0.300–0.700	0.003	0.005	0.003	0.017	0.003	0.009	0.021	0.041
x_B	0.030–0.070	0.007	0.008	0.032	0.023	0.006	0.096	0.042	0.080
	0.070–0.100	0.000	0.001	0.004	0.003	0.001	0.001	0.005	0.000
	0.100–0.150	0.006	0.021	0.006	0.007	0.003	0.006	0.025	0.003
	0.150–0.300	0.003	0.032	0.001	0.007	0.001	0.011	0.035	0.005
Q^2 (MeV^2)	1.000–1.500	0.004	0.001	0.027	0.030	0.018	0.030	0.054	0.002
	1.500–2.300	0.001	0.019	0.004	0.008	0.009	0.008	0.024	0.001
	2.300–3.500	0.001	0.001	0.000	0.014	0.000	0.001	0.014	0.000
	3.500–10.00	0.006	0.004	0.003	0.007	0.000	0.007	0.013	0.007
Overall		0.000	0.012	0.000	0.004	0.001	0.000	0.013	0.000

Table 5.3: Systematic errors in A_{cs} for 2005 data.

	Bin Range	$<Q^2>$	$<t_c>$	$<x_b>$	A_{sc}	δ_{stat}	δ_{syst}	A_{cs}	δ_{stat}	δ_{syst}
Q^2 (GeV^2)	(1.0–1.5)	1.24	0.09	0.06	0.094	0.104	0.047	-0.044	0.104	0.041
	(1.5–2.3)	1.86	0.11	0.08	0.102	0.089	0.023	-0.012	0.091	0.026
	(2.3–3.5)	2.83	0.13	0.11	0.172	0.094	0.042	-0.007	0.094	0.031
	(3.5–10.0)	4.87	0.20	0.17	0.039	0.095	0.062	0.066	0.097	0.021
t_c (GeV^2)	(0.00–0.06)	1.95	0.03	0.08	0.109	0.080	0.051	0.080	0.082	0.042
	(0.06–0.14)	2.51	0.10	0.10	-0.075	0.085	0.018	0.010	0.089	0.005
	(0.14–0.30)	2.83	0.20	0.11	0.169	0.095	0.039	-0.133	0.096	0.025
	(0.30–0.70)	2.40	0.42	0.12	0.345	0.145	0.104	0.032	0.132	0.035
x_b	(0.03–0.07)	1.45	0.11	0.05	0.192	0.087	0.024	-0.080	0.085	0.054
	(0.07–0.10)	2.16	0.11	0.08	0.029	0.091	0.026	0.004	0.095	0.024
	(0.10–0.15)	3.13	0.13	0.12	0.059	0.094	0.050	0.065	0.097	0.014
	(0.15–0.30)	5.05	0.20	0.20	0.126	0.111	0.020	0.035	0.116	0.013
Overall		2.44	0.12	0.09	0.097	0.047	0.021	0.001	0.047	0.013

Table 5.4: Table of Final Results for 2005 data.

2002, 2003, 2004 and 2005 have been discussed, where 2002-2004 were taken with a positron beam and 2005 was taken with an electron beam. The amplitudes show the potential to differentiate between values of J_u in the model discussed in the next chapter. The amplitudes from the two sets have been combined in order to look at the potential magnitude of any asymmetry resulting from the pure DVCS term. Any such asymmetry would necessarily be very small, and is consistent with zero at the current level of statistical precision. A study of the systematic errors that affect the 2005 data set and the extraction of asymmetries therefrom has been performed, and the results presented in tables 5.2 and 5.3. The final result for the 2005 data set asymmetries can be seen in table 5.4 and figure 5.6. The next chapter details the model used for comparison with experimental data, and explains the implications for the calculation of a value for the total angular momentum of quarks in the nucleon using the HERMES data as input to that model.

Chapter 6

Interpretation

The connection between the TTSA amplitude result presented in the previous chapter and the spin puzzle discussed in the introduction to this thesis has not yet been stated explicitly. This chapter will set out a way to link the two through use of the Vanderhaeghen, Guidal, Guichon model and programme for calculating experimental observables. A constraint upon the total angular momentum of the quarks in the nucleon is derived through comparison of asymmetry values calculated by this programme and the asymmetry value measured at HERMES. The implications for the spin puzzle from this constraint are then discussed followed by a description of a physical interpretation of the results.

In order to model GPDs H and E, the parametrisation discussed in [GPV01] uses the Ji "sum rule" (eqn (2.17)) to provide a limiting case for development of the model. The following two sections supply details of the parameterisation used to model the GPDs H and E.

6.1 A Parameterisation of the Generalised Parton Distribution H

In an earlier section (Chapter 2) one of the relationships between GPDs and regular form factors was written as

$$H^q(x,\xi,t) = H^q(x,\xi) \cdot F_1^q(t) \tag{6.1}$$

under the assumption of a factorised t-dependence. This then leads the t-independent

part of the GPD to be written as [GPV01]:

$$H^q(x,\xi) = H^q_{DD}(x,\xi) + \theta(\xi - |x|)\, D^q\left(\frac{x}{\xi}\right) \tag{6.2}$$

The second term in this equation, colloquially known as the "D-term" is the subject of some debate within the GPD community, but will not be covered here in detail. For a more thorough discussion, see [Wak07]. The H^q_{DD} term is a part which can be obtained from the double distribution $F^q(\beta,\alpha)$ [MR00], [Rad99], [PW99]:

$$H^q_{DD} = \int_{-1}^{1} d\beta \int_{-1+|\beta|}^{1-|\beta|} d\alpha\, \delta(x - \beta - \alpha\xi)\, F_q(\beta,\alpha) \tag{6.3}$$

However, this factorised t-dependence is directly contradicted by experimental evidence gleaned from studies of elastic processes. These indicate that the t-dependence of the cross section is not easily disentangled from the dependence on the photon-nucleon invariant mass. The experimental evidence is further supported by more recent QCD calculations performed on the lattice and other phenomenological considerations. So, rather than using this factorised t-dependence in the model calculations, the t-dependence of the GPD is not explicitly removed, but instead retained. The assumption is then made that the $F_q(\beta,\alpha)$ term above can be written as

$$F_q(\alpha,\beta,t) = F_q(\alpha,\beta)\,\frac{1}{|\beta|^{\alpha' t}} \tag{6.4}$$

This assumption is known as the Regge-type t-dependence. Since the simple factorised term is known to be disfavoured [GHH$^+$06], [Bur04], this assumption will be held as true for the rest of this work.

Under either the Regge or the factorised t-dependence, we can proceed to write $F_q(\alpha,\beta)$ in such a fashion as to give it a dependence on the ordinary quark parton distribution function (PDF), with an additional dependence on a profile function $h(\alpha,\beta)$ that contains a free parameter b that controls the dependence of the GPD on ξ [MR00]:

$$F^q(\alpha,\beta) = h(\alpha,\beta)\, q(\beta) \tag{6.5}$$

with

$$h\left(\alpha,\beta\right)=\frac{\Gamma(2b+2)}{2^{2b+1}\Gamma^{2}(b+1)}\frac{[(1-|\beta|)^{2}-\alpha^{2}]^{b}}{(1-|\beta|)^{2b+1}} \tag{6.6}$$

For $\beta > 0$, $q\left(\beta\right)$ is the ordinary quark PDF and, for $\beta < 0$, it represents the antiquark PDF. The b parameters in the above equation are completely unknown, both for valence quarks (b_{val}) and sea quarks b_{sea}. The rest of this work will continue under that the assumption $b_{val} = 1$ and $b_{sea} = 9$.

6.2 A Parametrisation of the GPD E

The following is a summary of pages 56-62 found in reference [GPV01].

The parameterisation of E is more complicated than that of H as there is no x-dependence in the forward limit. It is the evaluation of GPD E in which we can find sensitivity to J^q however. First assume that the t-dependence of E can be factorised and consider only the analogous equation to equation 6.2.

$$E^{q}(x,\xi,t)=E^{q}_{DD}(x,\xi,t)-\theta(\xi-|x|)\frac{1}{N_f}D\Big(\frac{x}{\xi},t\Big) \tag{6.7}$$

which reduces to $E^q_{DD}(x, \xi = 0, t = 0)$ in the forward limit where $(\xi = 0, t = 0)$. Taking eqn 2.14 at this limit and realising that in this limit the Pauli Form Factor F_2^h reduces to the anomalous magnetic moment of the hadron h, we get that:

$$\int_{-1}^{1}dxE^{q}_{DD}(x)=\kappa^{q} \tag{6.8}$$

and that, since $\kappa^u = 2\kappa^p + \kappa^n = 1.673$ and $\kappa^d = 2\kappa^n + \kappa^u = -2.033$ under the assumption of isospin symmetry, a real-valued normalisation constraint on the function $E_{DD}(x)$ can be determined. As an initial guess to the form of this function, the valence quark distributions for each flavour are posited:

$$\begin{aligned} E^{u}_{DD} &= \frac{1}{2}u_{val}(x)\kappa^{u} \\ E^{d}_{DD} &= d_{val}(x)\kappa^{d} \\ E^{s}_{DD} &= 0 \end{aligned} \tag{6.9}$$

Equation group (6.9) is taken to be the set of valence parameterisations of E and all that is left to determine is sea quark contribution. Chiral quark soliton model calculations show that this sea quark component is symmetric in x and narrowly peaked, so a δ-function is assumed. This leads to the relations

$$\begin{aligned} E^u_{DD} &= A^u u_{val}(x) + B^u \delta(x) \\ E^d_{DD} &= A^d d_{val}(x) + B^d \delta(x) \\ E^s_{DD} &= 0 \end{aligned} \tag{6.10}$$

where A_q and B_q are co-efficients determined by a combination of the total angular momentum of all (i.e. valence and sea) quarks of flavour q, the fraction of the proton's momentum carried by all quarks of flavour q and the fraction of the proton's momentum carried by valence quarks of flavour q:

$$A_q = \frac{2J_q - M^{(2)}_q}{M^{(2)}_{q_{val}}}, \tag{6.11}$$

$$B_u = 2\left[\frac{1}{2}\kappa_u - \frac{2J_u - M^{(2)}_u}{M^{(2)}_{u_{val}}}\right] \tag{6.12}$$

$$B_d = \kappa_d - \frac{2J_d - M^{(2)}_d}{M^{(2)}_{d_{val}}} \tag{6.13}$$

where $M^{(2)}_{q_{val}}$ is the valence quark contribution of quark flavour q to the proton's angular momentum and $M^{(2)}_q$ is the total quark contribution of quark flavour q to the same,

$$M^{(2)}_{q_{val}} = \int_0^1 x q_{val}(x) dx, \tag{6.14}$$

$$M^{(2)}_q = \int_0^1 x[q_{val}(x) + 2\ \bar{q}\ (x)]dx. \tag{6.15}$$

In this way, the values of J_q enter into the model as fit parameters and can be used as inputs in order to calculate observable such as azimuthally asymmetric photon yields. The variation of these calculated observables from measured values can then be used to recover information on J_q from the measured observables.

6.3 A Model-based Code for the Calculation of Observable Asymmetries in DVCS

A computational program capable of calculating observables in DVCS for the HERMES kinematic regime that utilises the parameterisation of GPDs described in the previous two subsections has been made available to the HERMES collaboration [VDH]. This program has been used to generate the value of the leading TTSA observable, A_{UT}^{sc} at HERMES kinematics for various values of J_u and J_d. In the following sections this model-based result is compared to the measured asymmetry values. This comparison derives a constraint on the total angular momentum of up- and down-quarks in the proton.

6.3.1 Comparison with Data

The simulation code ("VGG-code") from ref. [VDH] calculates a doubly polarised cross section in the HERMES kinematic regime, with values of J_u and J_d as free parameters. The value described in chapter 5 as A_{UT}^{sc} can be calculated from this cross section. This calculated value can then be compared to the value measured at the HERMES experiment. The other asymmetry measured in the previous section, A_{UT}^{cs} is not considered here as it has been shown already in chapter 5 to have little sensitivity to values of J_q.

All calculated cross sections and asymmetries mentioned in this chapter are produced for a process where the incoming lepton to the DVCS process is an electron. The cross section and asymmetries arising from it are expected to have little variance depending upon the beam charge. The most significant non-charge symmetric term in the cross-section is the $|\tau_{DVCS}|^2$ term from equation (2.18) but the contribution of this term is expected to be less than 10% and so is considered negligible when compared to other potential errors introduced by the model (see section 6.3.2).

A set of cross sections corresponding to an array of J_u/J_d values were produced. This array of J_u/J_d values corresponds to a grid described by $0 \leq J_u \leq 1$ and $-1 \leq J_d \leq 1$ with granularity 0.2. This level of granularity was chosen in order to minimise computational time, since even using a distributed computing network with many available processors, each J_u/J_d cross section set took ≈ 1 week to calculate. Since the grid granularity scales quadratically, an increase of two in grid resolution would mean that the calculation would take approximately one month.

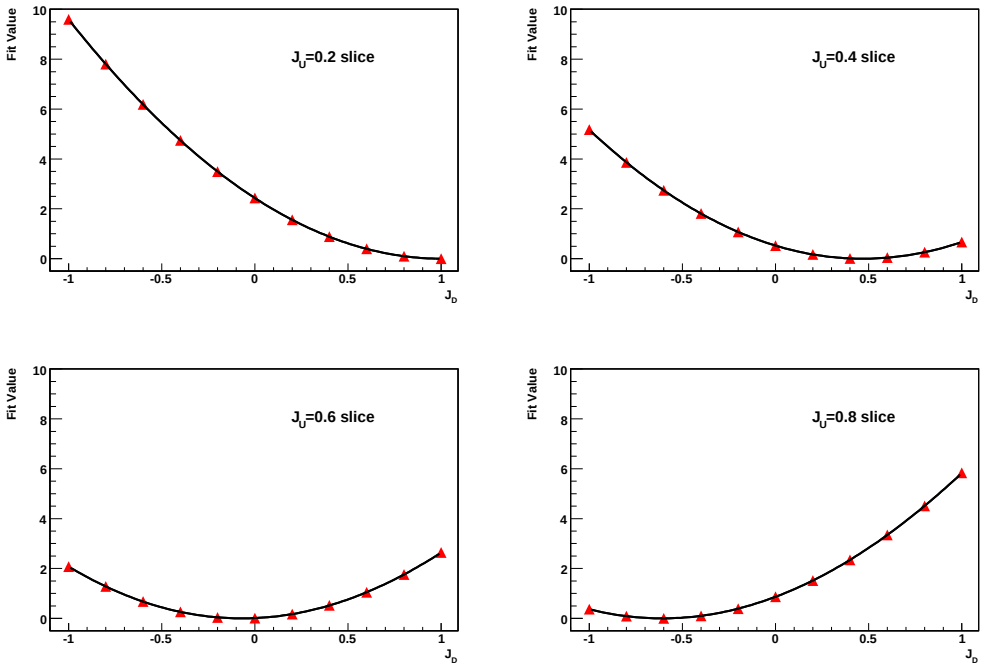

Figure 6.1: The surface represented in the previous figure for slices through various J_u values. It can be seen that the fit is qualitatively accurate.

The asymmetry value A_{UT}^{sc} was calculated for each J_u/J_d pair, producing points on an asymmetry value surface in J_u/J_d-space. These points were interpolated by fitting a 5-th order polynomial to them as in figure 6.2, slices of which can be seen in 6.1. In order to maximise the statistical significance of the experimentally measured result, the asymmetry value from the 2002-04 data set measured in section 5.3 was combined quadratically with the result obtained from the 2005 data set as:

$$\begin{aligned} TTSA_{overall} &= \sqrt{\frac{1}{2}(TTSA_{02-04}^2 + TTSA_{05}^2)} \\ &= \sqrt{0.5 * ((-0.146)^2 + (0.097)^2)} \\ &= 0.124 \end{aligned} \tag{6.16}$$

The distance from this value of A_{UT}^{sc} to the surface extracted from simulated data was then calculated with the χ^2 method shown in eqn (6.17). The acceptance effect was included in this calculation as the programme calculated observables in 4π, in contrast to the final systematic errors presented in chapter 5 which were presented

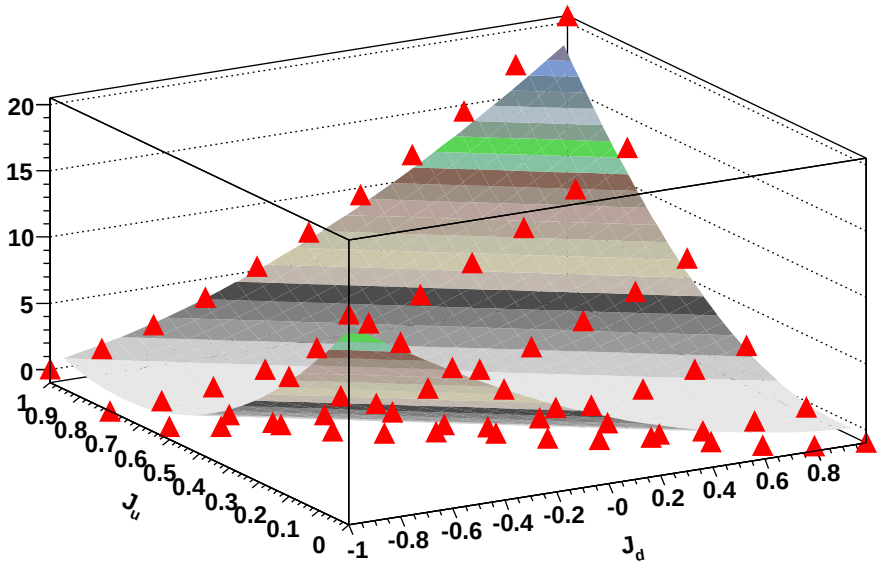

Figure 6.2: The VGG model output for various pairs of J_u and J_d values is calculated (red triangles) and is fit with a fifth-order two dimensional polynomial—J_u is on the y-axis, J_d is on the x-axis and the difference between the model-asymmetry value and the value calculated from experimental data appears on the y-axis. The surface shown is for impact parameters $b_{val} = 1$ and $b_{sea} = 9$.

without a systematic error due to the acceptance affect.

$$\chi^2(J_u, J_d) = \frac{\left[A_{UT}^{sc}\,|_{exp} - A_{UT}^{sc}\,|_{VGG}\,(J_u, J_d)\right]^2}{\sigma A_{stat}^2 + \sigma A_{sys}^2 + \sigma A_{acc}^2} \tag{6.17}$$

In equation (6.17) $A_{UT}^{sc}\,|_{exp}$ refers to the experimental result from eqn (6.16), $A_{UT}^{sc}\,|_{VGG}$ (J_u, J_d) refers to the surface extracted from simulated data and σA_{stat}^2, σA_{sys}^2 and σA_{acc}^2 refer to the statistical, systematic and acceptance errors respectively.

This calculation results in a surface χ_{dist}^2 in J_u/J_d-space describing the distance from the measured asymmetry result from data taken at HERMES to the asymmetries calculated from the simulated cross sections.

The minimum of this surface is then found, and all points on the surface S_p fulfilling the constraint S_p <min$(\chi_{dist}^2 + 1)$ are projected onto an area in the J_u/J_d-plane. This area then corresponds to a standard one σ model-dependent constraint on the value of $J_u + J_d$.

6.3.2 The Constraint Result

The constraint result can be seen in figure 6.3. The specific inputs to the VGG-code can be found in appendix A. The equation describing the band is given as:

$$J_u + \frac{J_d}{2.7} = 0.42 \pm 0.20 \tag{6.18}$$

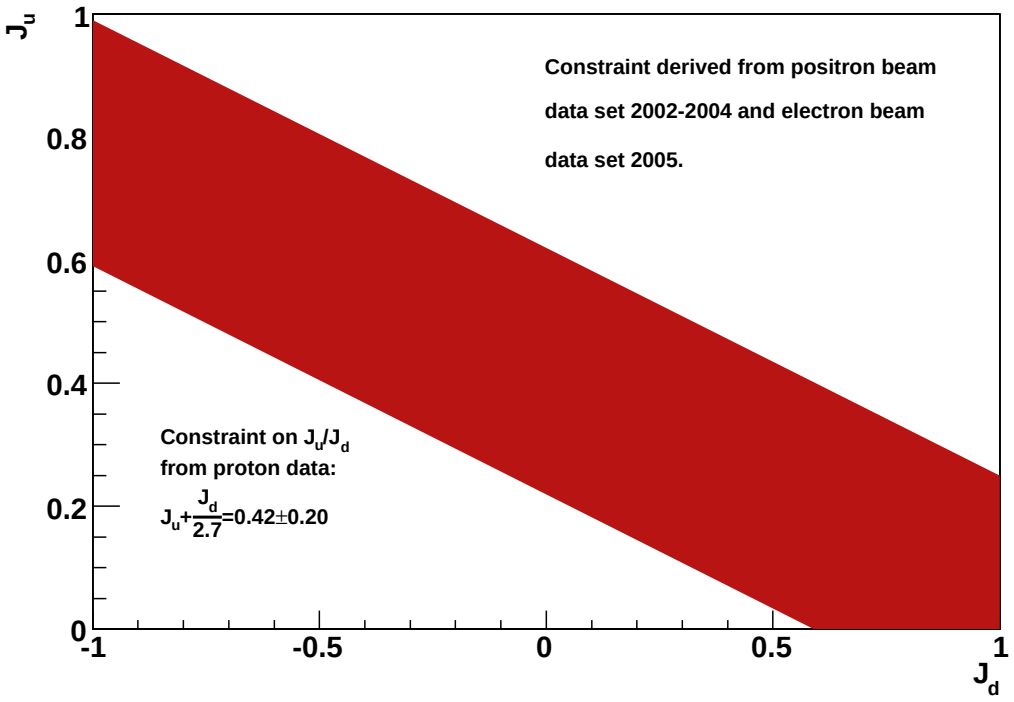

Figure 6.3: A one σ constraint on J_u and J_d for quarks in the proton dependent upon the VGG-model. The VGG-code values are determined with impact parameters $b_{val} = 1$ and $b_{sea} = 9$, in contrast to reference [Ye06]. A mathematical description of the area is given as equation (6.18).

The constraint is subject to an unknown systematic error that is a result of the model-dependence. The model is known not to reproduce world data correctly [ea06] and it is based upon Ji's sum rule which is valid for $t = 0$, whereas experimental data is necessarily at $|t| > 0$. There has also been shown a dependence on the unknown b profile parameter [Ye06] although is expected to be smaller than the other potential errors. Since the systematic error is difficult to quantify it is not propagated throughout the rest of this chapter. It is expected to be large, however.

6.4 Comparison with JLab Data

Hall A at Jefferson Lab in Virginia recently showed results [Maz07] obtained via the beam spin asymmetry on unpolarised deuterium to give a constraint on J_u and J_d on the neutron. This result on the neutron is produced from a beam spin asymmetry on the deuteron acting as a neutron target. The neutron BSA is another observable that is expected to be sensitive to GPD E. Under the assumption of isospin symmetry the constraint on the neutron can be related to the constraint on the proton by:

$$J_d + \frac{J_u}{5} = 0.18 \pm 0.14 \tag{6.19}$$

The area described in eqn (6.19) is plotted in figure 6.4, in addition to two constraints that are the result of lattice calculations made by the QCDSF collaboration and the LHP and MIL collaborations. The two theoretical results correspond to the intersection of the constraints on proton and neutron which is shown in blue.

Solving the equations for the proton and neutron simultaneously the result $J_u = 0.38$ and $J_d = 0.10$ is achieved. This indicates the centre of the blue region in figure 6.4. The blue area is dominated by an unquantified systematic error that arises from imperfections in the VGG-code cross-section calculation. However, it should be of interest to note that the result lies in a similar region to that of the lattice calculations, which are also subject to unquantified model-dependent systematic errors that arise for instance from neglection of Δ degrees of freedom and higher-order terms in Chiral Perturbation Theory.

6.5 A Wider Look at the Implications for a Constraint on J_u/J_d

In the following section, no attempt at error propagation is made. Whilst the constraints shown in figure 6.4 all lie in the same region in the J_u/J_d-plane, all are subject to unknown systematic errors. Since any error analysis would necessarily be vague, the centre is the blue region is taken as indicative of a possible J_u/J_d value pair, i.e. figure 6.4 is taken as giving an approximate value of

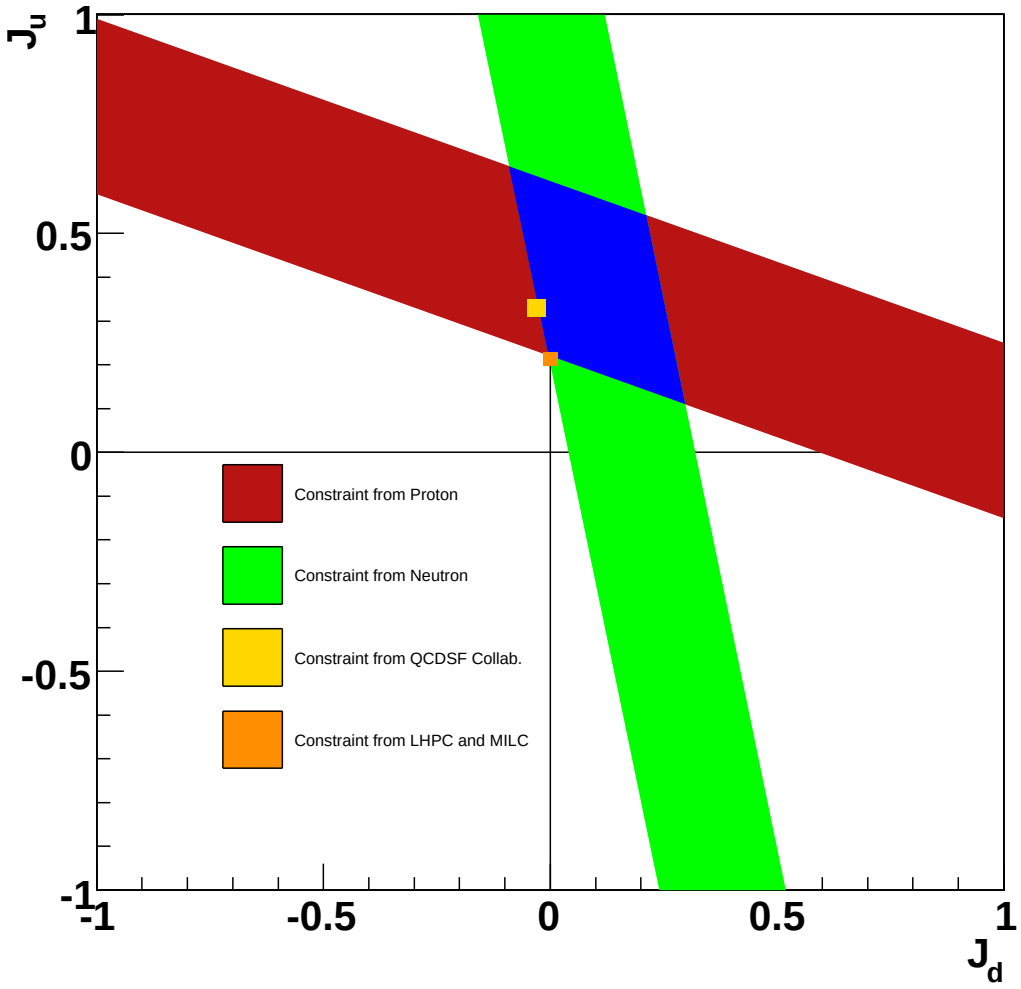

Figure 6.4: A set of VGG-model based constraints on J_u/J_d from the HERMES measurement on the proton (red band) and the JLab measurement on the neutron (green band) [Maz07]. Also given are QCDSF collaboration lattice calculation results (yellow rectangle) [Sch07] and LHPC and MILC lattice calculations (orange square) results [ea07].

$$\begin{aligned} J_u &= 0.38 \\ J_d &= 0.10 \end{aligned} \tag{6.20}$$

6.5.1 Interpretation of the Spin Equation in terms of Recent HERMES and JLab Results

In chapter 1 we saw equation (1.1), restated here:

$$\begin{aligned} \frac{1}{2} &= J_Q + J_G \\ &= \frac{1}{2}\Delta\Sigma + L_Q + \Delta G + L_G \end{aligned}$$

The Quark-Gluon Balance of Total Angular Momentum

Under the assumption that we can neglect any contribution to the spin of the proton that arises from the strange quark, we can write

$$J_Q = J_u + J_d \tag{6.21}$$

this being the case then we can immediately substitute in the result from equation (6.20):

$$J_Q = J_u + J_d = 0.38 + 0.10 = 0.48. \tag{6.22}$$

which, when substituted into the first line of equation (1.1) yields:

$$\begin{aligned} \frac{1}{2} &= J_Q + J_G \\ \Rightarrow 0.5 &= 0.48 + J_G \\ \Rightarrow J_G &= 0.02. \end{aligned} \tag{6.23}$$

This result on J_G directly contradicts a result published in 1997 by Ji and Balitsky [BJ97] where a value of $J_G = 0.35 \pm 0.13$ for a measurement scale of $\mu = 1\ GeV^2$. The calculation used in this paper assumes vector meson dominance in higher dimensions, which at the time of publishing was unknown. Nevertheless, the difference between

the value of J_G given in this paper and the value calculated in (6.23) is so large that it is indicative of a clear disagreement.

Angular Momentum of Quark Flavours

From equation (1.1) one can write

$$J_Q = \frac{1}{2}\Delta\Sigma + L_Q. \tag{6.24}$$

When this equation is combined with the result from this thesis on J_Q and the HERMES measurement of $\Delta\Sigma$ [A$^+$07b], a value for L_Q can be obtained:

$$\begin{aligned} 0.48 &= 0.5 \times 0.33 + L_Q \\ \Rightarrow L_Q &= 0.32 \end{aligned} \tag{6.25}$$

It is possible to go further and check this against the results $\Delta u = 0.42$ and $\Delta d = -0.21$ from the HERMES inclusive analysis [A$^+$05b]:

$$\begin{aligned} L_d &= J_d - \Delta d = 0.10 - (-0.21) = 0.31 \\ L_u &= J_u - \Delta u = 0.38 - (0.42) = -0.04 \\ \Rightarrow L_Q &= L_u + L_d = 0.31 + (-0.04) = 0.27 \end{aligned} \tag{6.26}$$

Despite a small discrepancy in the values of L_Q from equations (6.25) and (6.26), it is clear to see that both predict a non-trivial value of $L_Q \approx 0.3$ – a value that would make L_Q a more significant contributor to nucleonic spin than quark helicity or gluon total angular momentum.

The values written in equation (6.26) for L_u and L_d directly contradict those shown in [Sch07]. However, under the assumption that strange quark contributions can be neglected, the values shown in [Sch07] do not provide an explanation for how the helicity contribution ($\frac{1}{2}\Delta\Sigma \approx 0.15$) and the orbital angular momentum ($L_Q \approx 0$) sum to the total angular momentum arising from quarks ($J_Q \approx 0.3$). They derive their values based upon the formalism laid out in [CJ02].

6.5.2 Simple Physical Interpretation

The previous two sections give rise to a simple physical interpretation of nucleonic spin structure:

- Quark terms dominate the angular momentum of the nucleon.
- About $\frac{2}{3}$ of the quark contribution to the nucleon's spin comes from the orbital angular momentum, and that mostly from the down quark.

This then allows a naïve viewpoint of the structure of the nucleon to be formed. The most intuitive interpretation must be that of two, almost stationary up quarks in a "tightly-bound" core to the nucleon, orbited by a single fast-moving down quark. This is reflected in figure 6.5.

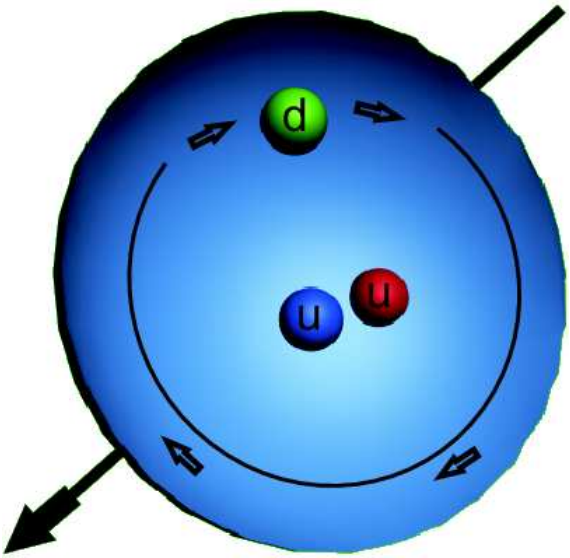

Figure 6.5: A naïve interpretation of the thesis result is that of a nucleon comprised of a diquark "up" core being orbited by a down quark. The angular momentum of the down quark is responsible for the difference between the nucleonic spin, and the contribution of the spins of the nucleonic constituents.

This is a picture which is quite consistent with a traditional quark-diquark model, one in which the two up quarks are bound into a single diquark state with a free down quark. However, this statement should not be taken too strongly – such a conclusion is drawn from asymmetry measurements which are non-precise and is reliant upon a GPD model, with all its inherent uncertainties and potential pit falls.

6.6 Future Work

It will be possible to improve the experimentally-obtained model-dependent constraints in this section by improving the underlying model. Unfortunately there are few models available that are capable of calculating experimental observables that can currently be measured. There are efforts underway [GT06] , however, to produce more predictive models and programs that can be used to interpret data in the field of GPDs, and at the HERMES kinematic regime in particular. In fact, shortly before publication, results from this model became available, and whilst there is not enough time to go into this new model here, it does supply one important caveat for the results previously mentioned.

This dual parametrisation method shows a model-dependent constraint which overlaps substantially with the constraint shown in figure 6.3. The constraint arising from the dual parametrisation method sits parallel to the VGG constraint, but at lower values of J_u. The overlap corresponds well with the region accorded to the MIL collaboration in figure 6.4. Taking this MIL region as indicative of values for J_u and J_d, we get

$$\begin{aligned} J_u &= 0.2 \\ J_d &= 0.0 \end{aligned} \tag{6.27}$$

Such an interpretation would allow agreement with the Ji and Balitsky paper cited above as [BJ97]. More comparisons with this Dual Parameterisation method will be seen in a paper to be released by HERMES in the near future.

Futher information from HERMES+Recoil (see figure 6.6) will also provide data of sufficiently high quality on BSA and BCA that these observables will become important and useful in understanding the structure of the GPD framework. The Beam Charge Asymmetry in particular has been shown to have sensitivity to the D-term [A$^+$07a] as alluded to briefly in eqn (6.2). Both asymmetries will provide important information about GPD H and allow a more thorough testing of the strengths and deficiencies of those models for GPDs that do exist.

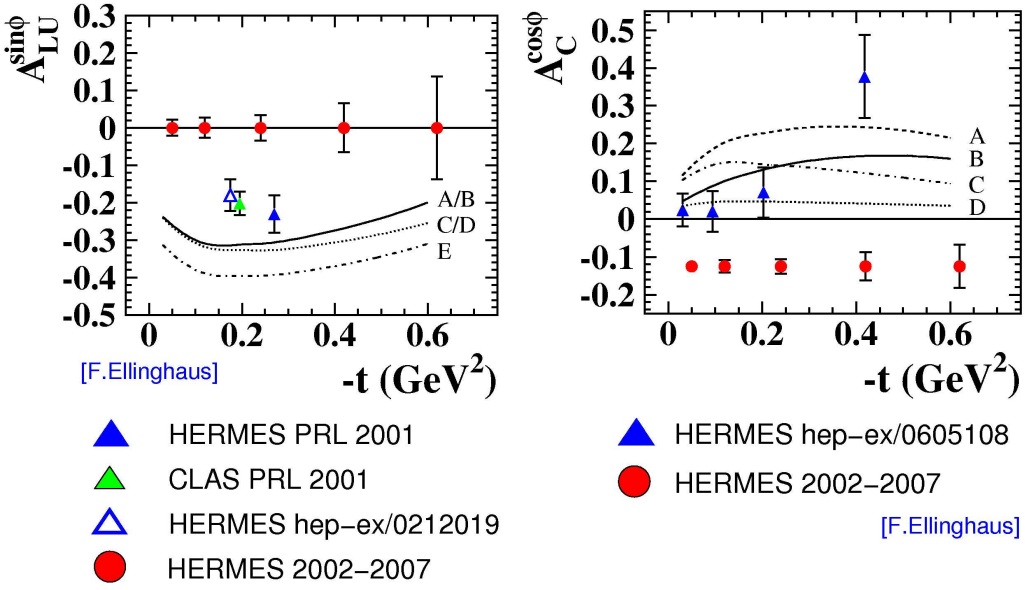

Figure 6.6: Projections of error magnitude from BSA (left) and BCA (right) DVCS measurements on the proton at HERMES as compared with published results.

Chapter 7

Conclusions and Outlook

Deeply Virtual Compton Scattering is the simplest process available to access Generalised Parton Distributions. The spin structure of the nucleon is encoded in the GPD framework, and so DVCS is inherently of interest to anyone wishing to study nucleon structure.

The goal of the HERMES collaboration is the study of nucleon structure. The collaboration's study of DVCS started in 1998, detecting only the scattered lepton and produced photon from the process and reconstructing the missing mass of the recoiling proton. In November 2005, HERMES was upgraded with a recoil detector in the target region that allows the detection of the recoiling proton and so also allows HERMES to completely measure the DVCS process for the first time.

The recoil detector has a number of subsystems, including an inner silicon detector placed in the beam pipe to detect low momenta protons, a scintillating fibre detector that allows detection of higher momentum protons, accurate tracking and particle identification and an outer photon detector that, in conjunction with the other two detectors, allows the subtraction of Δ-resonance final states from the data set, removing the main source of background to the DVCS interaction. There is also a 1 T surrounding magnet that bends particle tracks, facilitating PID and momentum reconstruction.

The silicon subdetector has been tested in various facilities. These test beam experiments have proved that it can be used to detect minimally ionising particles, that it has high efficiencies and that resolution is as expected. They have been used to identify damage to the detector, and as testing grounds for DAQ code. The functionality of the scintillating fibre detector has also been proven in test beams.

The Transverse Target Spin Asymmetry has been measured at HERMES for two data sets, 2002-2004 and 2005 with positron and electron beams respectively. In order to achieve this, data quality cuts have been made, an exclusive event sample identified and limitations in detector resolution have been overcome. The data has been combined to form a model-dependent constraint on the possible contribution of the total angular momentum of the up and down quarks to the nucleon spin.

A similar constraint from Hall A at JLab has been combined with the constraint derived in this thesis to obtain values for J_u and J_d. These have been combined into a value for J_Q and this has been used to speculate as to the solution to the spin puzzle. The hypothetical solution has been compared to several theory papers in the field.

Considerable improvements to knowledge of the structure of the nucleon will depend upon the GPD framework. Future results from the COMPASS collaboration at CERN and halls A and B at JLab can be expected to further improve knowledge of GPDs. The 12 GeV upgrade to Jefferson lab should allow the CLAS and Hall A collaborations to make DVCS measurements in a previously unexplored kinematic region (figure 7.1).

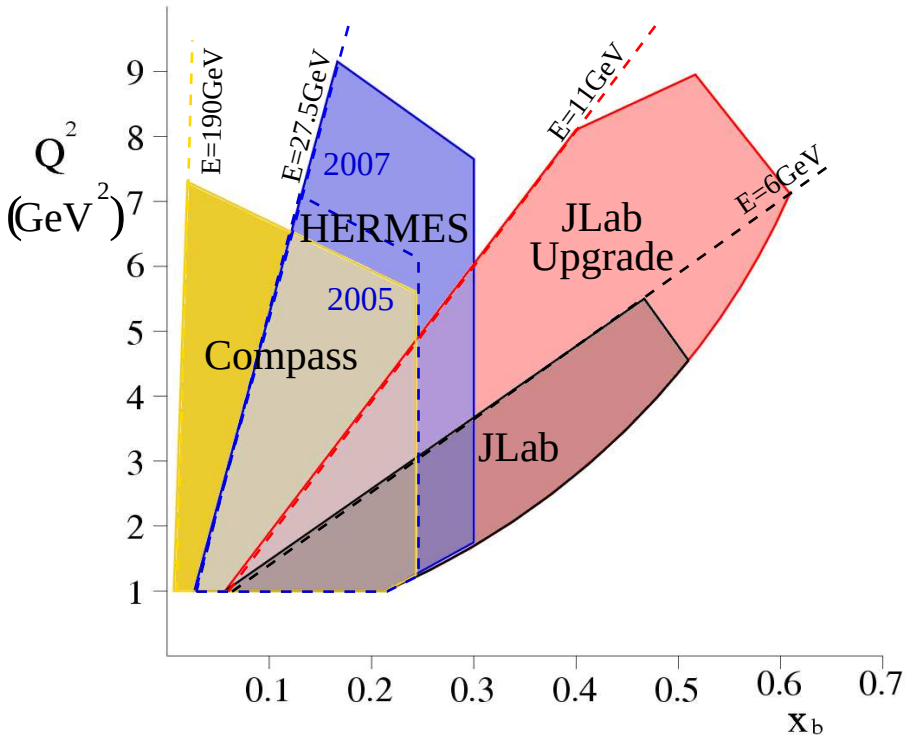

Figure 7.1: An outlook of the kinematic range that will be covered by DVCS experiments over the next 15 years. The upgrade of JLab to a 6 GeV beam will allow it to significantly increase its kinematic coverage.

Appendix A

Inputs to the VGG Code

The computational program written by Vanderhaeghen, Guichon and Guidal used to calculate TTSA amplitudes in section 6.5 was run with the following inputs:

- 4: DOUBLY POLARIZED cross sections for DVCS polarised electron, polarised target
- 3: Bethe-Heitler + DVCS contribution
- 1: proton
- 25: xi dependent parametrisation with MRST98 distribution
- 2: evolution with scale_sqr = Q_sqr
- Give the value for the power b in the profile function for the valence contribution to H: 1.0
- Give the value for the power b in the profile function for the sea contribution to H: 9
- 2: Regge inspired ansatz for the t-dependence
- 2: Do you Want to evaluate the D-term contribution to GPD H? (No)
- 2: How do you want to evaluate GPD E? (double distribution contribution + D-term)
- 2: Give the model for the double distribution part of the GPD E (valence quark + VM contribution)

- (0.0-1.0) Give the value of Ju (e.g. 0.3)?
- (-1.0-1.0) Give the value of Jd (e.g 0.2)?
- 1: Do you want to evaluate the pi0 pole contribution (i.e. SPD Etilde)? (yes)
- 2: Include twist-3 corrections for L photon in Wandzura-Wilczek approximation
- 1: calculate with xi' and put xi = xi' (virtual photon long momentum = -2 xi' P+)
- (1,2) Give the polarisation of the target proton? (x-plane AND $y-plane$)
- 1: Calculation for what LEPTON charge ? (negative)
- Give the value of beam energy in GeV (e.g. 27.) (27.56)
- Give the value of Q$\hat{2}$ in GeV$\hat{2}$ (e.g. 5.0) (2.44)
- Give the value of x_B (e.g. 0.3) (0.09)
- 3: Fixed out-of-plane angle (in deg) or phi-scan ?(scan in ϕ, fix in t)
- Give the value of -t (in GeV$\hat{2}$) (0.116)

More details about the MRST98 PDF can be found in reference [MRST98].

Appendix B

Quotations

I *really* like quotations, but I wanted to avoid putting a quotation at the start of each chapter. Instead, I have included a selection of quotations that, when I hear them, I think about the work I have performed for the relevant section. I very much hope that you find at least one new quotation here to enjoy.

Introduction

- "Begin at the beginning," said the king, gravely, "and go on until you reach the end. Then stop." — *L. Carroll*.
- Writing is an exploration. You start from nothing and learn as you go. — *E. L. Doctorow*.
- In the beginning the universe was created. This has made an awful lot of people angry and was widely regarded as a bad move. — *D. Adams*.

Generalised Parton Distributions and Deeply Virtual Compton Scattering

- There was so much to grok, and so little to grok from. — *R. Heinlein*.
- In DIS, Chuck Norris kills the proton. — *C. Vogel*.
- Pure as the driven slush. — *T. Bankhead*.

The HERMES Experiment

- Never worry about the theory as long as the machine does what it is supposed to do. — *R. Heinlein.*
- There is less to this than meets the eye. — *T. Bankhead.*
- The machine does not isolate man from the great problems of nature, but plunges him more deeply into them. — *A. de Saint-Exupery.*

The Recoil Detector

- We all make mistakes and when you've made enough you call it experience. — *The Supernaturals.*
- The cure for boredom is curiosity. There is no cure for curiosity. — *D. Parker.*
- We must wait. — *A. Borrisov.*

Transverse Target Spin Asymmetries in DVCS

- "So computers are the tools of the devil?" thought Newt. He had no trouble believing it. Computers had to be the tool of *somebody*, and all he knew for certain is that it wasn't him. — *N. Gaiman and T. Pratchett.*
- On two occasions I have been asked "Pray, Mr. Babbage, if you put into the machine the wrong figures. will the right answers come out?" I am not rightly able to apprehend the kind of confusion that could provide such a question. — *C. Babbage.*

Interpretation

- It's one of those irregularly declining words. I have an independent mind, you're eccentric, he's round the twist. — *B. Wooley*
- Where am I? What's that in there? Are those *my* feet? — *J. Hackett*
- Sure, that's nearly as mad as that thing you told me about the loaves and the fishes. — *D. MacGuire.*

Conclusions and Outlook

- At a physics talk, people applaud not in appreciation, but in relief. — *M. Murray.*

Bibliography

[A+88] J. Ashman et al. An investigation of the spin structure of the proton in deep-inelastic scattering of polarized muons. *Phys Lett B*, 206:364, 1988.

[A+89] J. Ashman et al. An investigation of the spin structure of the proton in deep-inelastic scattering of polarized muons on polarized protons. *Nucl. Phys.*, B328:1, 1989.

[A+98] K Ackerstaff et al. The hermes spectrometer. *NIM A*, 417:230, 1998.

[A+00a] A. Airapetian et al. Observation of a single-spin azimuthal asymmetry in semi-inclusive pion electro-production. *Phys. Rev. Lett.*, 84:4047–4051, 2000.

[A+00b] P. L. Anthony et al. Measurements of the q**2 dependence of the proton and neutron spin structure functions g1(p) and g1(n). *Phys. Lett.*, B493:19–28, 2000.

[A+01a] A. Airapetian et al. Measurement of the beam-spin azimuthal asymmetry associated with deeply-virtual compton scattering. *Phys. Rev. Lett.*, 87:182001, 2001.

[A+01b] A. Airapetian et al. Single-spin azimuthal asymmetries in electroproduction of neutral pions in semi-inclusive deep-inelastic scattering. *Phys. Rev.*, D64:097101, 2001.

[A+03] A. Airapetian et al. The q**2-dependence of nuclear transparency for exclusive rho0 production. *Phys. Rev. Lett.*, 90:052501, 2003.

[A+04] A. Airapetian et al. Flavor decomposition of the sea quark helicity distributions in the nucleon from semi-inclusive deep-inelastic scattering. *Phys. Rev. Lett.*, 92:012005, 2004.

[A+05a] A. Airapetian et al. First measurement of the tensor structure function b1 of the deuteron. *Phys. Rev. Lett.*, 95:242001, 2005.

[A+05b] A. Airapetian et al. Quark helicity distributions in the nucleon for up, down, and strange quarks from semi-inclusive deep-inelastic scattering. *Phys. Rev.*, D71:012003, 2005.

[A+07a] A. Airapetian et al. The beam–charge azimuthal asymmetry and deeply virtual compton scattering. *Phys. Rev. D*, 75:011103, 2007.

[A+07b] A. Airapetian et al. Precise determination of the spin structure function g1 of the proton, deuteron, and neutron. *Phys. Rev.*, D75:012007, 2007.

[Ade98] B. et al. Adeva. Spin asymmetries a_1 and structure functions g_1 of the proton and the deuteron from polarized high energy muon scattering. *Phys. Rev. D*, 58(11):112001, Oct 1998.

[AV] E. Avetisyan and I. Vilardi. Private communications. 2007.

[Ava98] H. Avakian. Performance of the electromagnetic calorimeter of the hermes experiment. *NIM A*, 417:69, 1998.

[B+94] D.P. Barber et al. The hera polarimeter and the first observation of electron spin polarization at hera. *NIM A*, 338:166, 1994.

[B+02a] C. Baumgarten et al. An atomic beam polarimeter to measure the nuclear polarisation in the hermes gaseous polarized hydrogen and deuterium target. *NIM A*, 82:606, 2002.

[B+02b] M. Beckmann et al. The longitudinal polarimeter at hera. *NIM A physics/0009047 DESY 00-106*, 479:334–348, 2002.

[B+03a] C. Baumgarten et al. A gas analyzer for the internal polarized target of the hermes experiment. *NIM A*, 508:268, 2003.

[B+03b] C. Baumgarten et al. Measurements of atomic recombination in the hermes polarized hydrogen and deuterium storage cell target. *NIM A*, 496:263, 2003.

[BDDM04] Alessandro Bacchetta, Umberto D'Alesio, Markus Diehl, and C. Andy Miller. Single-spin asymmetries: The trento conventions. *Phys. Rev. D*, 70:117504, 2004.

[Bev94] Robinson Bevington. *Data Reduction and Error Analysis for the Physical Sciences*. McGraw-Hill, 1994.

[BJ97] Ian Balitsky and Xiangdong Ji. How much of the nucleon spin is carried by glue? *Phys. Rev. Lett.*, 79(7):1225–1228, Aug 1997.

[Bjo69] J. D. Bjorken. Asymptotic sum rules at infinite momentum. *Phys. Rev.*, 179(5):1547–1553, Mar 1969.

[BMK02] A. V. Belitsky, D. Muller, and A. Kirchner. Theory of deeply virtual compton scattering on the nucleon. *Nuclear Physics B*, 629:323, 2002.

[Bru] A. Bruell. Top/bot misalignment for 96-03 data. E-mail to off-line list@hermes collaboration, June 09, 2003.

[BS86] J. Buon and K. Steffen. Hera variable-energy "mini" spin rotator and head-on ep collision scheme with choice of electron helicity. *NIM A*, 245 (2):248–261, 1986.

[Bur04] Matthias Burkardt. Generalized parton distributions for large x. *Phys. Lett. B*, 595:245, 2004.

[Car99] P.W. Carter. *The HERMES Experiment: I. Analyzing Powers in Pion Electroproduction II. The Aerogel Radiator of the HERMES RICH*. PhD thesis, CalTech, 1999.

[CJ02] Jiunn-Wei Chen and Xiangdong Ji. Leading chiral contributions to the spin structure of the proton. *Phys. Rev. Lett.*, 88:052003, 2002.

[Col07] The HERMES Collaboration. Shift primer. *HERMES Internal Document*, 2007.

[DMR+88] F. M. Dittes, Dieter Mueller, D. Robaschik, B. Geyer, and J. Horejsi. The altarelli-parisi kernel as asymptotic limit of an extended brodsky-lepage kernel. *Phys. Lett.*, B209:325–329, 1988.

[DS05] M. Diehl and S. Sapeta. On the analysis of lepton scattering on longitudinally or transversely polarised protons. *Eur. Phys. J.*, C41:515–533, 2005.

[Due95] M. Dueren. *The HERMES Experiment: From the Design to the First Results*. PhD thesis, University Erlangen-Nuernberg, DESY Grey Report: DESY-HERMES 95-02, 1995.

[ea97] Kaiser R. et al. A large acceptance recoil detector for hermes. *DESY-PRC*, page 36, 1997. DESY-PRC-97-06-ADD.

[ea03] Nass A. et al. The hermes polarized atomic beam source. *NIM A*, 505:633, 2003.

[ea06] C. Munoz Camacho et al. Scaling tests of the cross section for deeply virtual compton scattering. *Phys. Rev. Lett.*, 97(26):262002, 2006.

[ea07] P Hagler et al. Nucleon generalized parton distributions from full lattice qcd. *CERN Pre-Print DESY 07-077, JLAB-THY-07-651, TUM-T39-07-09*, hep-lat/0705.4295, 2007.

[Ell04] Frank Ellinghaus. *Beam Charge and Beam Spin Azimuthal Asymmetries in Deeply Virtual Compton Scattering*. PhD thesis, DESY-Thesis-2004-005, 2004.

[Fey89] Richard Feynman. *Photon Hadron Interactions*. Addison Wesley Longman Publishing Co, Sep 1989.

[GHH+06] M. Gockeler, Ph Hagler, R. Horsley, Y. Nakamura, D. Pleiter, P. E. L. Rakow, A. Schafer, G. Schierholz, W. Schroers, H. Stuben, and J. M. Zanotti. Probing nucleon structure on the lattice. 2006.

[GHK+04a] I.M. Gregor, I. Hristova, M. Kopytin, W. Lange, M. Reinecke, C. Shearer, J. Stewart, and A. Vandenbroucke. Study of the first prototype for the hermes silicon recoil detector with the zeus beam telescope. *HERMES Internal Report*, 04-019, 2004.

[GHK+04b] I.M. Gregor, I. Hristova, M. Kopytin, W. Lange, M. Reinecke, J. Stewart, and Vandenbroucke A. A laser test-stand for the new hermes recoil silicon detector. *HERMES Internal Report*, 04-016, 2004.

[GM64] M. Gell-Mann. A schematic model of baryons and mesons. *Phys. Lett*, 8:214–15, 1964.

[GPV01] K. Goeke, M. V. Polyakov, and M. Vanderhaeghen. Hard exclusive reactions and the structure of hadrons. *Progress in Particle and Nuclear Physics*, 47:401, 2001.

[Gro05] The Erlangen Silicon Group. Energy calibration of the silicon modules for the recoil detector with the tandem facility. *HERMES Internal Report*, 05-020, 2005.

[GT06] V. Guzey and T. Teckentrup. The dual parameterization of the proton generalized parton distribution functions h and e and description of the dvcs cross sections and asymmetries. *Phys. Rev. D*, 74:054027, 2006.

[HHK+05] M. Hoek, M. Hartig, T. Keri, S. Lu, L. Rubacek, and Seitz B. Performance of the recoil scintillating fibre tracker in a test beam at gsi. *HERMES Internal Report*, 05-013, 2005.

[HM05] I. Hristova and M. Murray. Hermes recoil silicon detector calibration to mips at t22 at desy. *HERMES Internal Report*, 0-014, 2005.

[Hoe06] M. Hoek. *Design and Construction of a Scintillating Fibre Tracker for measuring Hard Exclusive Reactions at HERMES*. PhD thesis, Universitaet Giessen, 2006.

[Jaf96] Robert L. Jaffe. Spin, twist and hadron structure in deep inelastic processes. 1996.

[Ji97a] Xiangdong Ji. Deeply virtual compton scattering. *Phys. Rev. D*, 55:7114, 1997.

[Ji97b] Xiangdong Ji. Gauge-invariant decomposition of nucleon spin and its spin-off. *Phys. Rev. Lett.*, 78:610, 1997.

[Kai97] R Kaiser. *Measurement of the Spin Structure of the Neutron using Polarised Deep Inelastic Scattering*. PhD thesis, Simon Fraser University, 1997.

[KN02] V. A. Korotkov and W. D. Nowak. Future measurements of deeply virtual compton scattering at hermes. *European Physical Journal C*, 23:455, 2002.

[Kol98] H. Kolster. The hermes gaseous internal polarised proton target and its use in the hera storage ring. Master's thesis, Ludwig-Maximilianstras-Universitaet Muenchen, 1998.

[Kop06] M. Kopytin. *Longitudinal Target-Spin Azimuthal Asymmetry in Deeply-Virtual Compton Scattering*. PhD thesis, Humboldt-Universitaet zu Berlin, August 2006.

[Kra05] B. Krauss. *Deeply Virtual Compton Scattering and the HERMES-Recoil Detector*. PhD thesis, Friedrich-Alexander-Universitaet Erlangen-Nuernberg, 2005.

[Kro06] P. Kroll. Gpds, the structure of the proton and wide-angle compton scattering. *hep-ph/0612026*, 2006.

[LA88] Elliot Leader and Mauro Anselmino. A crisis in the parton model: where, oh where is the proton's spin? *Z. Phys.*, C41:239, 1988.

[LPR+06] I. Lehmann, V. Prahl, C. Riedl, J. Stewart, and C. Van Hulse. Heating studies on the hermes target cell. *HERMES Internal Report*, 06-080, 2006.

[Maz07] M. Mazouz. Deeply virtual compton scattering on the neutron. *Exclusive Reactions at High Momentum JLab Workshop*, Talk:31, 2007.

[MR00] I. V. Musatov and A. V. Radyushkin. Evolution and models for skewed parton distributions. *Phys. Rev. D*, 61:074027, 2000.

[MRG+94] D. Muller, D. Robaschik, B. Geyer, F. M. Dittes, and J. Horejsi. Wave functions, evolution equations and evolution kernels from light-ray operators of qcd. *Fortschritte der Physik*, 42:101, 1994.

[MRST98] Alan D. Martin, R. G. Roberts, W. James Stirling, and R. S. Thorne. Parton distributions: A new global analysis. *Eur. Phys. J.*, C4:463–496, 1998.

[Nyl97] P. Nylander. A systematic method for unbinned fitting and statistical analysis. 1997.

[PTG93] ECP Division Programming Techniques Group. *ADAMO Reference Manual*. CERN, 3.3 edition, December 1993.

[PVZ05] N. Pickert, C Vogel, and D. Zeiler. Test experiment noise studies. *HERMES Internal Report*, 05-062, 2005.

[PW99] M. V. Polyakov and C. Weiss. Skewed and double distributions in pion and nucleon. *Phys. Rev. D*, 60:114017, 1999.

[Rad97] A. V. Radyushkin. Nonforward parton distributions. *Phys. Rev. D*, 56:5524, 1997.

[Rad99] A. V. Radyushkin. Double distributions and evolution equations. *Phys. Rev. D*, 59:014030, 1999.

[Sch07] G. Schierholz. Transverse hadron structure from lattice qcd. *Exclusive Reactions at High Momentum JLab Workshop*, 2007.

[ST64] A. A. Sokolov and I. M. Ternov. On polarization and spin effects in synchrotron radiation theory. *Sov. Phys. Doklady*, 8:1203, 1964.

[Ste01] CLAS Collaboration: S. Stepanyan. Observation of exclusive dvcs in polarized electron beam asymmetry measurements. *Phys. Rev. Lett.*, 87:182002, 2001.

[Tai06] P. Tait. *Beam-Induced Depolarisation at the HERMES Transversely Polarised Hydrogen Target*. PhD thesis, Friedrich-Alexander-Universitaet Erlangen-Nuernberg, 2006.

[Ter94] Yves Terrien. Last experimental results obtained at slac on the nucleon spin structure. *International Seminar on High Energy Physics Problems*, 1994.

[Van06] A. VandenBroucke. *Exclusive pi0 Production at Hermes: Detection - Simulation - Analysis*. PhD thesis, Universiteit Gent, 2006.

[VDH] M. Van Der Hagen. Private communications. 2003.

[Wak07] M. Wakamatsu. On the d-term of the nucleon generalized parton distributions. 2007.

[Wan97] W. Wander. *Reconstruction of High Energy Scattering Events in the HERMES Experiment*. PhD thesis, Friedrich-Alexander-Universitaet Erlangen-Nuernberg, 1997.

[Ye] Z. Ye. Private communications. 2006.

[Ye06] Zhenyu Ye. *Transverse Target-Spin Asymmetry Associated wuth Deeply Virtual Compton Scattering on the Proton and A Resulting Model-Dependent Constraint on the Total Angular Momentum of Quarks in the Nucleon*. PhD thesis, Universitaet Hamburg, 2006.

[YMMN06] Z Ye, M Murray, C. A. Miller, and W.D. Nowak. A model dependent constrain on ju and jd from the transverse target-spin asymmetry assiciated with dvcs from 2002-2004 data. *HERMES Release Report*, page 30, 2006.

[Zwe94] G. Zweig. An su(3) model for strong interaction symmetry and its breaking. *CERN Preprint*, 8182-TH:401, 194.